PHYSIK-DEPARTMENT

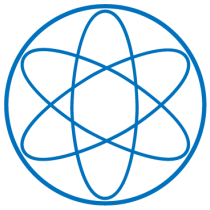

Dose Reconstruction in Radioactively Contaminated Areas Based on Radiation Transport Calculations and Measurements

PhD Thesis

Mauritius Michael Hiller

Dec. 2014

Technische Universität München

Fakultät für Physik

Lehrstuhl für Experimentalphysik E12

Dose Reconstruction in Radioactively Contaminated Areas Based on Radiation Transport Calculations and Measurements

Mauritius Michael Hiller

Vollständiger Abdruck der von der Fakultät für Physik der Technischen Universität München zur Erlangung des akademischen Grades eines

Doktors der Naturwissenschaften (Dr. rer. nat.)

genehmigten Dissertation.

Vorsitzender:	Univ.-Prof. Dr. J. Leo van Hemmen
Prüfer der Dissertation:	1. Hon.-Prof. Dr. Herwig G. Paretzke
	2. Univ.-Prof. Dr. Stefan Schönert

Die Dissertation wurde am 30.12.2014 bei der Technischen Universität München eingereicht und durch die Fakultät für Physik am 20.03.2015 angenommen.

Contents

List of Figures v

List of Tables ix

Zusammenfassung Deutsch xi

Abstract English xiii

1 Introduction and Concept of This Work 1

1.1 The Techa River Dose Reconstruction Problem 1

1.2 Task of This Work 5

2 Fundamentals 7

2.1 Radiation Transport Calculations 7

2.1.1 Monte Carlo Radiation Transport Calculations 8

2.1.1.1 Particle Transport 8

2.1.1.2 Random Numbers and Sampling Methods 9

2.1.1.3 Estimators 10

2.1.1.4 Accuracy of Monte Carlo Results 11

2.1.2 Photon Transport 12

2.1.3 The Monte Carlo Code MCNP for Radiation Transport Calculations 14

2.2 Radioactive Decay of the Radionuclide ^{137}Cs 15

2.3 Radiation Dose Rate Measurements 16

2.4 Integrated Radiation Dose Measurements by Stimulated Luminescence 18

2.4.1 Thermoluminescence (TL) Basics 18

2.4.2 Aluminum Oxide TLD 20

2.4.3 TL Dosimeter Analysis 21

2.5 Retrospective Dosimetry by Brick Sample Analysis 22

2.5.1 Brick Sample Analysis 23

2.6 Determination of Anthropogenic and Background Doses 25

2.7 In-Situ Gamma Spectroscopic Measurements 26

3 Measurements and Experimental Results **27**
3.1 Geometrical Dose Rate Mapping at the Church Tower . . . 29
3.2 Sample Collection at the Church Tower . . . 31
3.2.1 Age of Buildings . . . 33
3.2.2 Results of the Brick Measurements . . . 33
3.2.3 Results of the TLD Measurements . . . 35
3.2.4 Results of the Dose Rate Measurements at the Church Tower . . . 37
3.3 Geometric Measurements at the Church Tower . . . 38
3.4 Measurements at the Reservoir Lake . . . 39
3.5 In-Situ Gamma Spectroscopy in Soil . . . 42

4 Radiation Transport Simulations – Setup and Results **45**
4.1 Conversion Factors Between Doses in Bricks and Doses in TLD Materials . . . 45
4.1.1 Energy Dependence of the TLD Response . . . 45
4.1.2 Setup of the Simulation . . . 47
4.1.2.1 Simulation of Brick and TLD . . . 47
4.1.2.2 Simulation of the Spectrum Above Soil . . . 48
4.1.3 Determination of the Conversion Factors . . . 49
4.1.3.1 Doses in Brick and TL Dosimeters . . . 49
4.1.3.2 Spectra Above Soil . . . 51
4.1.3.3 Conversion Factors Between Doses in Brick and Doses in TLD . . . 52
4.1.3.4 Angular Dependence . . . 53
4.1.3.5 Effects of Plaster and Glue at the Wall . . . 54
4.2 Geometric Dose Profile at a Brick Wall . . . 56
4.2.1 Setup . . . 56
4.2.2 Observations . . . 57
4.3 Absorption of a Source under a Water Layer . . . 58
4.4 Simulation of the Metlino Area . . . 59
4.4.1 The Church Tower . . . 60
4.4.2 The Reservoir model . . . 62
4.4.3 The Metlino Model . . . 64
4.4.4 Migration of the Radionuclide ^{137}Cs in Soil . . . 69

5 Results – Determination of Air Kerma at Shoreline **70**
5.1 Estimation of the Anthropogenic Dose from 1949 – 1956 in Brick . . . 70
5.1.1 Reservoir Model . . . 70
5.1.2 Reservoir Dose . . . 78
5.1.3 Anthropogenic Dose in Brick from 1949 to 1956 . . . 81

5.2 Estimation of the Time Integrated Air Kerma . . . 83
5.3 Probabilistic Approach . . . 89
5.3.1 Alternative Estimation of the Effective Half-Life of the Radionuclide ^{137}Cs . . 91

6 Discussion 93
6.1 Environmental Influences on Dosimetric Results . . . 93
6.1.1 Soil Types . . . 93
6.1.2 Water Levels in Metlino . . . 93
6.1.3 Moisture Content in Soil . . . 95
6.1.4 Snow Shielding Factor . . . 96
6.1.5 Effect of the Environmental Conditions on the Data Interpretation . . . 96
6.2 Variation of the Source Configuration in the Metlino Model . . . 97
6.2.1 Depth Distribution of Radionuclides . . . 97
6.2.2 Depth-Dose Distribution in Bricks . . . 99
6.2.3 Spatial Radionuclide Distribution . . . 99
6.3 Height Profiles on the South Side of the Church Tower . . . 102
6.4 Air Kerma Compared to the Techa River Dosimetry System (TRDS) . . . 104
6.4.1 Validation of the TRDS by Taranenko et al. . . . 104

7 Summary and Outlook 106
7.1 Summary . . . 106
7.2 Outlook . . . 108

Bibliography 111

Appendix A Material Data used for MCNP Input 121

Appendix B Results for Different MCNP Versions 123

Appendix C Sampling Sites at the Church Tower 124

Appendix D Granary 127

List of Figures

1.1 The Nuclear Facilities of Mayak . . . 2
1.2 The Techa River . . . 3
1.3 The Reservoir System . . . 3
1.4 Map of Metlino . . . 4
1.5 Metlino 1965 . . . 5

2.1 Particle Path . . . 8
2.2 Decay Scheme of ^{137}Cs . . . 16
2.3 Automess Setup . . . 17
2.4 Automess Conversion Curves . . . 18
2.5 Energy Representation of the OSL Process . . . 19
2.6 TL Emission Spectrum of α-Al_2O_3:C . . . 20
2.7 The Risø TL/OSL Reader DA-15 . . . 21
2.8 Brick Sample . . . 23
2.9 Brick Crushing . . . 23
2.10 TL Curve . . . 24
2.11 OSL Curve . . . 25
2.12 Under Water Probe . . . 26

3.1 Metlino Site . . . 28
3.2 Remaining Buildings in Metlino . . . 28
3.3 Dose Rate Measurements at the Church Tower . . . 30
3.4 Brick Sample Locations . . . 31
3.5 Sampling Site at the Church Tower . . . 33
3.6 Church Tower Dimensions . . . 38
3.7 Measurement Points at the Reservoir Lake . . . 40
3.8 Transects Across the Reservoir Lake . . . 41
3.9 Gamma Spectroscopy in Soil . . . 43
3.10 Activity Distribution in Soil . . . 44

4.1 TLD Energy Dependence . . . 46

4.2 Simulation of TLD . . . 48
4.3 Absorbed Dose per Air Kerma . . . 50
4.4 Spectrum Above Soil . . . 51
4.5 Conversion Factor . . . 53
4.6 Angular Dependence . . . 54
4.7 Plaster on the Brick Wall . . . 55
4.8 Source in Front of Brick Wall . . . 56
4.9 Dose Profile at the Brick Wall . . . 57
4.10 Calculated Absorption of a Water Layer . . . 59
4.11 Metlino Before and After Evacuation . . . 60
4.12 Church Tower Model . . . 61
4.13 Brick Sample Locations . . . 61
4.14 Simulated Sampling Site . . . 62
4.15 Reservoir Lake . . . 63
4.16 Source Distribution . . . 63
4.17 Source Distribution in the Reservoir Model . . . 64
4.18 Historic Map . . . 65
4.19 Landscape Elevation . . . 65
4.20 Elevation of Peninsula . . . 66
4.21 Sources Compared . . . 67
4.22 Migration in Soil . . . 69

5.1 Determination of the Integral Air Kerma . . . 71
5.2 Determination of the Integral Air Kerma using Source Weights . . . 71
5.3 Height Profile . . . 72
5.4 Additional Souces . . . 73
5.5 Height Profile using Updated Source Configuration . . . 74
5.6 Source Numbers . . . 75
5.7 Annual Dose in TLD . . . 77
5.8 ^{137}Cs Concentration in Water as a Function of the Calendar Year . . . 79
5.9 Reservoir Doses . . . 80
5.10 Anthropogenic Dose in Brick Between 1949 and 1956 . . . 82
5.11 Dose in Brick at South-Western and South-Eastern Wall . . . 85
5.12 Dose in Air . . . 87
5.13 Time Integrated Air Kerma at Shoreline . . . 88
5.14 Integral Air Kerma at Shoreline . . . 90
5.15 Integral Air Kerma at Shoreline . . . 92

6.1 Water Level Variation 94
6.2 Precipitation in the Yekaterinburg Area 94
6.3 Water Content in Soil 95
6.4 Impact of the Source Depth to the Integral Air Kerma at the Shoreline 97
6.5 Impact of the Source Depth to the Integral Air Kerma at the Shoreline 98
6.6 Source Distribution in the Reservoir Model 100
6.7 Impact of the Source Area to the Air Kerma at Shoreline 101
6.8 Impact of the Source Area to the Air Kerma at Shoreline 102
6.9 Profiles on the South Side 103

7.1 Sample Location Overview 109

B.1 Results of Calculations with two MCNP Versions 123

C.1 Sampling Sites at the Church Tower 124

D.1 Dose Rate Measurements at the Granary 128
D.2 Granary 128

List of Tables

3.1 Sample Locations . . . 32
3.2 Results of Dose in Brick Measurements . . . 34
3.3 Results of TLD Measurements . . . 35
3.4 Annual Dose Measured with TLD . . . 36
3.5 Installation Time of TLD . . . 36
3.6 Current Dose Rates at the Church Tower . . . 37

4.1 Conversion Factor . . . 52

5.1 Measured Dose Rates in Air over the Source Areas . . . 75
5.2 Specific Activity in the Source Cells . . . 76
5.3 Annual Dose in TLD . . . 78
5.4 Reservoir Doses . . . 81
5.5 Anthropogenic Dose in Brick Between 1949 and 1956 . . . 83
5.6 Dose per Photon in Brick . . . 86
5.7 Dose per Photon at Various Locations in the Metlino Model . . . 87
5.8 Dose Conversion Factors . . . 88
5.9 Time Integrated Air Kerma at Shoreline . . . 88
5.10 Effective Half-Lives Calculated for Selected Sites at the Church Tower . . . 92

A.1 Air Composition . . . 121
A.2 Soil Composition . . . 121
A.3 Brick Composition . . . 121
A.4 Plaster Composition . . . 122
A.5 Wood Composition . . . 122
A.6 Al_2O_3 Composition . . . 122
A.7 Heat Shrink Tube Composition . . . 122
A.8 Glue Composition . . . 122

D.1 Dose Rates at the Granary 2011 . . . 129
D.2 Dose Rates at the Granary 2012 . . . 130

Zusammenfassung Deutsch

Die externe Strahlenbelastung in der ehemaligen Ortschaft Metlino wurde rekonstruiert. Der Techa Fluss in Metlino wurde durch die Anlagen von Mayak kontaminiert. Resultierend daraus wurde der Ort evakuiert und ein Reservoirsee angelegt. Absorbierte Dosen in Ziegeln wurden gemessen und Modelle des heutigen und früheren Ortes für Monte Carlo Rechnungen erstellt. Durch Kombination dieser konnte das Luftkerma am Ufer des Techa rekonstruiert und das Techa River Dosimetry System evaluiert werden.

Abstract English

The external radiation exposure at the former village of Metlino, Russia, was reconstructed. The Techa river in Metlino was contaminated by water from the Mayak plant. The village was evacuated in 1956 and a reservoir lake created. Absorbed doses in bricks were measured and a model of the present-day and the historic Metlino was created for Monte Carlo calculations. By combining both, the air kerma at shoreline could be reconstructed to evaluate the Techa River Dosimetry System.

Chapter 1

Introduction and Concept of This Work

The effect of ionizing radiation on humans is studied in most cases by investigating groups of persons which had an exposure of a relatively high dose by external radiation during a short time period. This kind of exposure scenario applies to, among others, the following cohorts: Atomic bomb survivors of the towns of Hiroshima and Nagasaki, patients treated in radiation therapy and workers of nuclear facilities exposed to radiation mainly during a single accident.
To get information about effects of low dose radiation, the observations of these groups have to be extrapolated to low doses, which can introduce systematic errors. Moreover, there is no evidence in this data, that the curve behaves linearly in the low-dose section.

The **L**inear **N**o **T**hreshold hypothesis (LNT) theory assumes a linear relationship between a dose and the biological response to the dose with no threshold. While the abscissa shows the dose, the ordinate gives the degree of the corresponding biological or health effect. Zero dose shows a natural or spontaneous incident level. An increasing trend for high doses is proven, however there is only statistically inadequate data for lower doses [21, 22, 75, 88, 89, 105].
To fill the gap of knowledge in the low dose regime, epidemiological studies were performed on cohorts of people that were exposed to anthropogenically low dose radiation generated at low dose rates. To precisely determine the correlation between the dose and the health effect, both, the health data and the doses need to be determined in the best possible way.

1.1 The Techa River Dose Reconstruction Problem

Today the **M**ayak **W**orker **C**ohort (MWC), the **E**xtended **T**echa **R**iver **C**ohort (ETRC) and the **T**echa **R**iver **O**ffspring **C**ohort (TROC), are regarded as one of the most important data sources for late health effects associated with low-dose rate exposure to plutonium, strontium and external gamma radiation [7, 50, 63, 76, 78, 91, 97, 102].
As the persons in these groups suffer from a radiation with low dose rates and low doses over a

much longer time period than the groups mentioned before, findings from these groups will be more reliable in the low dose regime than the error prone extrapolated answers from the other groups. This information can give reliable answers to the effect of low dose radiation to human health and can give criteria to affirm or rebut the LNT hypothesis [5, 6, 27, 60, 61, 93].

The Combine Mayak, or Mayak Production Association (PA) and the city of Ozyorsk (see Fig. 1.1) were constructed between 1945 and 1948 as part of the Soviet nuclear weapons program in Southern Urals, Russia. The primary objective of the plant was the production of plutonium for nuclear weapons. During the operation of the plant, which is still active today, several uranium-graphite reactors and reactors for producing weapons-grade plutonium were constructed along with a radio-chemical plant, a chemical-metallurgical plant and radioactive waste-management facilities [112].

Figure 1.1: The Nuclear Facilities of Mayak
The Techa river passes by the Mayak PA on the back of the picture. [Courtesy of A. Ulanovsky]

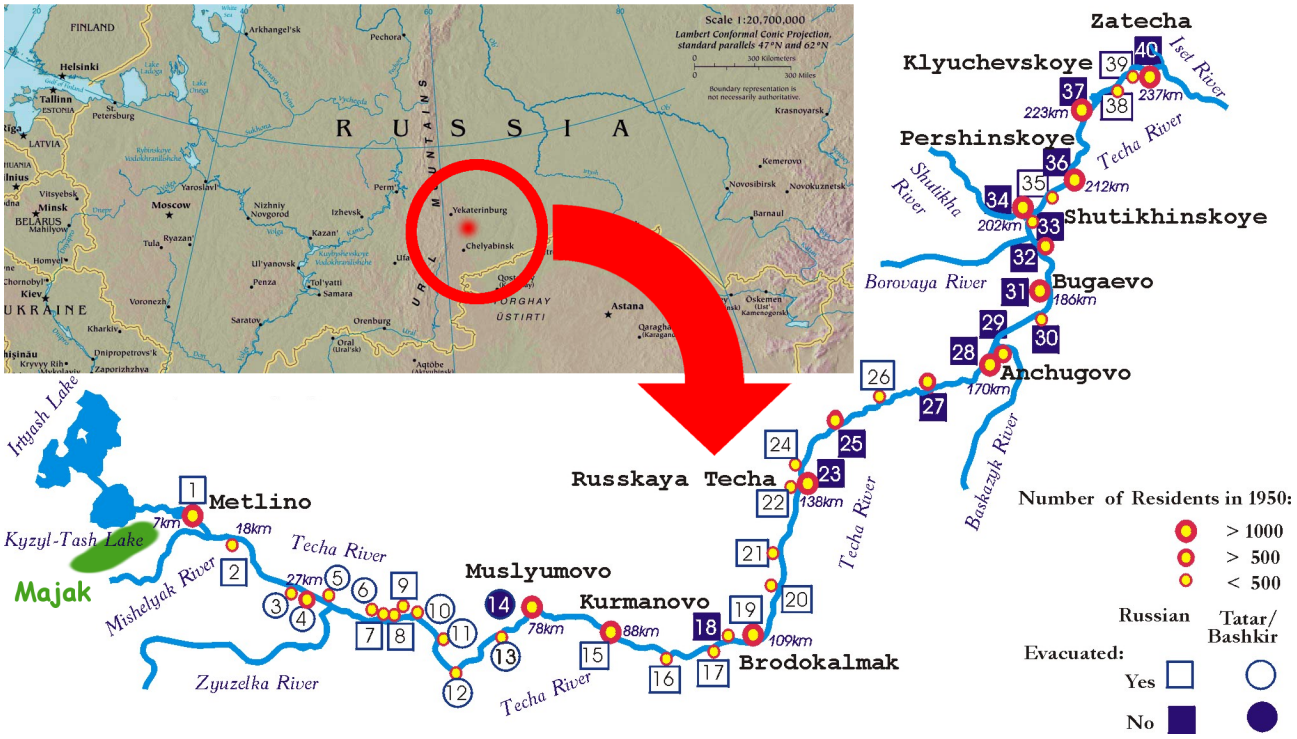

Figure 1.2: The Techa River

The Techa river is located in Southern Urals, Russia. The nuclear facilities of Mayak are at the spring of the river; the former village of Metlino is located at 7 km distance. The village Metlino was evacuated among others due to high radioactive contamination. [Courtesy of N. Semioschkina]

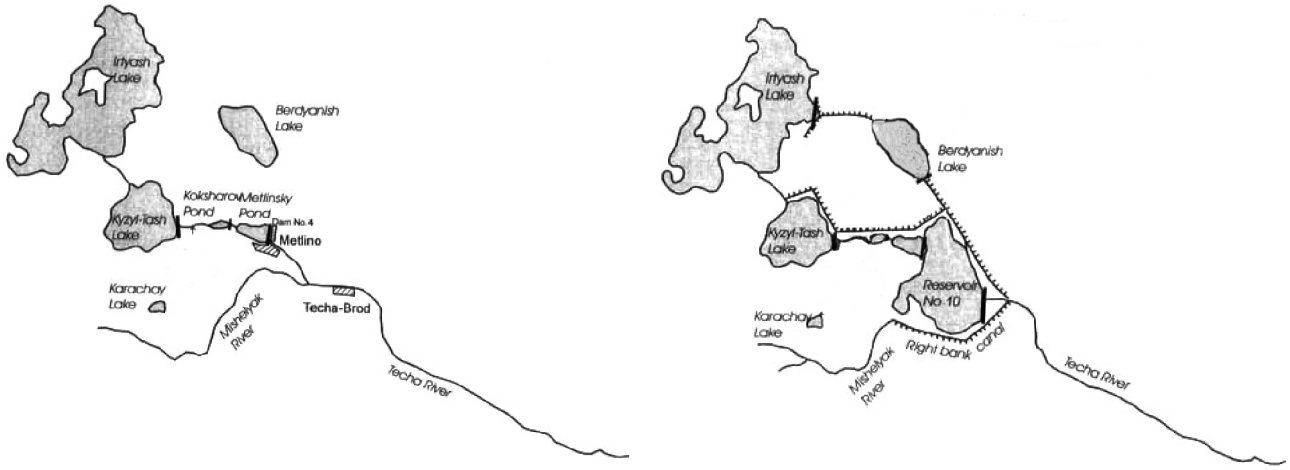

a. Before the evacuation **b.** After the evacuation

Figure 1.3: The Reservoir System

Various reservoir lakes and sewage canals were added to the Techa river system over the years. After the evacuation of Metlino in 1956, the Reservoir lake R10 was created on parts of the former settlement [112].

Between 1949 and 1956, liquid radioactive waste from the Mayak PA was diluted with water from a lake and then disposed of in the nearby Techa river (see Fig. 1.2). The release characteristics of radioactive waste into the Techa river system changed quite frequently in the time from 1949 - 1956 (see e.g. Vorobiova et al. [112]). A system of reservoir lakes was created along the course of the river (see Fig. 1.3) [72].

Between 1949 and 1956, liquid radioactive waste from the Mayak PA was diluted with water from a lake and then disposed of in the nearby Techa river (see Fig. 1.2). The release characteristics of radioactive waste into the Techa river system changed quite frequently in the time from 1949 – 1956 (see e.g. Vorobiova et al. [112]). A system of reservoir lakes was created along the course of the river (see Fig. 1.3) [72].

It is important to realize, that the main source of radiation studied here is not due to one of the accidents in Mayak, but due to ongoing operation [65].
The village of Metlino (see Fig. 1.4 and 1.5) is located at the shores of both, the Techa river and a small lake called *Metlinski pond*. It is the first village downstream of Mayak in about 7 km distance to the site. The village was evacuated and demolished in 1956 due to the high radioactive contamination of the Techa river. Not all buildings were torn down after evacuation of the village. A church, a former mill and a granary are still remaining today. In the course of the last fifty years, some walls of the mill and granary have collapsed, and the church and its tower are heavily weathered. After the evacuation, a reservoir lake, called *Reservoir 10*, or *Shubinsky pond*, was created [26, 34, 69–73, 112].

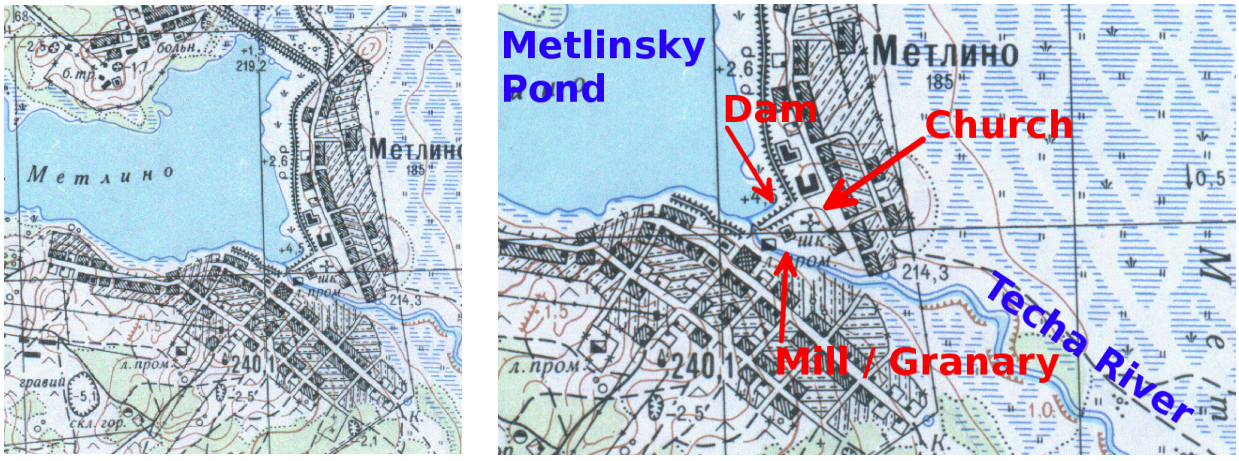

Figure 1.4: Map of Metlino
The map dates between 1952 and 1956 and shows the old village of Metlino along the shore of the Metlinski pond and the Techa river. The buildings of the Mill, Granary and the Church were not destroyed. On the other side of the dam, opposed to the Metlinski pond, the reservoir lake R10 was created. [Courtesy of A. Ulanovsky]

Figure 1.5: Metlino 1965
All buildings except a mill, a granary and a church with its tower were destroyed. The reservoir lake R10 covers now the area where buildings were before. [Courtesy of A. Ulanovsky]

1.2 Task of This Work

This work focuses on the reconstruction of radiation exposure at the former village of Metlino in Southern Urals, Russia, to provide improved information about the x-axis (dose) in ongoing epidemiological studies on the Techa river cohorts. These studies are conducted in the project SOLO (Epidemiological Studies of Exposed **So**uthern Ura**l**s P**o**pulations) funded by the European Union's "Seventh Framework Program" and were also addressed in the former project SOUL [55]. It is anticipated that the results of the project will give new insight into the effect of ionizing radiation at low dose levels. For a reliable quantification, a constant improvement of health and dosimetric data is needed.

To assess the dose along the Techa river, the **T**echa **R**iver **D**osimetry **S**ystem (TRDS) was established [31–35, 79, 111]. The key parameter for the external exposure in the TRDS is the annual air kerma above shoreline $K_r(t)$ in Gy a^{-1}. The external exposure accounts for about one third of the total exposure at the location of Metlino (estimate after Degteva et al. [28]). The goal in this work is to assess the air kerma due to anthropogenic radiation sources, to validate the TRDS, version 2009, for the location of Metlino. Therefore it is important to estimate the integral air kerma at shoreline between 1949, the beginning of the contamination and 1956, the time of the evacuation: $K_x = \int_{1949}^{1956} K_r(t)dt$.
This can be achieved due to the fact that bricks function as natural dosimeters, i.e. they store the information on natural and anthropogenic sources of radiation exposure since the time of their firing until today. By combining experimental methods with computer modeling, based on a reconstructed spatial distribution of the radioactive contamination around the site, dose in air at selected reference points can be inferred from the measured dose in bricks.

For this work, three field trips to the former village of Metlino were performed to gather the necessary data. During the field trips, detailed dose rate measurements and measurements of the geometry of the landscape and the remaining buildings were performed. Brick samples were collected from selected building walls and thermoluminescence dosimeters were deployed in the brick wall for one year, in order to monitor the present gamma dose rate due to the contamination.
These measurements and several other sources were used to create a detailed model of the landscape, the buildings and the source configuration for extensive radiation transport calculations using the Monte Carlo Code MCNP.

In summary, with this experimental and theoretical work, the dosimetry system for the evacuated village of Metlino and its evacuated should be evaluated and improved.

Chapter 2

Fundamentals

2.1 Radiation Transport Calculations

Radiation transport can be simulated with several different methods and approaches. These methods are based on the transport equation, which in its simplest form describes the particle distribution in a medium for a differential energy and directional flux density. The particle transport can be described or estimated with analytic or numeric approaches.
The radiation transport can be analytically described by e.g. the law of attenuation and the interaction equations. Deterministic methods include the diffusion approximation or multi-group approximations or the discrete-ordinates theory [95].
None of these methods is able to describe a complicated, arbitrary three dimensional geometry with extended sources, like it is the case for the dose reconstruction in a historically contaminated area, such as the former settlement of Metlino studied in this work. These complicated boundary conditions can only be treated with the help of Monte Carlo methods.

Monte Carlo is the name of a collection of mathematical techniques that use stochastic probability to estimate correct predictions to physical problems. Numerical modeling allows two approaches, deterministic and Monte Carlo methods. Deterministic methods require the approximation of integrals or differential equations, and they are limited by how well the result is approximated. In contrast to this, Monte Carlo methods sample the exact integral or differential equation with a large number of statistical trials that observe the underlying physical experiment using stochastic methods. For each statistical trial, a Monte Carlo approximation uses a different set of random numbers. Deterministic methods provide more exact solutions of approximate models, whereas Monte Carlo methods provide statistically approximate solutions of more exact models [45, 56].
The Monte Carlo method was originally developed mainly for radiation transport applications. The name *Monte Carlo* was first used in the 1949 paper by N. Metropolis and S. Ulam titled *The Monte Carlo method* [67].

2.1.1 Monte Carlo Radiation Transport Calculations

2.1.1.1 Particle Transport

The particle transport is described in Monte Carlo methods using the integral form of the Boltzmann transport equation:

$$F(R) = \int K(R;R')F(R')dR' + S_f(R) \tag{2.1}$$

where R is the kinetic energy, direction of flight and spatial coordinates of the particle, F(R) is the collision density and $S_f(R)$ is the first flight collision density due to extraneous sources, $K(R,R')$ is the next flight collision density at R due to a collision at R' [23].

In a Monte Carlo transport problem, not a complete description of the problem is provided at a time, as in the deterministic numerical solution. Rather the particle history is simulated stepwise, observing and simulating only the appropriate physical parameters of the transport at the current step of the history of the particle [23].

The particle transport process for neutral particles, like photons studied in this work, satisfies the following conditions:

1. Particles travel in straight lines without losing energy.
2. Particles suffer a collision per unit distance with the probability Σ_t.
3. The time between entering and leaving a collision can be neglected.
4. The simulated particle transport is linear.

The geometric travel of a particle is described by the position (x,y,z) and the direction of flight (u,v,w) (see Fig. 2.1). After traveling a distance λ the particle is at position $x' = x + u\lambda$, $y' = y + v\lambda$, $z' = z + w\lambda$ [23].

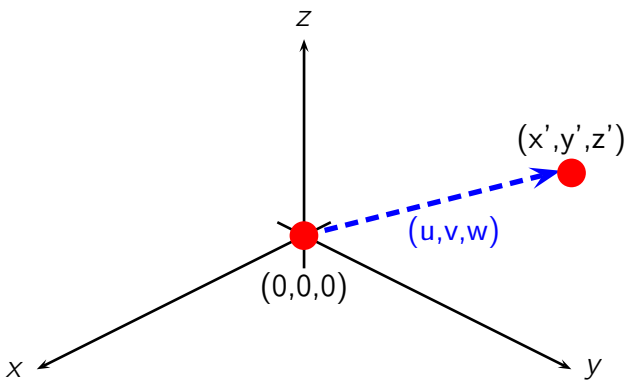

Figure 2.1: Particle Path
The figure shows the path of a particle in the Cartesian coordinate system. After starting from point (x,y,z) = (0,0,0) and traveling into direction (u,v,w), the particles next collision is at position (x',y',z').

For the first step of the history, a free path length x_i has to be associated to the particle by setting it to $x_i = -(1/\rho\sigma)\ln(1-\xi_i)$, with ξ_i being from (0,1). The next step is to decide for the interaction of the particle. For example, assuming the chance of absorption being 0.1 and the chance of scatter being 0.9, the interval (0,1) is split into (0,0.1) and [0.1,1), the future of the particle is decided by the second random number ξ_i being in the first or the second interval. Further steps in the history of the particle, like a scattering angle, etc. are sampled accordingly [45].

The sources distribution is sampled by a density function $S(\boldsymbol{r}, E, \Omega, t)$. The source can be biased using an importance function $I(\boldsymbol{r}, E, \Omega, t)$ to sample the important particles more frequently than the not so important. The difference in the number of particles is then compensated by their weight. With this, the source coordinates are selected with the density function

$$g(\boldsymbol{r}, E, \Omega, t) = \frac{S(\boldsymbol{r}, E, \Omega, t)\, I(\boldsymbol{r}, E, \Omega, t)}{\int S(\boldsymbol{r}, E, \Omega, t)\, I(\boldsymbol{r}, E, \Omega, t)\, d^3r\, dE\, d\Omega\, dt}. \tag{2.2}$$

An initial weight

$$W = \frac{S(\boldsymbol{r}, E, \Omega, t)}{g(\boldsymbol{r}, E, \Omega, t)} \tag{2.3}$$

is attributed to the source particles. It is $(\boldsymbol{r}, E, \Omega, t)$ the coordinate of the particle with $\boldsymbol{r}$ the location of the particle, E its energy, Ω the direction and t the time [23, 95].

The probability that a particle starting at $s = 0$ will hit a next collision at Δs is given by

$$p(s)\Delta s = \Sigma_t(s) \exp\left\{-\int_0^S \Sigma_t ds'\right\} \Delta s. \tag{2.4}$$

The weight of the particle has to be adjusted to

$$W' = W\, \frac{\Sigma_s(s) \exp\left\{-\int_0^S \Sigma_t ds'\right\}}{\left[\overline{\Sigma}_t(s) \exp\left\{-\int_0^S \overline{\Sigma}_t ds'\right\}\right]} \tag{2.5}$$

after the collision where Σ_t and Σ_s are the total and scattering cross sections.
This method of weight adjustment to account for capture in a collision is called *implicit capture*. The alternative is *analog capture* in which the particle is terminated with the probability of capture, but continued with no weight adjustment with the probability of scatter [23].

2.1.1.2 Random Numbers and Sampling Methods

Random numbers are a sequence of numbers drawn from an interval without any pattern in the sequence itself. In Monte Carlo, these random numbers are created by random number generators. Many schemes for the generation of random numbers exist. Most schemes are pseudo random, gen-

erating the numbers from arithmetic subroutines. Those algorithms must have a certain randomness and they have to be uniformly distributed and uncorrelated [23, 62].

A sequence of random numbers ξ is drawn from the interval (0,1) to sample probability distributions and thereby construct a hypothetical but realistic history for the simulated particle.
A basic sampling is done with a probability density function

$$p(x) = p_i \quad \text{with} \quad i-1 \leq x \leq i \quad \text{for} \quad i = 1, 2, \ldots, n. \tag{2.6}$$

The random numbers

$$\xi = P(x) = \int_0^x p(t)dt \tag{2.7}$$

are uniquely defined as a function of ξ to sample a value of x.
Another method often used for sampling is the rejection technique in which x is sampled from an easily sampled density function and rejected if it is outside the bounds of the true density function [23, 45].

An example of a probability density function is the one that shows how far a particle is transported before the next event occurs. With ρ being the atom density of the material and σ the total cross section, the distance x to the next event is given by probability density function $\rho\sigma e^{-\rho\sigma x}dx$ [45].

2.1.1.3 Estimators

The Monte Carlo method does not give answers, but instead statistical estimates of the mean value of a distribution. The Monte Carlo estimators can be separated into four basic classes: collision estimators, surface estimators, track-length estimators and next-event estimators (so called point detectors).

Surface estimators usually calculate currents, the number of particles crossing a surface, or fluxes on a surface. They can also be used to calculate energy deposition and pulse height by a balance adding the energy crossing a surface into a region and subtracting the energy crossing out.

The collision estimator scores at collisions in the desired tally volume with a functional $W \cdot \frac{\Sigma(\boldsymbol{r},E)}{\Sigma_t(\boldsymbol{r},E)}$. Here, W is the weight of the particle (how many particles are represented by the statistical track), S the track length, Σ the macroscopic reaction cross section and Σ_t the total cross section, $\boldsymbol{r}$ the spacial location and direction and E the energy.

The track length estimator scores the flux for every path within the desired geometric space, $W \cdot \int_0^S \Sigma(\boldsymbol{r}, E)ds$. The flux can be converted to a reaction rate or dose rate when multiplied by

volume and cross section.

The next-event estimator calculates the flux at a point as $W \cdot e^{-\lambda} \frac{p(\mu)}{2\pi R^2}$, which is the density function for particle to go to the point as the next event after the source birth or a collision. It can also be used for a deterministic transport within a Monte Carlo calculations from collisions and source points in the direction of a low-probability region of the problem [23, 98, 100].

2.1.1.4 Accuracy of Monte Carlo Results

A large number of n histories, or statistical trials, are generated in the described way in a Monte Carlo problem. The laws of large numbers applies to the results of Monte Carlo simulations. Finding the statistical error can give confidence in the result of the Monte Carlo calculations.
When each history produces a score x_i, the mean score X_n is calculated by

$$X_n = \frac{1}{n} \sum_{i=1}^{n} x_i \tag{2.8}$$

The relative error of the estimate, called variance, can be approximated as the mean of the squares of the scores subtracted by the square of the mean score:

$$Var(x_i) = \frac{1}{n} \sum_i x_i^2 - \left(\frac{1}{n} \sum_i x_i \right)^2 \tag{2.9}$$

The relative error in the probability distribution is given by

$$\frac{1}{X_n} \sqrt{\frac{Var(x_i)}{n}} \tag{2.10}$$

The law of large numbers states that the mean X_n approaches the real solution if the number of histories n, approaches infinity; this can be proven using Chebyshev's inequality [23, 45].

In real applications, more information about the mean is demanded, which can be explored using the Central Limit Theorem. With n independent, identically distributed random numbers $x_1, x_2, \ldots x_n$, a common mean m and a variance σ^2 are given. The central limit theorem becomes

$$\lim_{n \to \infty} P \left\{ m + a \frac{\sigma}{(n)^{1/2}} \leq X_n \leq m + b \frac{\sigma}{(n)^{1/2}} \right\} = \frac{1}{(2\pi)^{1/2}} \int_a^b e^{-t^2/2} dt. \tag{2.11}$$

In Monte Carlo, the random variable is a function $x(t)$ with t being governed by the probability

distribution $p(t)$. Then, the common mean m can be written as

$$m \equiv E(x) = \int_{-\infty}^{+\infty} x(t)p(t)dt \tag{2.12}$$

and the variance σ^2 that appears in the central limit theorem becomes

$$\sigma^2 = \int_{-\infty}^{+\infty} [x(t) - E(x)]^2 \, p(t)dt = E(x^2) - E^2(x). \tag{2.13}$$

The sample mean of n experimental trials becomes

$$X_n = \frac{1}{n}\sum_{i=1}^{n} x(t_i) = \frac{1}{n}\sum_{i=1}^{n} x_i. \tag{2.14}$$

When the random variable x is sampled n times, the sample variance $\overline{\sigma}^2$ is

$$\overline{\sigma}^2 = \frac{1}{n-1}\sum_{i=1}^{n}(x_i - X_n)^2 = \frac{n}{n-1}\left(\frac{1}{n}\sum_{i=1} nx_i^2 - X_n^2\right). \tag{2.15}$$

$\overline{\sigma}^2$ approaches

$$\overline{\sigma}^2 \cong \frac{1}{n}\sum_{i=1}^{n} x_i^2 - X_n^2 \tag{2.16}$$

if n becomes sufficiently large [23].

2.1.2 Photon Transport

Scattering laws are used to simulate the travel of photons, treated as particles, through matter in Monte Carlo calculations. Various collision types are integrated into Monte Carlo radiation transport codes. For photons in the energy range of 1 keV to 100 MeV, five basic scattering processes are needed to accurately model photon transport: Photoelectric absorption with fluorescence, incoherent scattering (Compton scattering with form factors), coherent scattering (Thomson scattering with form factors), pair production and bremsstrahlung [62, 104].

The photoelectric effect describes the absorption of a photon with energy E by an electron, releasing the electron from an atomic shell. The released electron has a kinetic energy of $e = E - e'$ with e' being the binding energy of the electron in the shell.
For the Monte Carlo Calculation, the photoelectric effect means the termination of the photon history. The photoelectric cross section σ_{pe} depends on the energy of the incident photon and the atomic number of the atom the electron is attached to. σ_{pe} increases with approximately the 4.5^{th} power of the atomic number and decreases rapidly with the energy. After photoelectric absorption multiple photons can be emitted by fluorescence [23, 62].

The Compton scattering describes the collision of the photon with a free electron at rest. The particle is assigned an energy $E = h\nu$ with ν the frequency and h the Planck constant. In the Compton scattering process, the outgoing photon energy e is calculated with the incoming photon energy E and the scattering angle θ as:

$$e = \frac{E}{1 + E(1 - \cos\theta)}. \tag{2.17}$$

The cross section for the scattering of a photon of energy E is given by the Klein-Nishina equation.

In reality, electrons are neither free nor at rest when a photon hits them. These binding effects are corrected by the incoherent scattering function, or *form factor*.
Incoherent scattering models the scattering from bound electrons. The cross section is described by $\sigma_{inc}(E, \theta, z) = \sigma_1(E, \theta) \cdot S(q, z)$ with $S(q, z)$ the incoherent scattering function and $q = (E^2 + e^2 - 2Ee\cos\theta)^{1/2}$.
Data for cross sections and scattering factors are included in most Monte Carlo codes [23, 62].

Coherent (Rayleigh) scattering describes the process of the interaction of a photon with a bound electron without an energy loss. It has to be considered at low photon energies for materials with high atomic numbers. The angular distribution is described by a product of the classical Thomson cross section with the atomic form factor to account for the electron binding effect [23, 62].

Pair production happens in the vicinity of a nucleus or an electron. It becomes important with energies greater than the energy of two electrons at rest $2m_ec^2 = 1.022\,\text{MeV}$. It describes the process of creating an electron – positron – pair with particle energies of $m_ec^2 = 0.511\,\text{MeV}$ each. The initial photon is terminated at pair production, the excess energy over 1.022 MeV is distributed among the electron positron pair as kinetic energy.
The cross section rises monotonically from zero at the threshold energy of 1.022 MeV.
Generally, the positron recombines with the next electron on its path emitting two photons with an energy of m_ec^2 each. The two annihilation photons are emitted in opposite directions and are uncorrelated to the primary photon. In Monte Carlo codes, the annihilation is modeled at the point of the pair production [23, 62].

Photons are also produced during the slowing down of electrons, or bremsstrahlung. Bremsstrahlung photon production can be approximated by neglecting the electron transport and only producing the bremsstrahlung photons at photon collisions by sampling the bremsstrahlung photon production probability density functions and making assumptions about subsequent photon direction and displacement [100].

2.1.3 The Monte Carlo Code MCNP for Radiation Transport Calculations

The **M**onte **C**arlo-**N**-**P**article (MCNP) code is a well-established Monte Carlo code with a long history dating back to the 1940s. MCNP has a wide user base with several thousand users which apply the code to a multitude of different applications, including, but not limited to criticality safety, oil-well logging, nuclear energy, nuclear safeguards, fusion research, medical technology and space exploration. Due to its long history of usage, the code has matured, has been compared to uncountable experiments and has been proven to estimate the results correctly [4, 45].

The simulations presented in this work were carried out with the MCNP 5 code, version 1.60 [100]. Version 5, 1.60 was the current version at the beginning of this work in 2011, and although the newer version 6.1 [85] was published since then, the version was kept constant over the time of this project for reasons of consistency. The updated features of the new version do not apply to the problems presented here. Some benchmark tests against the new version were carried out, but no difference in the results was observed (see appendix B).

MCNP enables the user to set up arbitrary geometric shapes and structures bounded by surfaces via an input file to create the problem geometry. The geometric structures can be filled by any desired material that can be created by specifying the elemental composition of the material. Appendix A lists the composition of the materials used in this work. The MCNP geometry plots presented here were generated using the Visual Editor, version X24_J by R. Schwarz et al. [94].

In the problems presented here, mostly photon calculations including secondary electrons were carried out. Photons are mostly from contamination with the radionuclide ^{137}Cs with an energy of 0.662 MeV. Several problems included electrons modeled in energy ranges from 0.03 – 3.00 MeV or other nuclear isotopes besides ^{137}Cs.

For all photons, the following physical effects are treated: Photoelectric effect, pair production, Compton scattering and incoherent scattering. The detailed physics used here also includes coherent (Thompson) scattering and accounts for fluorescent photons after photoelectric absorption [100].

The dose estimation is mostly done by energy deposition F6 tallies that estimate the average energy deposition in the desired tally region using track length estimators. Track length estimators, in contrast to collision estimators, are especially recommended for optically thin media, like the detectors in air used in many of the problems presented here. The track length estimator itself is a limiting form of the collision estimator. The track length estimator determines the flux which is then multiplied by a kerma factor (heating number) to provide energy deposition.

Other dose estimations are performed using *F8 tallies that estimate the energy deposition via an energy balance of particles crossing surfaces to enter or leave a geometric region.
Flux spectra are estimated with the F4 tally that scores the flux averaged over a cell volume [23, 98, 100].

MCNP results are always normalized per source particle.
Energies are given in units of MeV, masses in g. Hence doses are given in units of MeV g^{-1} and can be converted into Gy = J kg^{-1} by multiplication with a rounded factor of $1.602 \cdot 10^{-10}$.
The flux is given in units of $\frac{\text{particles}}{\text{cm}^2}$.

The Monte Carlo calculations were always optimized to produce a relative statistical error below 2 % that is not listed with the MCNP results shown here.

To reduce computer time required to achieve a desired relative error, several techniques can be applied to the calculation, optimizing the figure of merit (FOM)

$$FOM = \frac{1}{\sigma^2 t} \tag{2.18}$$

with σ^2 the variance and t the computer time needed.
Electron energies were cut off below 0.03 MeV which did not affect the outcome of the simulations.
Geometry splitting with Russian roulette can be performed when a particle undergoes certain events: The particle is split when it travels in an important direction and it gets rouletted when it travels in the opposite direction. The importance can be assigned to a particle on its travel on a grid independent of the underlying geometry, called weight windows [15–17, 44, 46–48, 80, 86].

2.2 Radioactive Decay of the Radionuclide ^{137}Cs

Today, the remaining dominant radionuclide in Metlino is the long lived ^{137}Cs with a physical half-life of about 30 years (see section 4.4.3). ^{137}Cs itself is a pure beta emitter, but with a 95 % probability, ^{137}Cs decays to the metastable ^{137m}Ba with a half-life of 2.55 min (see Fig. 2.2). The metastable ^{137m}Ba decays to the stable ^{137}Ba, emitting the characteristic 0.662 MeV photon [104].

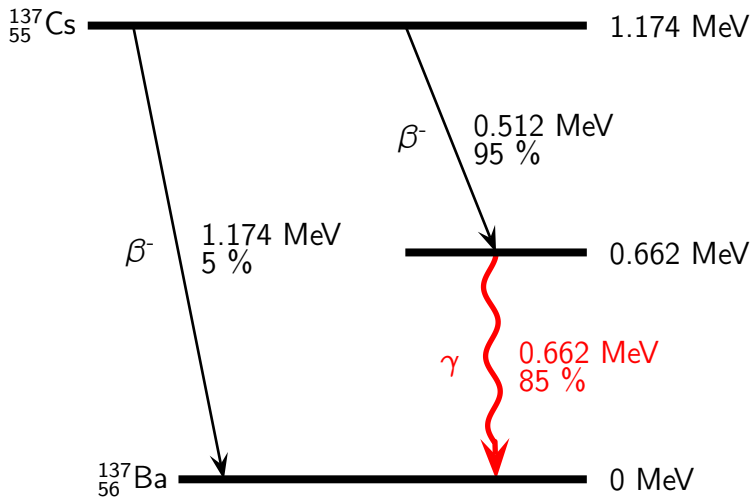

Figure 2.2: Decay Scheme of ^{137}Cs
The radionuclide ^{137}Cs decays via beta emission to the metastable ^{137m}Ba, that itself emits the characteristic 0.662 MeV photon (drawing after [104]).

2.3 Radiation Dose Rate Measurements

The dose rate measurements in air were performed with a hand held dose rate meter from Automess, Ladenburg, Germany, model *6150 AD 6/E*, serial number 122445 [108].

The devices specifications state an accuracy of 5 %, when the device has integrated the dose over a sufficiently long enough time. For the case of low dose rates in Metlino, this time was usually impractically long.
In a conservative approach, an error of 20 % was assumed for a confidence interval of 95 %. This was also assumed by Taranenko et al. [99] and Jacob et al. [54].

The dose rate meter gives the dose as dose equivalent H*(10) in units of $\mu Sv\,h^{-1}$. ICRU 51 states that "The ambient equivalent dose, H*(d), at a point in a radiation field, is the dose equivalent that would be produced by the corresponding expanded and aligned field, in the ICRU sphere at a depth, d, on the radius opposing the direction of the aligned field." [81] The quantity H*(d) is in units of $J\,kg^{-1}$. The special name for the untit of the ambient dose is the sievert, Sv. For a strongly penetrating radiation, a depth of 10 mm is recommended by the ICRU [81, 96].
The quantity H*(10) is impractical for the observations here, where only the physical quantity of the absorbed dose is of interest, not an equivalent dose.

The manufacturer supplies the instrument with a conversion curve for the radionuclide ^{137}Cs and a plot of the energy and angular dependence of the detector response with regard to H*(10) and normalized to the response for ^{137}Cs at 0°. In principle these data can be used to calculate a

conversion coefficient between H*(10) and air kerma for a given photon spectrum.
Nevertheless, a conversion coefficient based on own measurements of the actual device was performed with a Cs and Co source and over the N-30 through N-300 ISO spectra with a X-ray source of the **S**econdary **S**tandard **D**osimetry **L**aboratory (SSDL) of HMGU (see Fig. 2.3). The filtered X-ray sources cover peak energies from 0.033 – 0.250 MeV while the ^{137}Cs and ^{60}Co sources have energies of 0.662 MeV and 1.250 MeV [84].

The displayed dose of the device was compared with air kerma at the detector position. A curve for the energy and the angular dependence was established and a conversion curve between air kerma and H*(10) was derived (see Fig. 2.4). The Automess device was irradiated in different angles from 0 – 360 °. It was also sampled for a variation in the positioning of the Automess, with the Automess at a flat position, the radiation was entering through the narrow top side, while at an upright position, the radiation was entering through the front side (see Fig. 2.3).
For the photon spectrum produced by a 0.662 MeV ^{137}Cs source homogeneously distributed in the ground up to a depth of 30 cm, a conversion coefficient of 0.78 was evaluated.

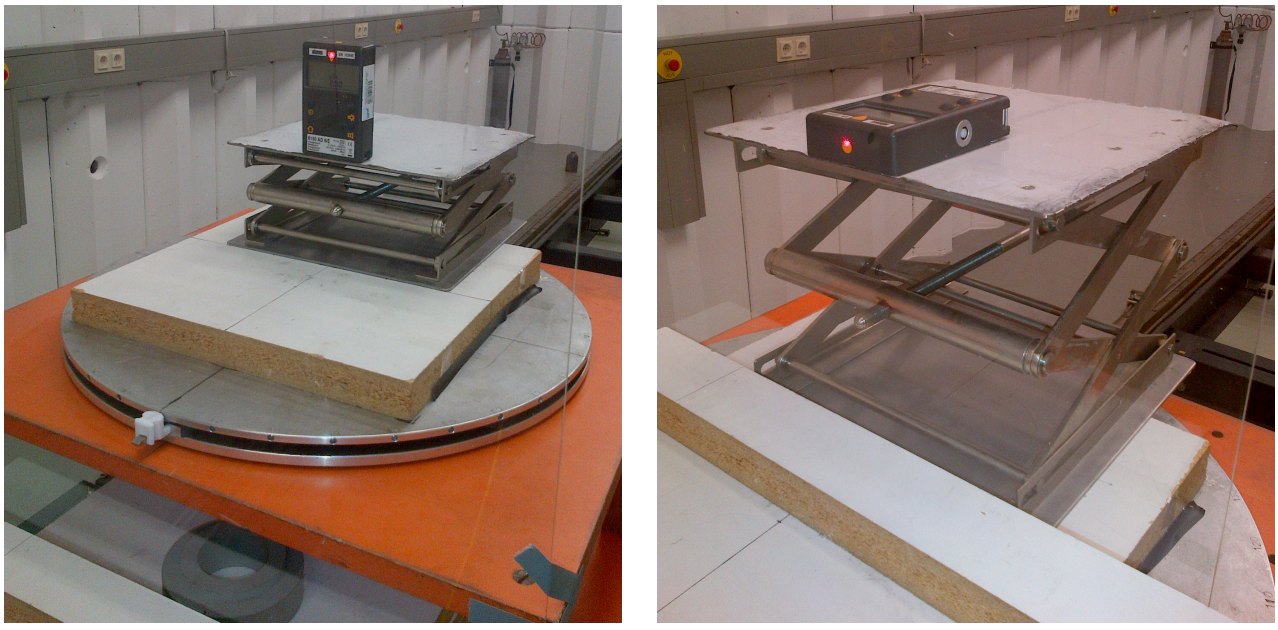

a. Front side **b.** Top side

Figure 2.3: Automess Setup
The picture shows the setup of the Automess at the Buchler source. The radiation enters the device from the front side (**a**) and the top side (**b**), marked by a red laser spot.

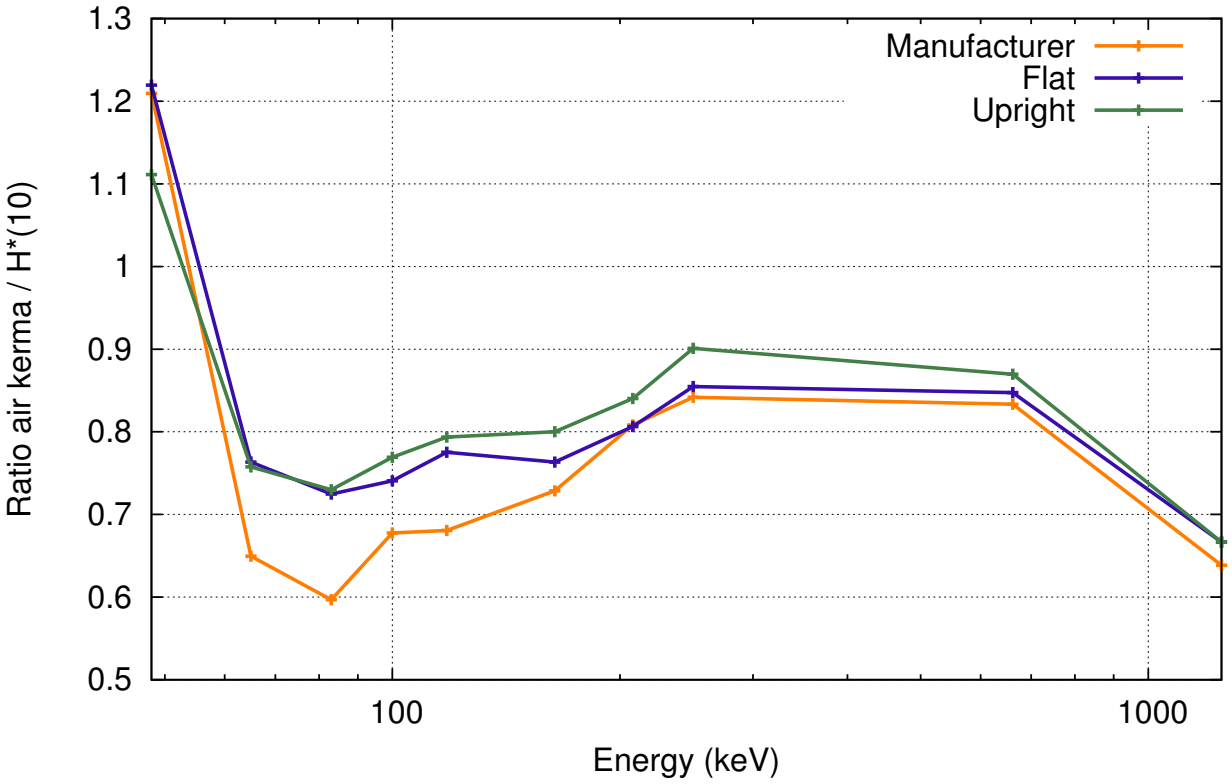

Figure 2.4: Automess Conversion Curves
The figure shows the conversion curve to convert H*(10) doses in air kerma at the Automess dose rate meter. The curve derived from data provided by the manufacturer is shown in orange. The conversion curve for flat and upright positions of the Automess are shown in blue and green [108].

2.4 Integrated Radiation Dose Measurements by Stimulated Luminescence

2.4.1 Thermoluminescence (TL) Basics

"**T**hermo**l**uminescence (TL) is one of a family of processes known as thermally stimulated phenomena" [64]. In the first stage, a perturbation is introduced by irradiation and the system is shifted to a metastable state (see Fig. 2.5a). In the second stage, the electron is stored in the conduction band. In the third stage, the system gets back to its initial state by heating it, the electrons get evicted from the conduction band under the emission of photons, the so called thermally stimulated relaxation. The amount of irradiation introduced in the first stage corresponds to the energy (light) release in the second stage [3, 64].

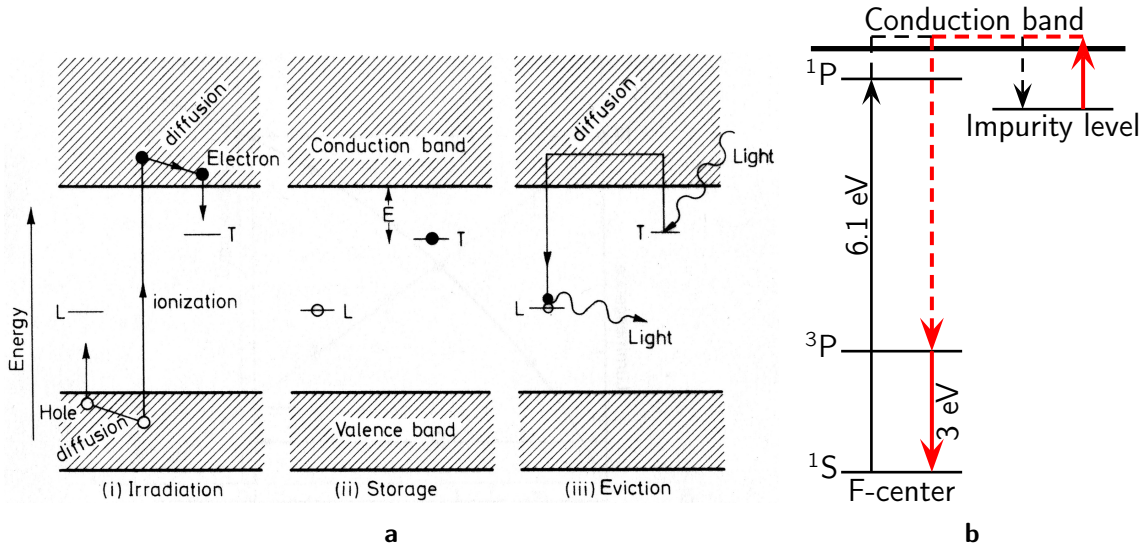

Figure 2.5: Energy Representation of the OSL Process

Figure **(a)** shows the three stages of the TL process: Irradiation, Storage and Eviction [3]. Figure **(b)** shows the emission scheme for the Al_2O_3:C material used as TLD in this work (drawing after [117]).

Absorption of energy from ionizing radiation creates additional lattice defects in the material over and above the thermal defects and impurities that are initially existing in the material. In this context, radiation induced defects denote localized electronic energy states, impurities and displaced (interstitial) atoms, occupied by a non-equilibrium concentration of electrons. Defect creation by energy storage occurs via the process of electron-hole pair production by ionizing radiation in the crystal lattice. The free charge carriers can diffuse throughout the lattice and undergo various trapping and de-trapping events until finally being thermally stabilized at a specific lattice site. The amount of trapped charges (and thus the amount of radiation-induced defects created) is proportional to the amount of absorbed energy and thus to the absorbed dose. Materials and impurities used for TLD include LiF:Mg,Cu,P, LiF:Mg,Ti (TLD-100) $CaSO_4$:Dy and Al_2O_3:C (TLD-500), where by convention, the basic material is written before the colon ":" and the impurities after it, material:impurity.

The energy release in form of thermoluminescence is stimulated by increasing the sample temperature. The recombination of the electron-hole pairs releases energy in the from of photons. The emitted photons can be registered by a sensitive photomultiplier in a TL-reader.

The recorded glow curve, consisting of several glow peaks for a material depends on the type of material, number and distribution of defects and various other characteristics. The probability of electron release p at temperature T is given by

$$p(T) = s(T) \exp\left\{-\frac{E}{kT}\right\} \tag{2.19}$$

where s(T) is an only weakly temperature dependent factor called frequency factor, E the energy

difference between the localized trapping state and the conduction band, and k the Boltzmann constant.
Energy can also be released by the by the process of recombination between interstitial atoms (H centers) and vacancies (F centers) described by

$$F + H = \text{perfect lattice} + \text{photon}_{\text{TL}}. \tag{2.20}$$

With n_c the concentration of free electrons, n the concentration of trapped electrons and N the concentration of available electron traps, following rate equations define the process of TL production:

$$\frac{\mathrm{d}n}{\mathrm{d}t} = -n\,s\,\exp\left\{-\frac{E}{kT}\right\} + n_c(N-n)\,A \tag{2.21}$$

$$\frac{\mathrm{d}n_c}{\mathrm{d}t} = -\frac{\mathrm{d}n}{\mathrm{d}t} + \frac{n_c}{\tau} \tag{2.22}$$

where A is the trapping transition probability and τ is the recombination lifetime [64].

2.4.2 Aluminum Oxide TLD

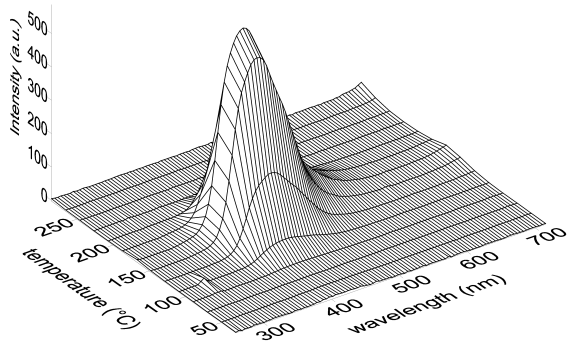

Figure 2.6: TL Emission Spectrum of α-Al_2O_3:C
The TL emission spectrum of α-Al_2O_3:C pre-irradiated with 1 Gy. The emission spectrum has a peak at 420 nm at a temperature of 160 °C when heated at 1 °C s^{-1}. [Courtesy of C. Woda]

The Al_2O_3 **T**hermo**l**uminescence **D**osimeters (TLDs) that were used in the work here are fabricated in the form of α-Al_2O_3:C samples that are grown from a melt at 2050 °C. Usually, the substance is cut into discs with 5 mm in diameter and a thickness of 1 mm. The Al_2O_3 crystal grows in a highly reduced atmosphere, but in the presence of graphite, thus the crystal gets doped with a concentration of 100 – 5000 ppm carbon atoms. This introduces large concentrations of oxygen vacancies in the crystal (F and F^+ centers). After crystal growth any deep traps get removed in an annealing process [64].

The glow curve shows a central peak between 160 °C and 209 °C, depending on the heating rate. By introducing certain approximations ("quasi-equilibrium"), the rate equations can be analytically solved to yield an analytic expression for the TL glow curve (see e.g. Randall and Wilkins, [87]).
The emission peak is at 420 nm at a temperature of 160 °C when heated at 1 °C s^{-1} and pre-irradiated with 1 Gy (see Fig. 2.6) due to an electron transition from the excited ^{3}P to the ^{1}S ground state

with a lifetime of $\approx$ 35 ms, emitting 3 eV photons that are registered as blue light. The emission scheme for the Al_2O_3:C crystal used as TLD in this work is shown in figure 2.5b. The energy release can be described with equation (2.20) as a recombination of an electron with an F^+ center [64, 117]:

$$F^+ + e^- \Rightarrow F^* \Rightarrow F + h\nu_{420nm} \tag{2.23}$$

2.4.3 TL Dosimeter Analysis

The dosimeters were installed in the 2011 field trip and removed in the 2012 field trip. After removal from the church tower, they were transported to the lab at **H**elmholtz Zentrum **M**ünchen für **G**esundheit und **U**mwelt (HMGU). Table 3.3 lists all dosimeters with their types, table 3.5 gives information on the time the dosimeters were installed.

The TL chips were read out using a Risø TL-DA-12 instrument, similar to the one shown in figure 2.7. A heat absorbing HA-3 filter and a Corning 7-59 glass filter transmitting in the range of 300 – 500 nm were used. No source was installed to avoid unintentional exposure of the highly sensitive TL chip by scattered radiation, and the LED element was removed to bring the photomultiplier closer to the sample.

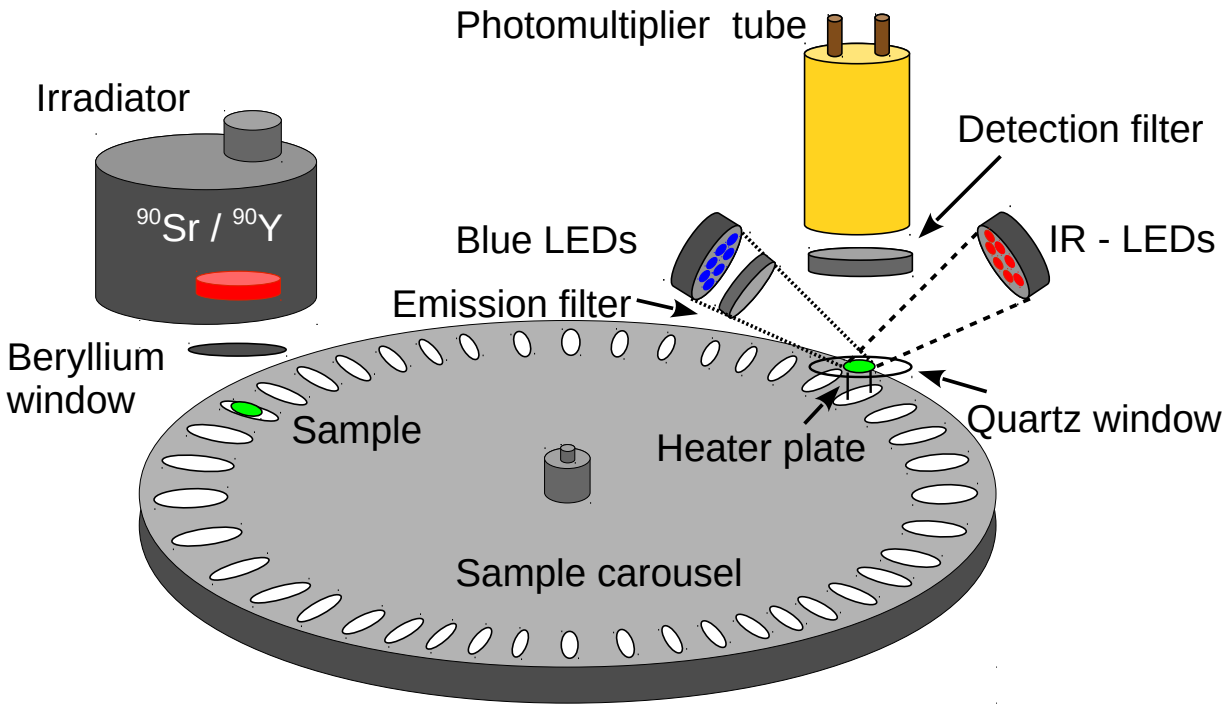

Figure 2.7: The Risø TL Reader DA-15

The drawing shows the essential parts of the Risø DA-15 TL/OSL reader. The sample can be irradiated by a ^{90}Sr / ^{90}Yr sample and can be excited by blue LEDs. Through a filter, the emitted photons are registered in a photomultiplier tube. The source and the LED element were removed for TL measurements [36].

Knowing the storage time of each TLD, the average dose rate per year was calculated.
Three dosimeters were transported to the site and back without further usage in Metlino at the 2011 field trip. They were used to determine the dose accumulated on the dosimeters during transport. These dosimeters showed an average transportation dose of 0.08 mGy. The dose of the installed dosimeters was corrected by this value.

A background dose rate for the TLD of $0.70 \pm 0.08\,\mathrm{mGy\,a^{-1}}$ was calculated, based on gamma-spectrometric measurements of the specific activity of natural radionuclides in brick (see section 2.5) and MCNP derived dose conversion coefficients, reported in Aznar et al. [8].

2.5 Retrospective Dosimetry by Brick Sample Analysis

With luminescence (TL/OSL) measurements, not only the TL dosimeters shown in the previous section can be analyzed. Also the dose accumulated in natural quartz grains, which are present in the bricks in the walls of the church tower in Metlino, can be read out. The suitability of luminescence measurements for the measurement of brick samples was shown various times before [11, 18–20, 40–42, 66, 99, 115, 116].
For TLD, a specifically engineered crystal is exposed to radiation. But also in natural crystal structures, such as granite or feldspar minerals, defects get introduced by radiation that can be analyzed with the TL method. Like for the TLD chips, the sample is heated and the emitted light pulse is analyzed to determine the radiation. The biggest difference to the TLD is a reduced sensitivity, more complex measurement protocols, and that brick samples have to be treated mechanically and chemically before analyzing them with TL or OSL.

The natural concentration of lattice defects in a crystalline structure is in the range of 10^{-8} – 10^{-7} ppm. The number of radiation-induced occupied sites calculates as

$$I = S \cdot \dot{D} \cdot \tau_1 \left(1 - \exp\left\{-\frac{t}{\tau_1}\right\}\right) \tag{2.24}$$

with I the intensity, S the sensitivity, $\dot{D}$ the dose rate and τ_1 the time to fill $(1 - e^{-1})$ sites.

For **O**ptically **S**timulated **L**uminescence (OSL) measurements, the sample is stimulated by an external light source instead of a heat source [113].

2.5.1 Brick Sample Analysis

The brick samples collected in the field trips were first taken to a lab at the **U**rals **R**esearch **C**enter for **R**adiation **M**edicine (URCRM) in Chelyabinsk, Russia. The samples were cleaned and cut to a reasonable size there.

Then the samples were transported to the lab at HMGU for further processing. Figure 2.8 shows a brick sample. The short side was facing towards the outside of the wall. The brick was exposed to sunlight, which can bleach the dose information in the surface layer. Thus, the outer layer of the brick with a thickness of 0.5 cm was removed.

Figure 2.8: Brick Sample
A brick sample as it arrived in the lab at HMGU. The small side was facing outside of the wall. The brick was sectioned into slices of approximately 1 cm thickness. These slices were analyzed separately.

The brick was sectioned into slices of 1 cm thickness, from the front on. The brick sections were analyzed separately with TL/OSL methods. From all samples, the section from 0.5 – 1.5 cm and 2.5 – 3.5 cm was analyzed. From selected samples, also deeper sections were analyzed, this allowed the analysis of a depth profile of the brick. All cutting procedures on the brick were carefully carried out by hand using a saw with a thin round blade to avoid unnecessary heating.

The slices were then gently crushed with a metal piston (see Fig. 2.9a). After the slice was crushed down to a fine powder, the powder was sieved with a coarse mesh of 200 µm width and then again with a finer mesh of 140 µm (see Fig. 2.9b, 2.9c). The fraction between 140 µm and 200 µm was taken for chemical processing.

a. Piston **b.** Coarse mesh **c.** Fine mesh

Figure 2.9: Brick Crushing
The brick slices were crushed using the piston shown in (**a**). The powder was then filtered with a coarse 200 µm mesh (**b**) and a fine 140 µm mesh (**c**). The fraction between 140 µm and 200 µm was further processed chemically.

About 2 – 4 g of the 140 – 200 µm fraction of brick powder was cleaned in 10 % HCl for 1 h in an ultrasonic bath. This process removes calcite, organic residues and carbonates.
The HCl was removed and the samples were cleaned with distilled water. The powder was then wet-sieved and dried in the oven over night at 50 °C.
Subsequently, samples were etched for 40 minutes with 40 % hydrofluoric acid in a rotary shaker, carefully decanted and rinsed several times with distilled water. After a final 1 hour cleaning step with HCl in an ultrasonic bath, the samples were wet-sieved to a grain size larger than 140 m and dried overnight [2, 116].

The TL measurements were performed using Risø TL-DA-12 instrument, similar to the one shown in figure 2.7. A heat absorbing HA-3 filter and a Corning BG 3 glass filter transmitting in the range of 300 – 500 nm were used.
For measurements with TL, a restricted single aliquot regeneration protocol was used, terminating the glow curve at 270 °C and using three calibration points, thus avoiding significant changes in sensitivity [9]. A typical TL glow curve of one aliquot of sample C10 is shown in figure 2.10a. At the heating rate of 2 °C s^{-1} the curve peaks at 210 °C. Figure 2.10b shows the calibration curve of the same aliquot to convert the TL signals into dose. The plateau test (see Fig. 2.10c) indicates which temperature interval can be used to determine doses unaffected by thermal fading [2].

The OSL samples were analyzed using the Risø TL/OSL-DA-15 instrument (see Fig. 2.7) equipped with blue LEDs stimulating the sample with light of 470 ± 30 nm. A 7.5 mm U-340 Hoya optical filter with a transmission window of 290 – 370 nm was used for detection.

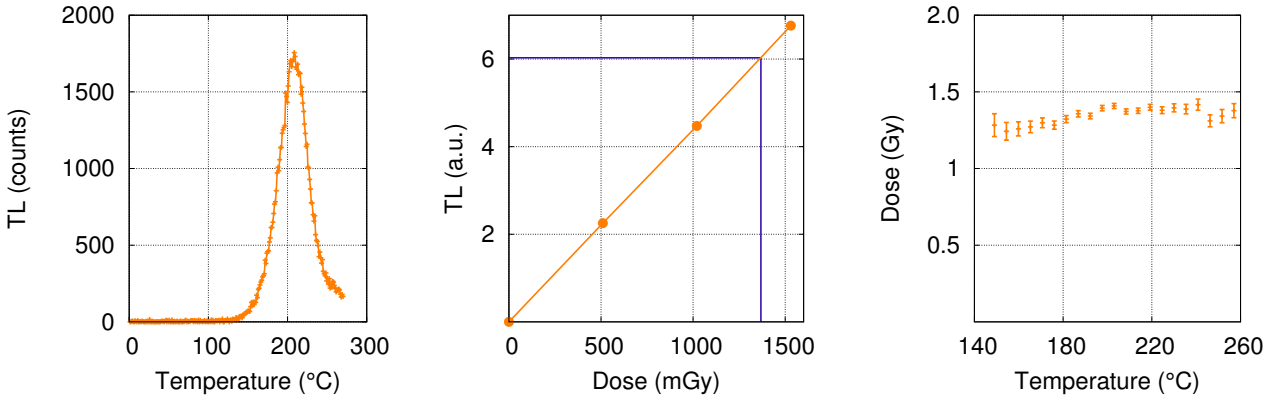

a. TL signal **b.** TL calibration **c.** Plateau test

Figure 2.10: TL Curve
The TL curve of sample C10 is shown. **a:** Glow curve showing the 210 °C TL peak. **b:** Calibration curve for the sample. **c:** The plateau test indicates which temperature interval can be used to determine doses unaffected by thermal fading.

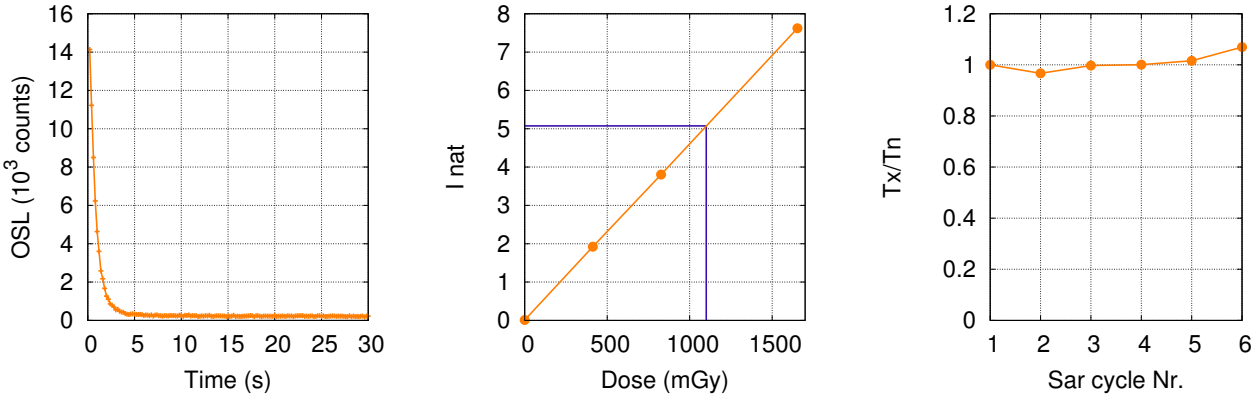

a. OSL signal **b.** OSL calibration **c.** Monitoring of sensitivity

Figure 2.11: OSL Curve

a: The OSL curve of sample C6. **b:** Calibration curve to convert OSL signals to dose. **c:** Sensitivity analysis over various SAR cycles.

For OSL measurements, a single aliquot regeneration (SAR) protocol with test dose normalization was used [9,10,77]. A preheat of 190 °C for 10 seconds and a cutheat of 160 °C was applied [115,116]. A typical OSL curve, here for sample C6, is shown in figure 2.11a. Figure 2.11b shows the calibration curve to convert the OSL signals to dose. The sample shows a constant sensitivity over various SAR cycles (see Fig. 2.11c).

2.6 Determination of Anthropogenic and Background Doses

The absorbed dose measured in brick, also termed the cumulative dose, DL, consists of two parts: The dose due to natural background, DBG, and the dose due to anthropogenic sources, D_X, the latter being of interest here. For assessing the background dose, it is assumed that all bricks from one building were fired in the same year and thus all have the same age T. By measuring the specific activity of natural radionuclides in each brick and applying tabulated dose conversion coefficients (see Adamiec and Aitken [1], and Ulanovsky and Woda [106]), each bricks individual background dose can be calculated as:

$$D_{BG} = \dot{D_{BG}} \cdot T. \tag{2.25}$$

The age of the samples can be either assessed from historical records (if available) or by dating of well-shielded background samples. The anthropogenic dose can then be calculated as:

$$D_X = D_L - D_{BG}. \tag{2.26}$$

2.7 In-Situ Gamma Spectroscopic Measurements

Gamma ray spectroscopy to assess radionuclides is mostly performed using Ge semiconductors or NaI scintillation detectors. The three most important interaction processes in these detectors are the photoelectric effect, the Compton effect and the pair production. The full cascade of interactions of photons with matter is registered in the detectors. In scintillation detectors, photons are detected with a photomultiplier, producing an electric pulse that can be registered with a counter. In semiconductors, the incident radiation produces electrons and holes which recombine directly on the detector electrodes [82].

The detectors consist of a Ge crystal in a vacuum cryostat with a window at the endcap minimizing the absorption of the incident radiation. The detectors are characterized by their size (for scintillation detectors) or their relative efficiency towards a standardized 3“ NaI crystal for 1.33 MeV gamma radiation from a ^{60}Co source (for Ge detectors). The energy resolution is characterized by the FWHM for a full energy peak from the standard ^{60}Co radiation [82].

In this work, in-situ gamma spectroscopic measurements on the ground of the reservoir lake were performed during the 2012 field trip (see section 3.4). Measurements in soil were performed on a previous field trip in 2008 (see section 3.5).
For the measurements on the ground of the reservoir lake, a portable spectrometric collimated detector was used by O. Ivanov and colleges [51]. The underwater radiometer allows the screening of bottom sediments without taking samples. It measures the surface activity of the radionuclide ^{137}Cs and other nuclides with an error below 30 % [24, 25, 90, 118].
The sketch in figure 2.12 shows the scintillation detector on the bottom sediment in its housing. From the Monte Carlo calculations, the thickness of the contaminated and an uncontaminated layer on the top of it can be reconstructed using suitable integration intervals in the photo peak and the Compton continuum in the gamma spectrum of the radionuclide of interest [51].

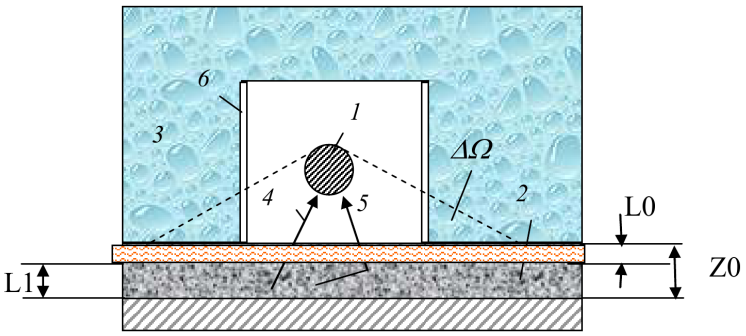

Figure 2.12: Under Water Probe
The collimated detector probe sits on the bottom sediment of a lake. It detects scattered and unscattered radiation [51].

Chapter 3

Measurements and Experimental Results

Most of the data used in this work is based on samples and measurements collected on field trips to the former village of Metlino at the Techa river, Southern Urals, Russia. Three field trips were performed to this area: September 10^{th} – 17^{th} 2011, September 17^{th} – 21^{st} 2012, and September 16^{th} – 18^{th} 2013. Figure 3.1 shows a map of the site. A dam separates two lakes, the so called *Metlino pond* or *Metlinski pond* in the North and the *reservoir lake R10* South of the dam. The reservoir lake was created after the evacuation of the village on its former terrain. The remaining buildings in Metlino are a granary, a mill and a church with a tower. A modern weir controls the water outlet from Metlinski pond to the reservoir lake.

Figure 3.2 gives an overview of the remaining buildings of the church and the church tower as seen in the field trips. The church tower and the granary are approximately 100 m away from each other.

The main tasks of the field trips were dose rate measurements in the surrounding of the church and extraction of bricks from the walls of the church for TL and OSL measurements. TLD were installed in the walls of the church tower. The geometry of the site and the buildings thereon were measured precisely. In-situ gamma spectroscopic measurements in the sediment of the reservoir lake R10 were performed and the depth of the lake was measured on several profiles across the lake.

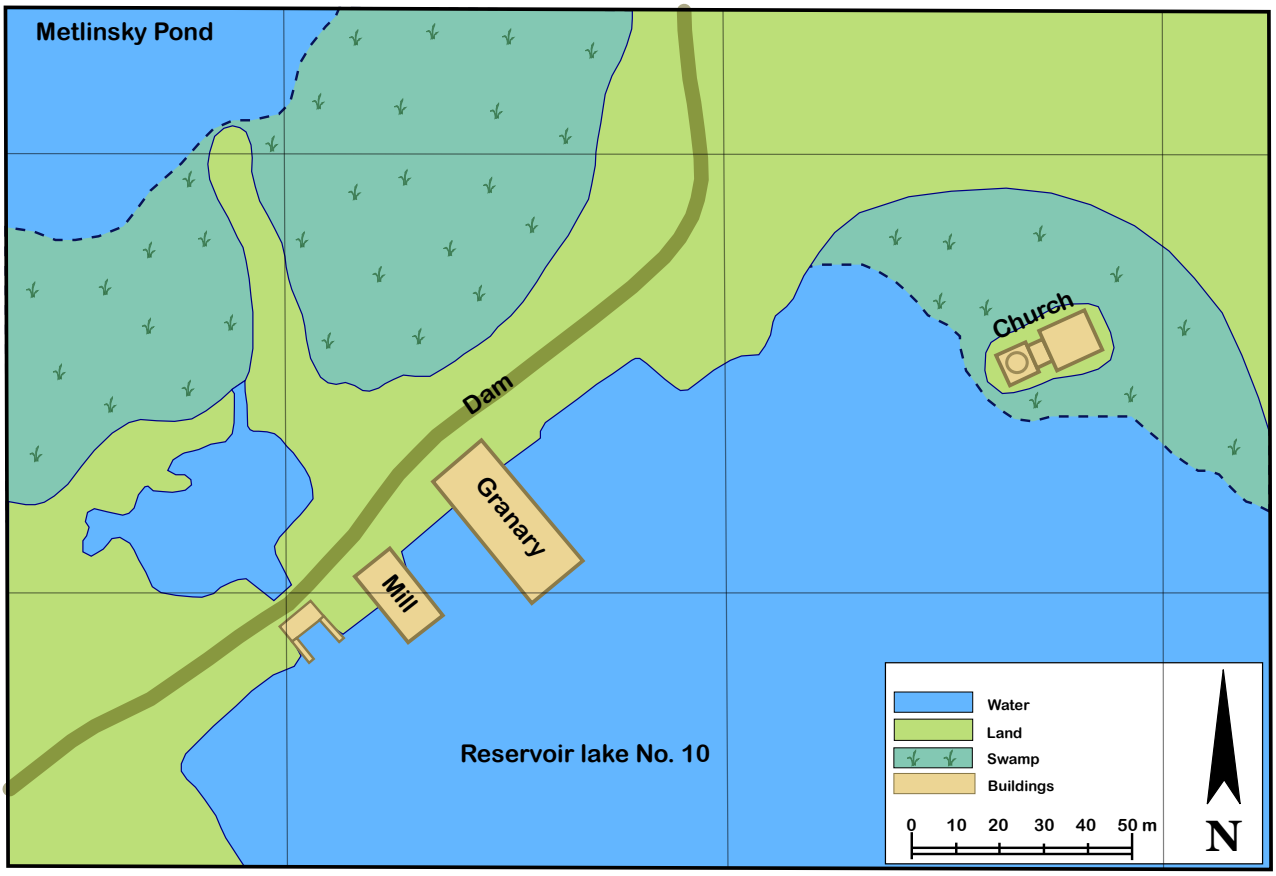

Figure 3.1: Metlino Site

This sketch shows the former village of Metlino as it is seen today. The top left shows a lake called *Metlinski pond* separated from the *reservoir lake R10* in the bottom by a dam. On the shore of the dam towards the reservoir lake are the remains of the former mill and granary as well as a modern weir to control the flow from the Metlinski pond to the reservoir lake. To the right of the dam is the church with its tower. [Courtesy of A. Ulanovsky]

a. Church **b.** Mill and granary **c.** Granary

Figure 3.2: Remaining Buildings in Metlino

The pictures show the site of Metlino as seen in the Field trips. **a:** View of the church from the dam (2011). **b:** View from the church tower to the remaining front walls of the mill, left, and granary, right (2011). The distance between the church and the mill is about 100 m. **c:** Front view of the granary (2012).

3.1 Geometrical Dose Rate Mapping at the Church Tower

Dose rate mappings were performed in the vicinity of the church tower to investigate the spatial distribution of the contamination (see Fig. 3.3). The measurements were performed with a hand held Automess dose rate meter (see section 2.3) at a height of 1 m over ground. At each location, the dose rate was integrated over a time of typically 0.5 – 2 minutes. The dose rates were corrected for a background dose of 0.08 $\mu Sv\,h^{-1}$ and converted to $\mu Gy\,h^{-1}$ using the coefficient derived in section 2.3.
The distance between the measurement points was determined with a laser range meter.

The dose rate in the area around the church was measured during the 2012 field trip. A grid of measurement points with a distance of 5 m was laid out in the swampy part North of the church tower. The reference point for the grid was sampling position C14 at the church tower (see section 3.2). The measured area ranges up to a distance of 50 m from the church tower. On the West, the grid reaches the shore line of the reservoir lake.
During the 2013 field trip, some measurement points were measured again with a dose rate meter. During a field trip in 2008 within the EU project SOUL, the dose rate was also measured at selected spots.
Fig. 3.3 shows the location and results of the dose rate measurements. The 2012 measurements are given in black, the 2013 measurement in red and the 2008 measurements in green.

To the South of the church, the landscape is very rough with steep edges and trees. After a few meters distance from the church tower the reservoir lake starts. The reference point for measurements is sampling position C16 at the church tower. It was not possible to measure on a 5 m grid there, horizontal distances between measuring points had to be adjusted according to terrain accessibility and are indicated in Fig. 3.3. The vertical distance is 2.5 m. The measurements were continued up to a few meters into the lake. The approximate water depth in cm is shown in blue in figure 3.3.

The 2012 dose rate measurements show higher doses rates than the 2008 and 2013 measurements, but the relative trend of lower doses in areas further apart from the reservoir lake is similar. Adjacent dose rate measurements with similar values were grouped to larger patches to reconstruct the sources for the reservoir model (see section 4.4.2).
The distance measurements were used to reconstruct the geometry of the site (see section 4.4.2).

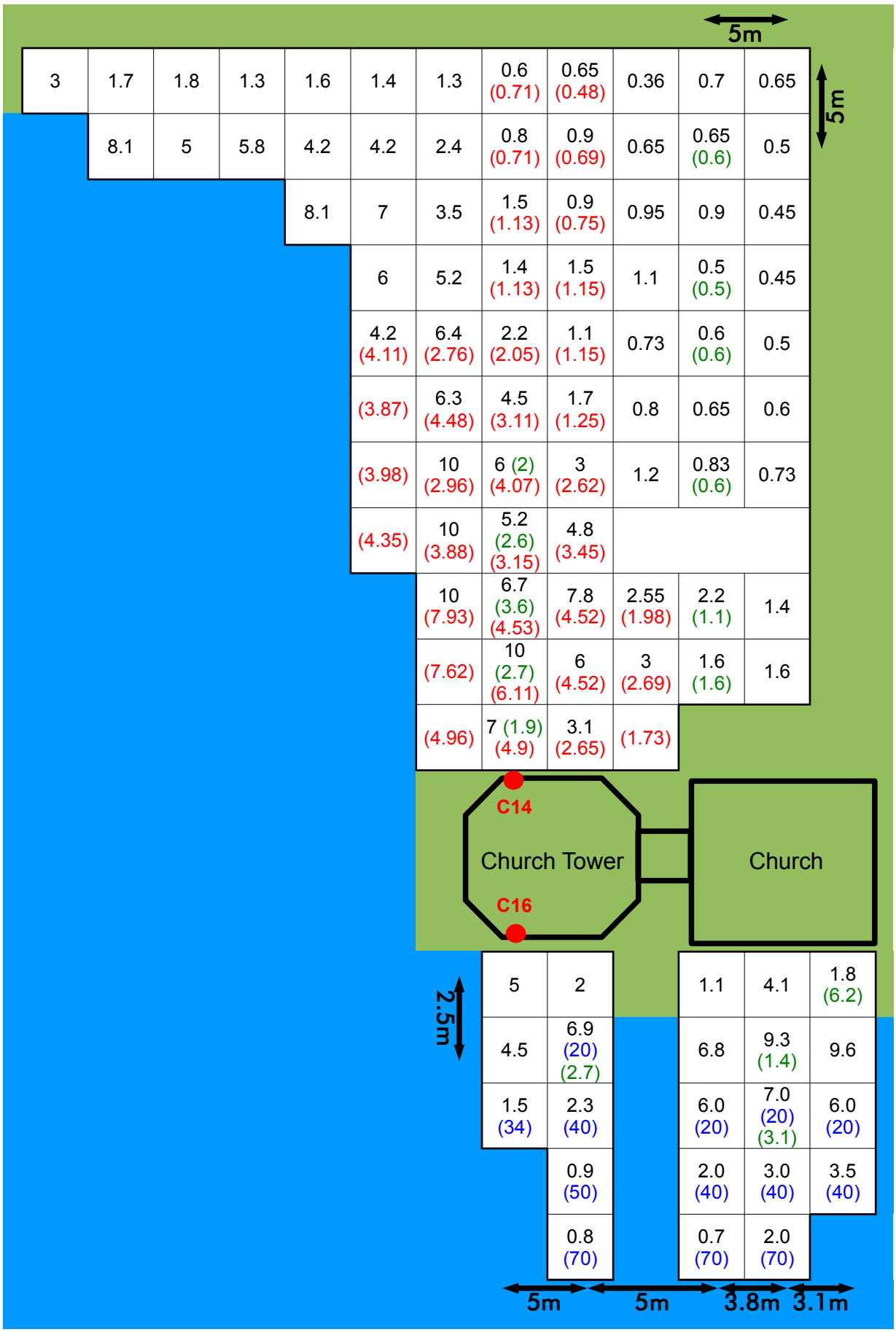

Figure 3.3: Dose Rate Measurements at the Church Tower

The location and measured dose rates in $\mu Gy\,h^{-1}$ around the church tower are shown in this figure. Black numbers indicate measurements during the 2012 field trip, measurements from 2008 are given in green, and measurements performed in 2013 in red. The water depths in cm at the sampling sites South of the church tower is shown in blue.

3.2 Sample Collection at the Church Tower

The church tower overlooks the geometry at Metlino. The North side faces towards the nowadays contaminated swampy part while the South-Western and South-Eastern walls face towards the former bed of the Techa river. From the church tower, samples were taken from three walls, facing in various directions at different heights.

Brick samples were taken from the church tower from three different heights: From the ground floor at 3.6 m, from the 2nd floor at 11.8 m and from the 4th floor at 19.6 m. One sample, C21, was taken at a height of only 1.25 m. At each story, samples from different walls all around the church tower were taken to cover a wide area of the Metlino geometry. See figure 3.4 and table 3.1 for the precise location and listing of all sampling sites. Pictures of all sampling sites are shown in appendix C.
The height profiles can give insight in the spatial distribution of the source and the distance of the source from the church tower.

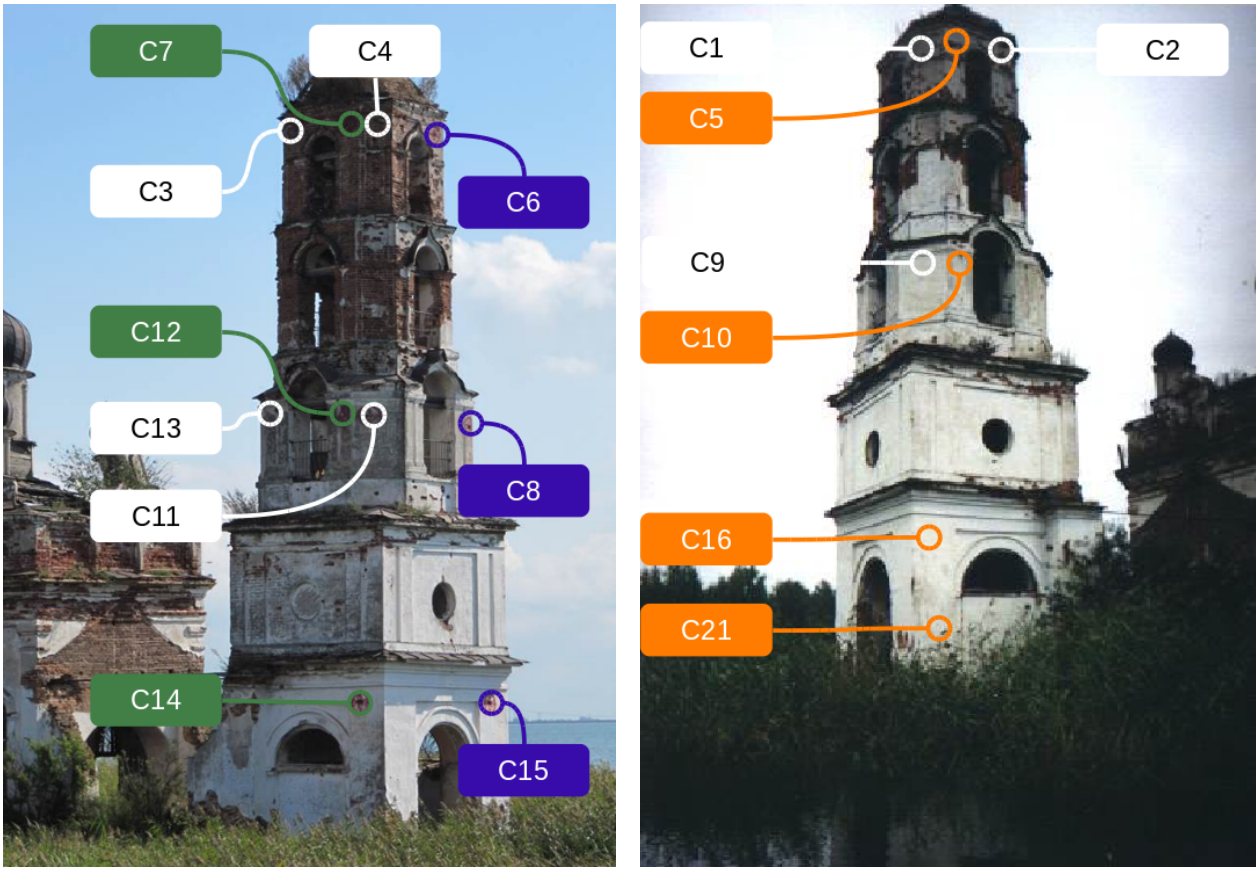

a. North side **b.** South side

Figure 3.4: Brick Sample Locations
The images show the brick sample positions at the church tower. Three height profiles are indicated: The green profile at the North side faces towards the swampy area contaminated nowadays. The blue and the orange profile on the South-West and South-East side face towards the former bed of the Techa river.

At each of the sampling sites, a brick sample was extracted (see Fig. 3.5). The bricks were transferred to the lab and analyzed there with TL and OSL methods (see section 2.5.1).
At selected locations, TL dosimeters were placed in drill holes in adjacent bricks. In general, four dosimeters were inserted around one extracted brick sample. Two types of casing materials were used to cover the TLD: Cu and Al (see section 4.1). On each sampling site, one TLD in a Cu and three TLD in an Al case were installed in 2011 and retrieved in 2012.

The brick samples collected show the total accumulated dose (see section 2.5). The TLD measurements show the current dose accumulated during one year. It is shown later, that these measurements and the associated simulations can be used to reconstruct the anthropogenic dose in brick for the years before the evacuation of Metlino, 1949 – 1956 (see chapter 5).

Floor	Wall	Height (m)	Sample number
Ground floor	North	3.6	C14* C20
	West	3.6	C15*
	South	3.6	C16*
	South	1.3	C21
2^{nd} floor	North-East	11.8	C13
	North	11.8	C12*
	North-West	11.8	C11*
	West	11.8	C8*
	South-West	11.8	C9
	South	11.8	C10*
4^{th} floor	North-East	19.6	C3
	North	19.6	C7*
	North-West	19.6	C4
	West	19.6	C6*
	South-West	19.6	C1 C18
	South	19.6	C5*

Table 3.1: Sample Locations
The table shows the location of all sampling sites at the church tower. At all sites, brick samples were taken, at selected sites, TL dosimeters were installed (marked with an asterisk).

Figure 3.5: Sampling Site at the Church Tower
The center of the picture shows a brick sample before its extraction. In the four drill holes around the brick, TL dosimeters were installed for one year.

3.2.1 Age of Buildings

Using TL measurements on background samples taken from the church in 1996, Degteva et al. [30] determined the church to have an age of 131 ± 26 years, thus it was built in between 1839 and 1891. This agrees well with the *Address-calendar of Ekatrinburg's eparchy for 1887* [103] that states that the church was constructed in 1861.

3.2.2 Results of the Brick Measurements

The brick samples were prepared and measured with TL and OSL techniques as described in section 2.5. The results of the OSL and TL measurements are shown in table 3.2.
In general, the OSL measurements produced results that agree between the different aliquots. For Sample C10 however, the OSL measurements produced different results that did not agree with each other. Therefore, for this sample, the TL measurement was used for the calculations.

On a first sight, green profile in Fig. 3.4 with samples C14, C12 and C7 that is facing towards the swampy area in front of the church, shows a distinct height profile of 2140 ± 146 mGy, 969 ± 48 mGy and 797 ± 47 mGy. In contrast, the samples C15, C8 and C6 of the blue profile with 864 ± 45 mGy, 979 ± 49 mGy and 886 ± 42 mGy and the samples C16, C10 and C5 of the orange profile with 1238 ± 55 mGy, 746 ± 63 mGy and 1129 ± 50 mGy show no distinct pattern. The profiles are further analyzed in section 5.1.3.

Sample	Depth (mm)	OSL (mGy)	TL (mGy)	Sample	Depth (mm)	OSL (mGy)	TL (mGy)
C1	10 ± 5	823 ± 49	850 ± 49	C11	10 ± 5	1134 ± 50	1624 ± 59
	21 ± 5	688 ± 45	720 ± 48		30 ± 5	807 ± 39	
C2	12 ± 5	800 ± 47	725 ± 45		50 ± 5	560 ± 29	
	20 ± 5	632 ± 41		C12	10 ± 5	969 ± 48	
C3	15 ± 5	479 ± 33	463 ± 33		30 ± 5	714 ± 43	
	26 ± 5	360 ± 29	346 ± 29	C13	10 ± 5	648 ± 37	
C4	15 ± 5	612 ± 36	607 ± 36		30 ± 5	438 ± 29	
	27 ± 5	597 ± 37	635 ± 39		50 ± 5	320 ± 22	
C5	10 ± 5	1129 ± 50		C14	10 ± 5	2140 ± 146	
	30 ± 5	780 ± 38			30 ± 5	1643 ± 82	
	50 ± 5	580 ± 33		C15	10 ± 5	864 ± 45	854 ± 45
	70 ± 5	448 ± 30			30 ± 5	598 ± 36	
C6	10 ± 5	886 ± 42			50 ± 5	428 ± 27	
	30 ± 5	602 ± 33		C16	10 ± 5	1238 ± 55	
	50 ± 5	434 ± 27			30 ± 5	811 ± 40	
C7	10 ± 5	797 ± 47			50 ± 5	582 ± 34	
	30 ± 5	546 ± 39		C18	10 ± 5	956 ± 52	
C8	10 ± 5	979 ± 49	850 ± 53		30 ± 5	766 ± 41	
	30 ± 5	667 ± 38		C20	10 ± 5	2622 ± 124	
	50 ± 5	508 ± 33			30 ± 5	1913 ± 89	
C9	10 ± 5	819 ± 96	805 ± 59	C21	10 ± 5	2323 ± 121	
	30 ± 5	674 ± 85	666 ± 87		30 ± 5	1656 ± 86	
	50 ± 5	456 ± 45	448 ± 33				
C10	10 ± 5	746 ± 63	1018 ± 57				
	30 ± 5	597 ± 47	729 ± 51				
	50 ± 5	250 ± 47	542 ± 36				

Table 3.2: Results of Dose in Brick Measurements
This table shows the dose accumulated in brick determined by OSL and TL measurements.

3.2.3 Results of the TLD Measurements

The TLD were analyzed as described in section 2.4. The absorbed dose of each TLD along with its type is shown in table 3.3.

In the majority of cases, the doses measured by the TLD with an Al casing showed good agreement within one sampling point, whilst the value for the TLD with the Cu casing is systematically lower. For reasons to be explained later in this work (see section 4.1), only the values of the Al cased dosimeters were considered. The averaged annual dose values of the dosimeters from each sampling site are shown in table 3.4.
Table 3.5 shows the time, the TLD were installed in the brick wall.

Sample	TLD Nr.	Housing material	Dose rate ($mGy\,a^{-1}$)	Sample	TLD Nr.	Housing material	Dose rate ($mGy\,a^{-1}$)
C5	1	Al	2.303	C11	21	Al	5.703
	2	Al	2.243		22	Al	6.044
	3	Al	1.822		23	Al	5.591
	4	Cu	2.294		24	Cu	4.668
C6	5		3.203	C12	25	Al	6.913
	6		3.287		26	Al	7.330
	7		2.037		27	Al	7.329
	8		2.803		28	Cu	6.267
C7	9	Al	5.993	C14	29	Al	13.014
	10	Al	5.818		30	Al	12.644
	11	Al	5.599		31	Al	13.145
	12	Cu	4.270		32	Cu	11.254
C8	13		3.488	C15	33	Al	4.075
	14		3.530		34	Al	4.067
	15		2.770		35	Al	3.914
	16		2.912		36	Cu	3.571
C10	17	Al	2.284	C16	37	Al	3.542
	18	Al	2.844		38	Al	3.293
	19	Al	1.920		39	Al	3.531
	20	Cu	2.670		40	Cu	4.725

Table 3.3: Results of TLD Measurements
This table shows an overview of the installed TL dosimeters at each sampling position of the church tower. The last column shows the dose rate in $mGy\,a^{-1}$. The values were corrected for background radiation as well as for radiation accumulated during transport.

As expected, the dose rates are much higher on the detectors C14, C12 and C7 facing towards the swampy area to the North of the church where the contamination is not covered by the water of the reservoir lake.
The detectors facing to the North of the church tower (green profile in Fig. 3.4) as well as the detectors facing towards the reservoir lake (blue and orange profile) show a decreasing dose rate with the height, a factor of 2.3 for the green profile, a factor of 1.5 for the blue profile and a factor of 1.9 for the orange profile between the highest and the lowest sample on each profile.

Sample	Dose (mGy)
C5	1.42 ± 0.26
C6	2.13 ± 0.57
C7	5.10 ± 0.20
C8	2.47 ± 0.39
C10	1.65 ± 0.47
C11	5.08 ± 0.24
C12	6.49 ± 0.24
C14	12.23 ± 0.26
C15	3.32 ± 0.09
C16	2.75 ± 0.14
C20	12.23 ± 0.24

Table 3.4: Annual Dose Measured with TLD
The annual dose at the sampling site in mGy averaged over the three dosimeters with Al case.

TLD Nr.	Deposition	Retrieval	Storage time (years)	Measurement
01 – 12	13.09.2011	18.09.2012	1.016	24.09.2012
13 – 24	14.09.2011	19.09.2012	1.016	24.09.2012
25 – 28	15.09.2011	19.09.2012	1.014	26.09.2012
39 – 40	16.09.2011	20.09.2012	1.014	26.09.2012

Table 3.5: Installation Time of TLD
This table summarizes the time each TLD was installed in the brick wall as well as the date of their analysis.

3.2.4 Results of the Dose Rate Measurements at the Church Tower

The current dose rate at the brick sampling positions of the church tower was measured with the hand held Automess dose rate meter during the 2011 and 2012 field trips (see Tab. 3.6). Also some measurements were performed in a 2008 field trip. The measurements were corrected for the background dose of 0.08 $\mu Sv\,h^{-1}$ and then converted to $\mu Gy\,h^{-1}$ using the coefficient derived in section 2.3.
The dose rate measurements from 2014 were provided by N. Bougrov, URCRM, Chelyabinsk, Russia. The measurements were performed with a DBG-06T professional device # 1166. The measurements were in micro Röntgen per hour and converted to $\mu Gy\,h^{-1}$. After this conversion, the measurement were also background corrected.

The dose rates measured in 2012 show higher values than the dose rates measured in 2011 and 2014. The measurements of 2014 are slightly higher than the measurements of 2011. This trend of dose rates measured at the church tower is in agreement with the trend seen in the dose rate measurements over ground where also the measurements from 2012 showed higher dose rates than the measurements from 2012 and 2008.

Sample	2008 ($\mu Gy\,h^{-1}$)	2011 ($\mu Gy\,h^{-1}$)	2012 ($\mu Gy\,h^{-1}$)	2014 ($\mu Gy\,h^{-1}$)
C1	0.23			
C2	0.04			
C3	0.21			
C4	0.13			
C5		0.05		0.19
C6		0.12		0.20
C7		0.29	0.87	
C8		0.17	0.56	0.27
C9		0.02	0.23	
C10		0.12		0.29
C11		0.27	0.87	
C12		0.27		
C14		0.80	1.69	
C15		0.23	0.61	0.32
C16		0.29	1.15	0.39
C21				0.66

Table 3.6: Current Dose Rates at the Church Tower
The table shows the current dose rates measured at the church tower from 2008, 2011, 2012 and 2014. The measurements were background corrected and converted to units of $\mu Gy\,h^{-1}$.

For these dose rate measurements, as for the dose rates estimated with the TLD, there is a decrease of the dose rate with the height. Comparing the highest with the lowest measured point of the 2011 measurements shows a factor of 2.7 between the dose rates of sample C14 and C17 (green profile in figure 3.4), a factor of 1.9 between the dose rates of sample C15 and C6 (blue profile) and a factor of 5.8 between the dose rates of sample C16 and C5 (orange profile). The different dose rate measurements performed at the church tower are discussed in section 6.3.

3.3 Geometric Measurements at the Church Tower

The geometry of the church tower was measured in great detail with a laser range meter (Stabila LE200, Stabila, Trifels, Germany. Precision: Distance up to 30 m: ± 2 mm, more than 30 m: ± 10 mm).

The first two floors have a rectangular shape, the upper three have an octagonal shape. From these measurements, a precise model of the geometry of the church tower was reconstructed (see section 4.4.1).

In each floor of the building, the following dimensions were measured (see Fig. 3.6):

- Inner diameter of the room in both directions.
- Outer diameter of the room in both directions.
- Width of the walls at each window.
- Dimensions of each window.
- Height of the room.
- Length of wall in the octagonal floors.
- Thickness of the floor plate.

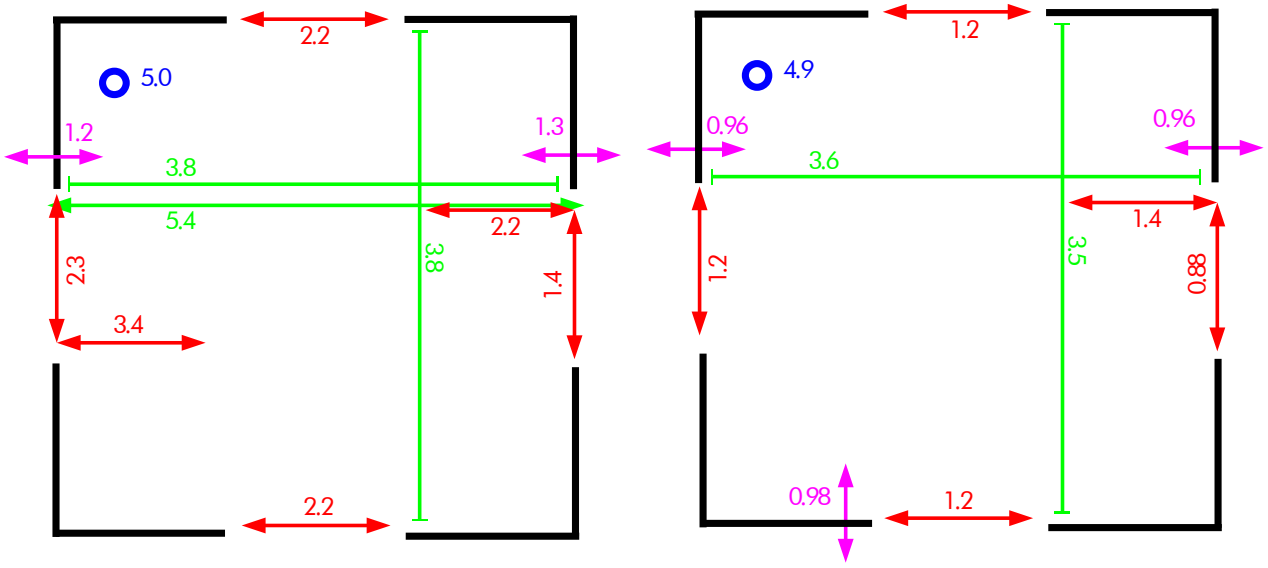

a. Ground floor **b.** 1st floor

Figure 3.6: Church Tower Dimensions, Part 1

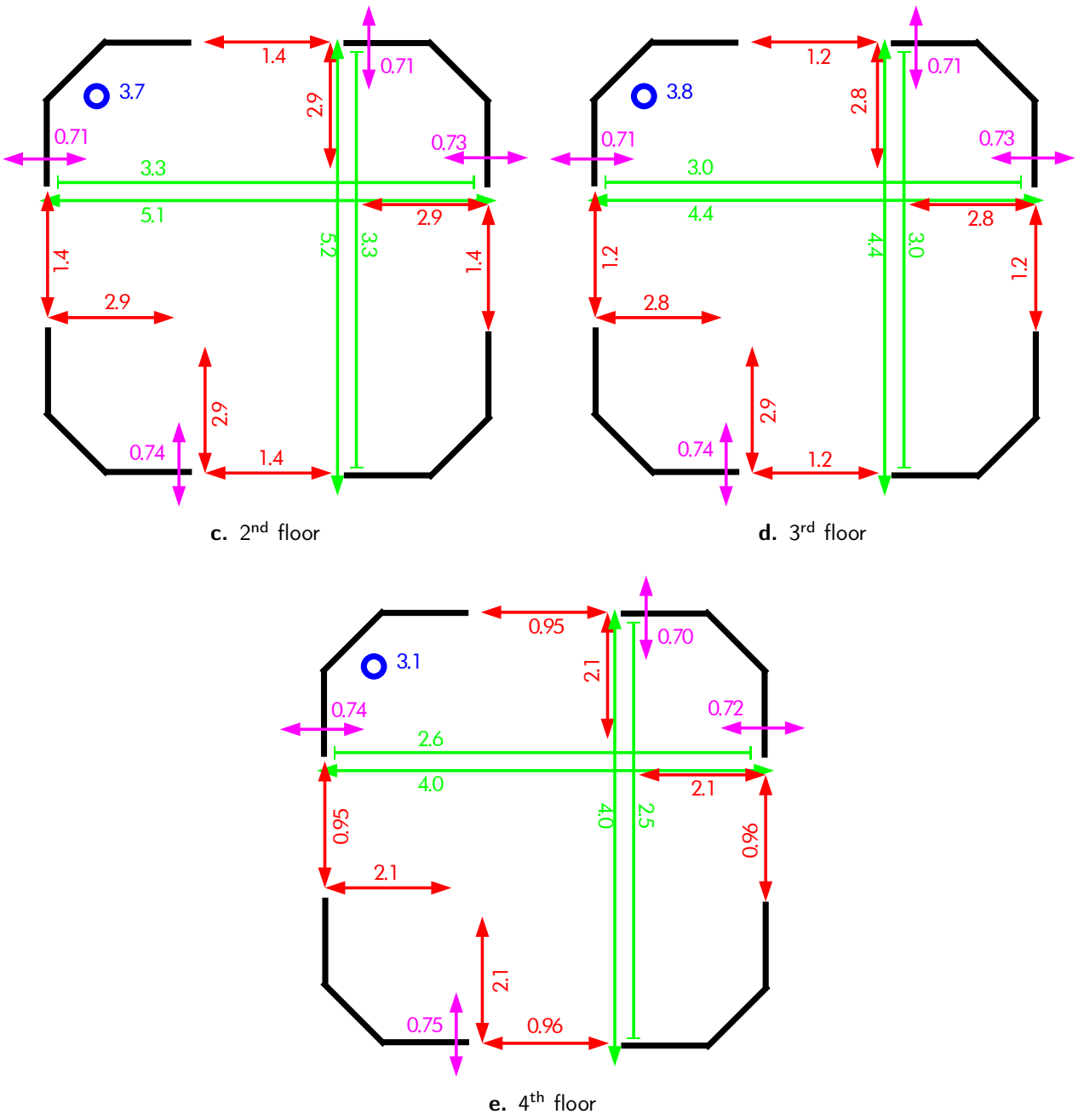

Figure 3.6: Church Tower Dimensions, Part 2
The pictures show the dimensions of the church tower that were measured with a laser range meter: The height of the wall (blue), the inner and the outer diameter of the room (green), the dimensions of the windows (red), and the thickness of the walls (pink). All distances are in units of meter.

3.4 Measurements at the Reservoir Lake

Figure 3.7 shows an aerial image of the Metlino area with the remaining walls of the mill and granary on the top, and the church tower on the right hand side. The center of the image shows the reservoir lake R10. The lake was crossed by boat along several transects starting near the church tower. Along the transects, the dose rate over the water and the water depth were measured every

few meters. Also, the activity of the soil at the bottom of the lake was measured with in-situ gamma spectroscopy (see section 2.7).

Figure 3.8 shows the results of the measurements. The measurements show a depth of the reservoir lake between 2.5 m and 4.5 m. The depth transect clearly show cavities in the ground of the reservoir lake. These cavities were identified as possible locations of the former beds of the arms of the Techa river (see section 4.4.3).

The activity of the bottom sediment of the lake is between 1 GBq m^{-2} and 2 GBq m^{-2}. There are drops in the activity of transects 1 and 2 at a distance of about 70 m. These were identified as an uncontaminated peninsula in the Metlino geometry before the creation of the reservoir lake (see section 4.4.3).

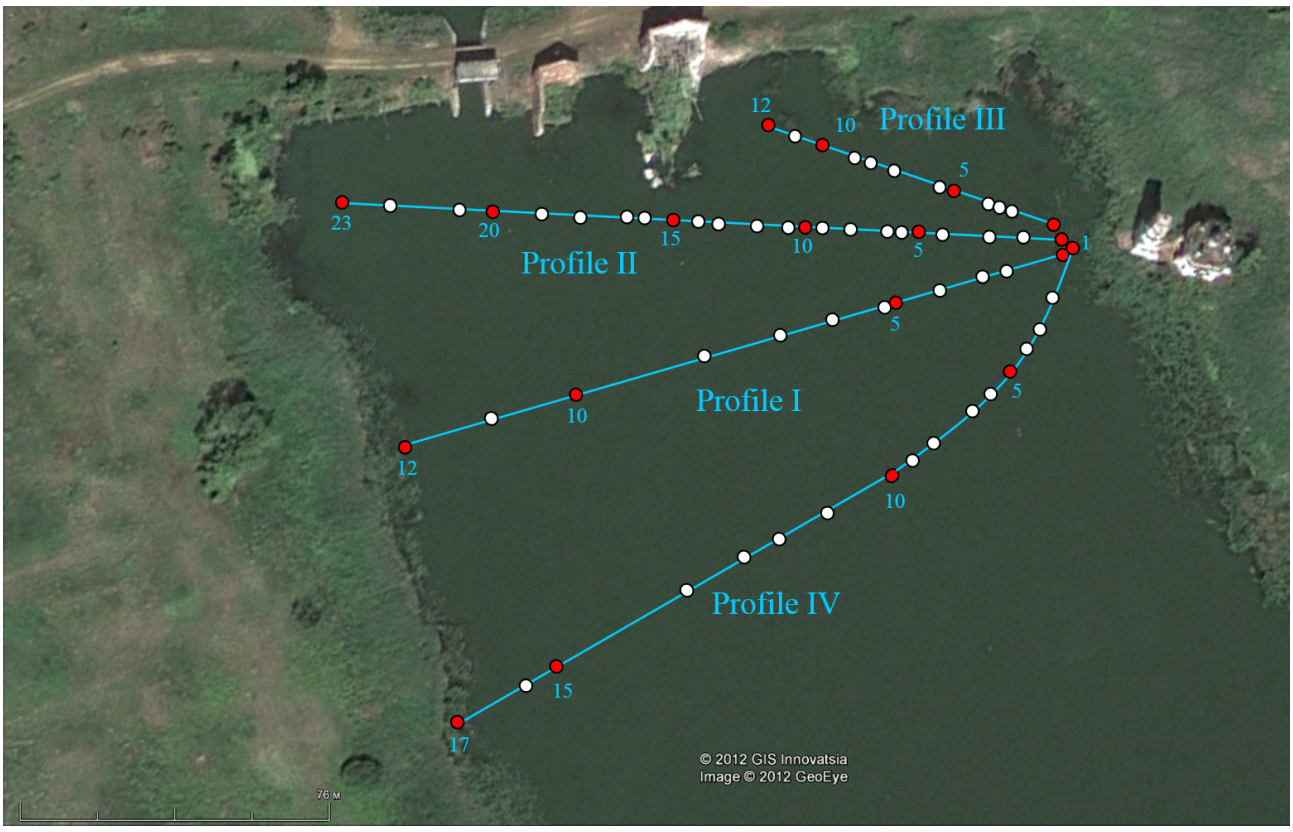

Figure 3.7: Measurement Points at the Reservoir Lake
The reservoir lake was crossed on several transects. Every few meters, the dose rate over the water, the water depth and the activity at the bottom of the lake were measured. © 2012 GIS Innovatsia. © 2012 GeoEye. © 2012 Google.

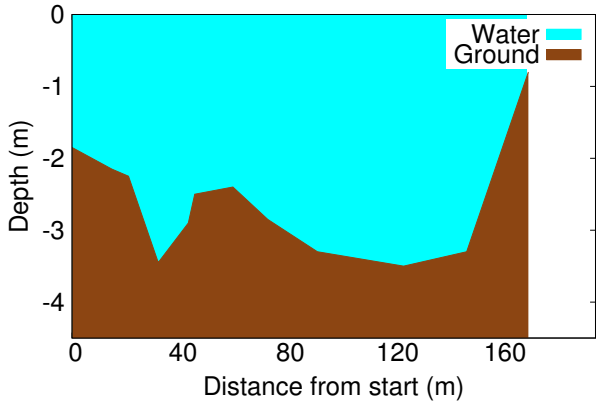

a. Transect 1, depth

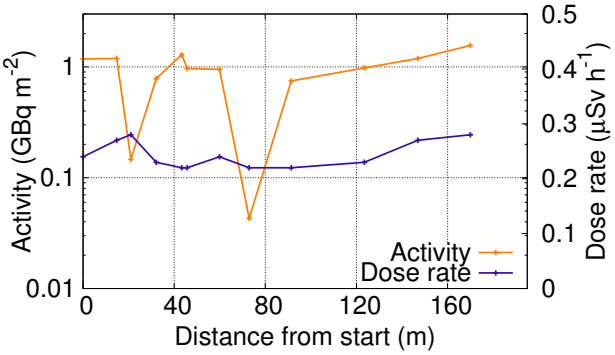

b. Transect 1, activity, dose rate

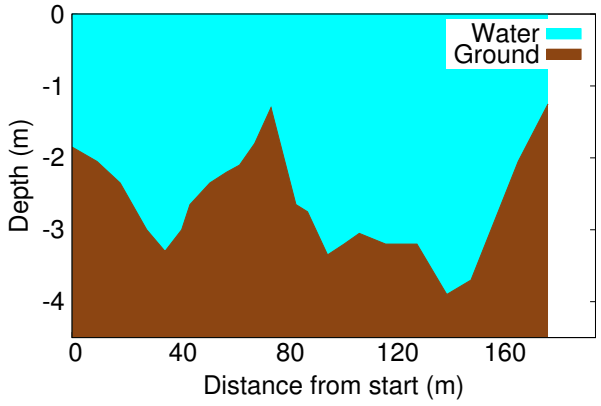

c. Transect 2, depth

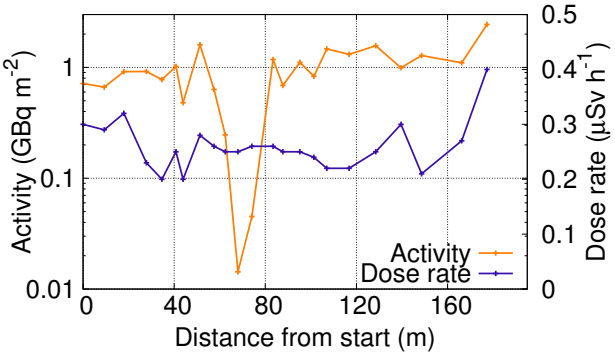

d. Transect 2, activity, dose rate

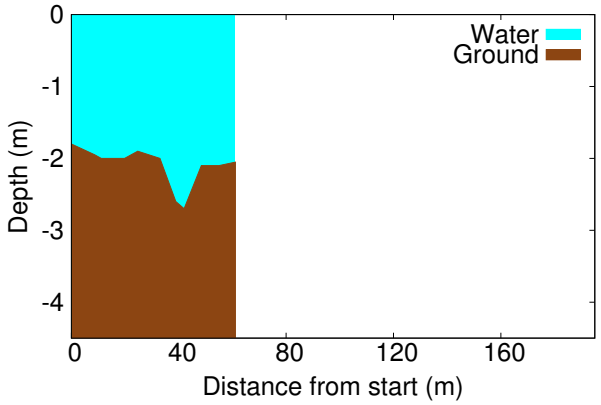

e. Transect 3, depth

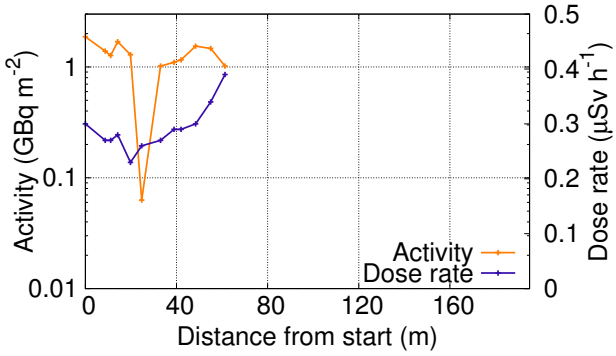

f. Transect 3, activity, dose rate

Figure 3.8: Transects Across the Reservoir Lake, Part 1

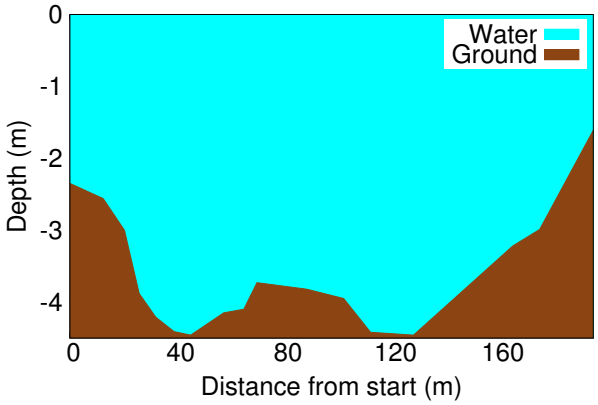

g. Transect 4, depth

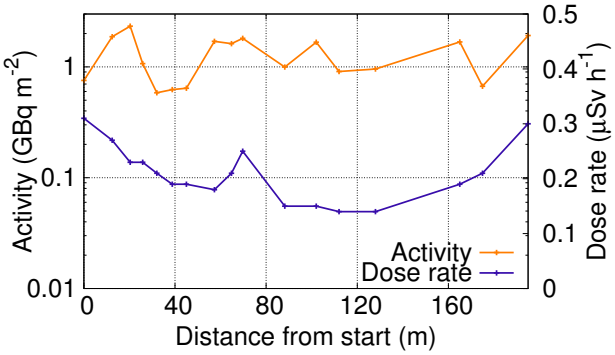

h. Transect 4, activity, dose rate

Figure 3.8: Transects Across the Reservoir Lake, Part 2
The plots show the results of the measurements along the transects across the reservoir lake. The left column shows the water depth, the right column gives the activity in GBq m^{-2} and the dose rate in µSv h^{-1}.

3.5 In-Situ Gamma Spectroscopy in Soil

In-situ gamma spectroscopy measurements in soil were performed during a field trip to Metlino in 2008. The area to the North of the granary and the church was sampled (see Fig. 3.9). At selected sites, boreholes up to a depth of 40 cm in the ground were drilled. Lowering a collimated detector into the drill hole, the depth distribution of the activity in the soil was evaluated for the radionuclides ^{137}Cs and ^{60}Co (see Fig. 3.10). These measurements were performed for two sampling sites in front of the granary, location 205 and 206 in figure 3.9.
Both sites show an uncontaminated layer on top, 5 cm for sample 205 and 2 cm for sample 206. They show a maximum of the activity at a depth of 10 cm in the ground, sample 205 with a maximal activity of 130 kBq kg^{-1} and sample 206 with a maximal activity of 500 kBq kg^{-1}. Both samples also show, that most of the activity is contained within a soil layer of up to 30 cm depth.

There were no measurements of this kind to the North of the church. The soil is expected to be similar in this region and thus, also the contamination pattern with the main activity in the first 30 cm of the soil is expected to be similar. But in contrast to the area North of the granary, the area in the North of the church tower is a floodplain and gets covered with water from time to time. Thus, a clean, uncontaminated layer in the first centimeters is not expected to be realistic in this scenario.

These measurements of the depth profile of the contamination helped to reconstruct the contamination pattern to the North of the church tower and thus to model the depth distribution of the source for the reservoir model (see section 4.4.2).

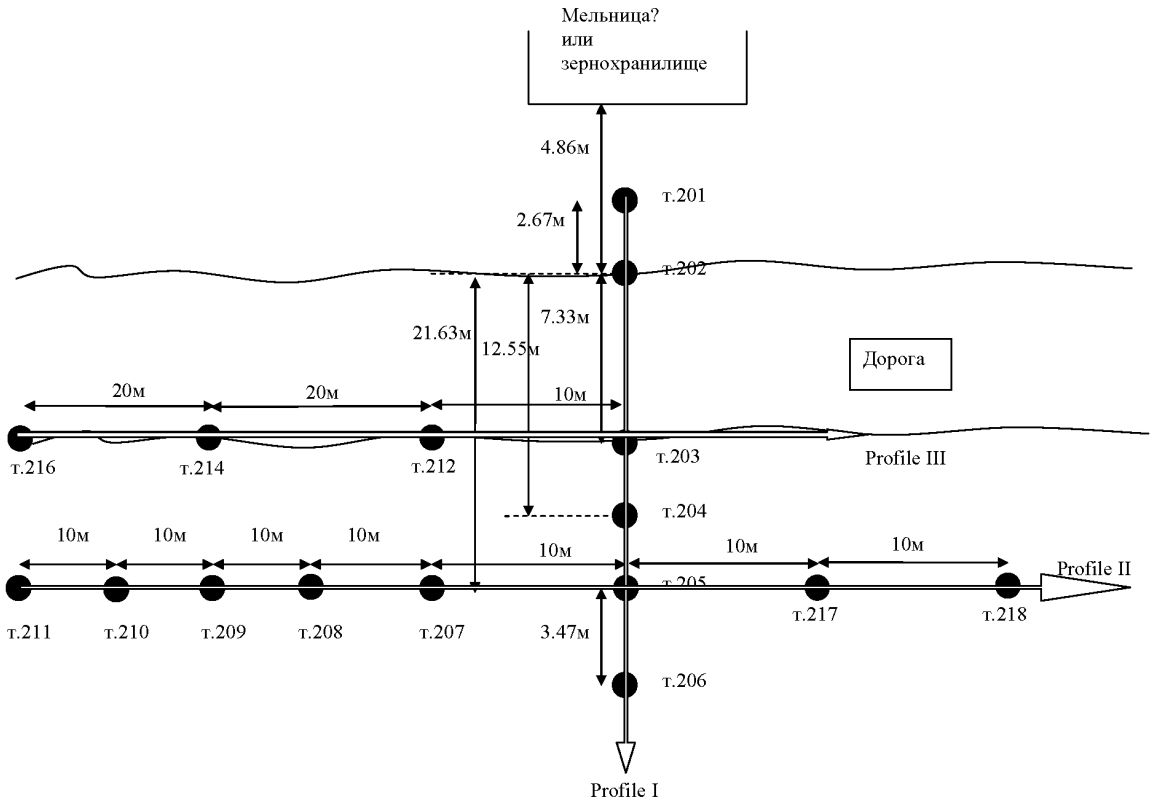

a. Granary

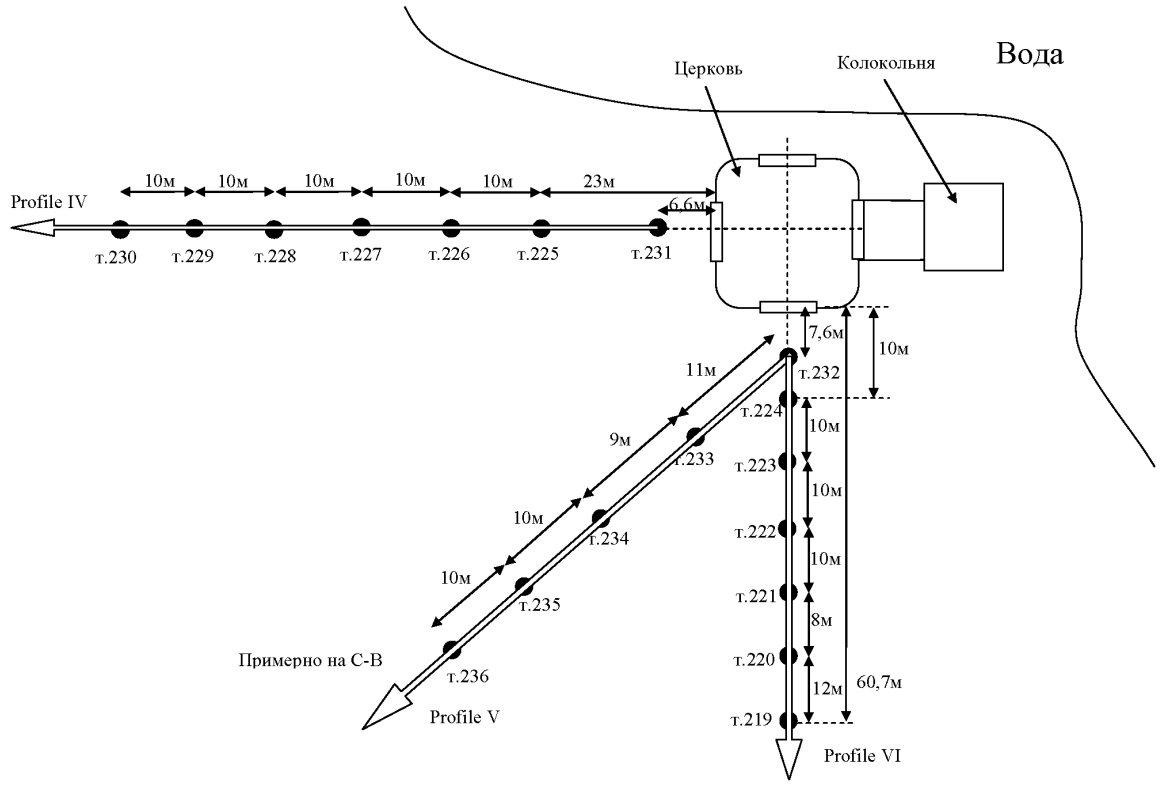

b. Church

Figure 3.9: Gamma Spectroscopy in Soil

These two sketches show the location of gamma spectroscopic measurements in front of the granary and the church tower. At sampling sites number 205 and 206 to the North of the granary, the depth distribution of the activity was measured.

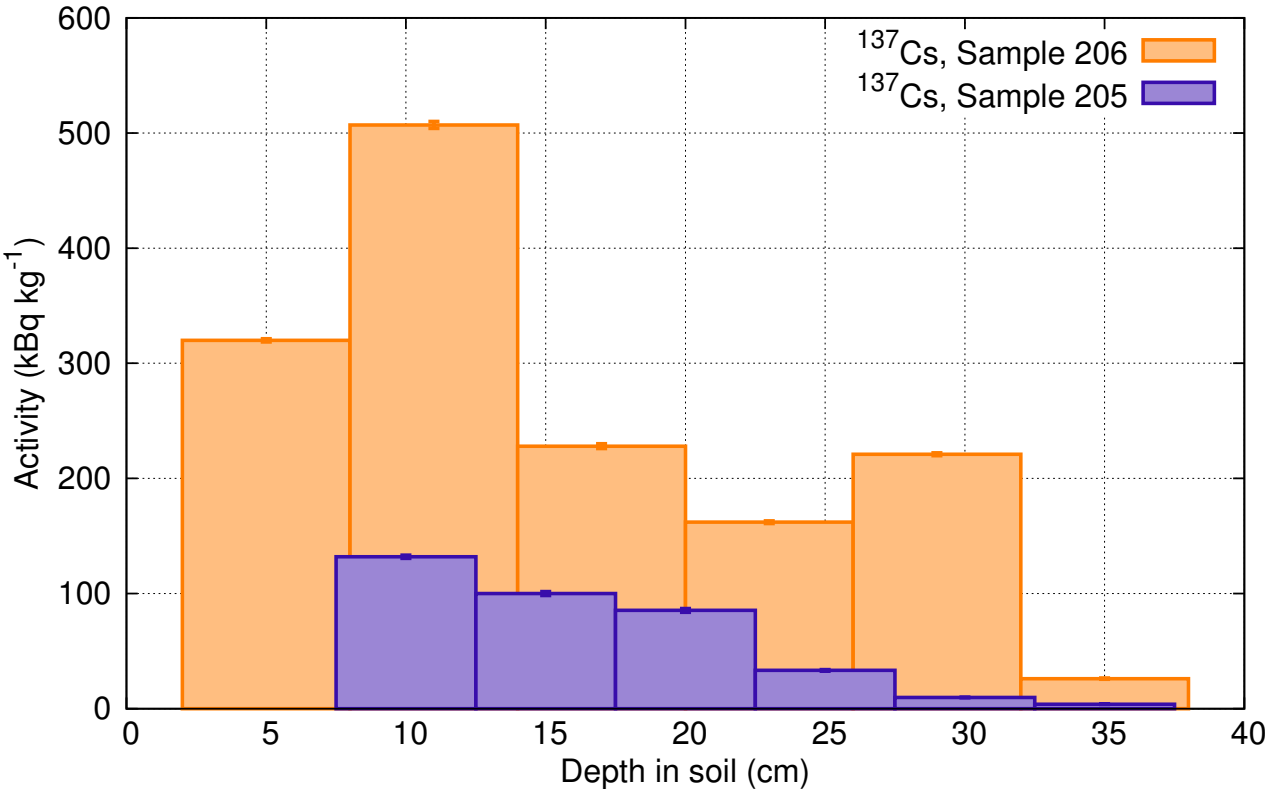

Figure 3.10: Activity Distribution in Soil

The depth distribution of the activity in soil was measured for the radionuclide ^{137}Cs. Both measurements show an uncontaminated layer on top and radioactivity down to a depth of 30 cm.

Chapter 4

Radiation Transport Simulations – Setup and Results

4.1 Conversion Factors Between Doses in Bricks and Doses in TLD Materials

In this work, doses accumulated in TLD (Al_2O_3) were used to derive the contemporary gamma dose rate in quartz containing bricks. The response of a brick to radiation is different to the response of a TLD to the same kind of radiation (particle type, energy distribution, angular distribution). To compare the doses accumulated in the brick and the doses of the TLD, dose conversion factors between doses in bricks and doses in TLD were calculated. Therefore, first the dose per air kerma was compared for photons in the energy range of 0.03 – 3.00 MeV. In a second step, the energy spectrum of a source in ground was calculated at various altitudes over ground. Finally, this photon spectrum was folded over the function of the energy dependence to establish the conversion factors. The calculations were performed for TLD with 3 mm Al- as well as for TLD with 1 mm Cu- housing.

4.1.1 Energy Dependence of the TLD Response

To evaluate the level of agreement between measured and simulated doses in TLD, the energy dependence between measured and simulated doses in TLD, and the energy dependence of the two different housings was first investigated in the lab.

The TLD were simulated in a simplified setup, with no brick environment and frontal irradiation. The TLD consisted of a cylindrical Al_2O_3 chip (see Tab. A.6), 1 mm thick and 5 mm in diameter (see Fig. 4.2), with a density of 3.97 g cm^{-3}. This chip was housed in a cylindrical shell. Two different types of shielding material were used, copper with a thickness of 1 mm (density 8.96 g cm^{-3}) and aluminum with a thickness of 3 mm (density 2.79 g cm^{-3}). The thicknesses of the shielding media are sufficient according to Aznar et al. [8].

The experiment was carried out using the same irradiation conditions in the energy range of 0.033

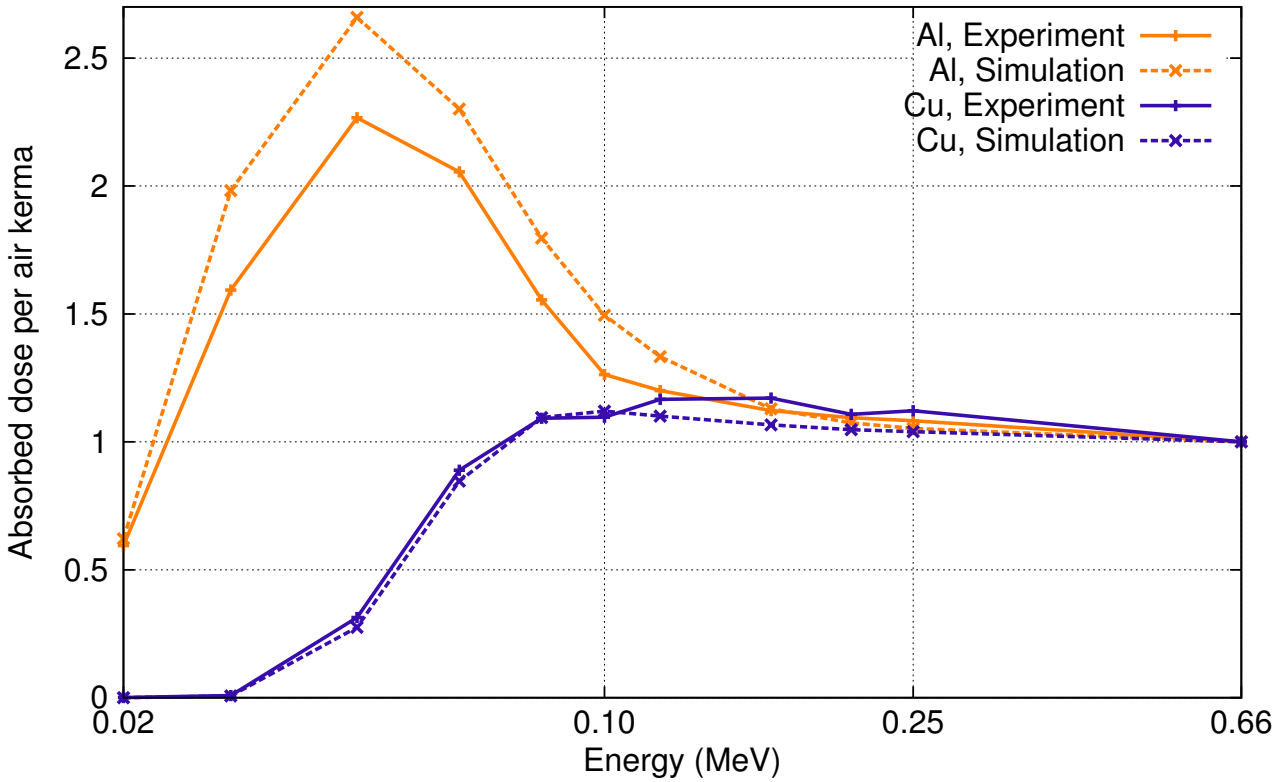

Figure 4.1: TLD Energy Dependence
The dose per air kerma was measured for Al- and Cu- covered TLD and normalized on 0.662 MeV. The experiments were verified by MCNP calculations.

– 1.250 MeV as for the dose rate meter (see section 2.3).
The ratio measured dose in the TLD relative to the air kerma at the detector position was calculated (see Fig. 4.1). The ratio of dose per air kerma was also simulated with MCNP for Al- and Cu-shielded TLD.
The calculations show an over estimation of the dose for Al- covered TLD for energies below 100 keV, while Cu covered TLD in this energy range strongly underestimate the dose. For higher energies, the dosimeters show equal doses.

Both the Al- and the Cu- covered TLD show a good agreement between each other for energies over 100 keV. In this energy range, also the simulated and the measured results agree. At high energies, the result is independent of the shielding material, the photons penetrate though. But for low energies, the material does matter and the ability of photons to penetrate depends e.g. on the atomic number of the material.
For lower energies the dose per air kerma rises gradually between 30 keV and 80 keV to a value of about 1.0 – 1.2 for the Cu shielded TLD. At the low energies, most photons can not penetrate the

Cu shield, almost all are stopped below 30 keV, so there is no dose in this range. With more and more photons penetrating the Cu shield, the dose rises. The simulated and measured results are in good agreement for the Cu shield.
For the Al shielded TLD, the curve peaks at 50 keV with values of 2.3 and falls then also to values of 1.0 – 1.2 for energies above 100 keV. For the case of Al, the experiment shows a lower dose per air kerma than the simulation, about 20 % at the peak position. A possible explanation for this effect could be the following: In the simulation, all incident radiation in the detector volume creates a corresponding dose. For the TLD, the dose that is generated for a certain incident radiation depends on the efficiency of the TLD towards the energy of the radiation. Low energies are related to a decreased TL efficiency with an increasing LET at these energies [64].
The discrepancy between the measured and calculated dose is also important for the conversion factor between dose in brick and dose in TLD shown in section 4.1.3.3.

4.1.2 Setup of the Simulation

4.1.2.1 Simulation of Brick and TLD

A large sphere was divided into two halves by a plane, one half containing the brick material, the other containing air (see appendix A for material definitions in MCNP). A drill hole was simulated in the brick, perpendicular to the interface between brick and air, and the radius of the drill hole was set to exactly contain the dosimeter. The material of the brick was simulated according to Taranenko et al. [99] (see Tab. A.3) with a density of 1.6 g cm^{-3}.
The TLD were simulated as described above (see also Fig. 4.2). The housing of the TLD was enclosed in a heat shrink tube (see Tab. A.7) with a density of 0.95 g cm^{-3}.
The TLD was placed 1 cm deep in the simulated drill hole in the brick.

A third, *brick only* configuration was prepared with only the brick half-sphere, not containing any TLD, where the scoring was performed in the same volume where originally the TLD chip was.

A layer of plaster was simulated on top of the brick with a variable thickness of 0.25 – 5 cm. The front of the drill hole was simulated to be filled with glue to keep the TLD in position, as it was done in the field, when the TLD were installed in the brick wall.

The source was on a circular plane with radius 100 cm to the left of the drill hole, aligned on its center. The source particles were sampled uniformly over the source area. The emitted photons were in the energy range of 0.03 – 3.00 MeV.
The volume of the TLD chip or the equivalent brick volume was scored using the *F8 tally.

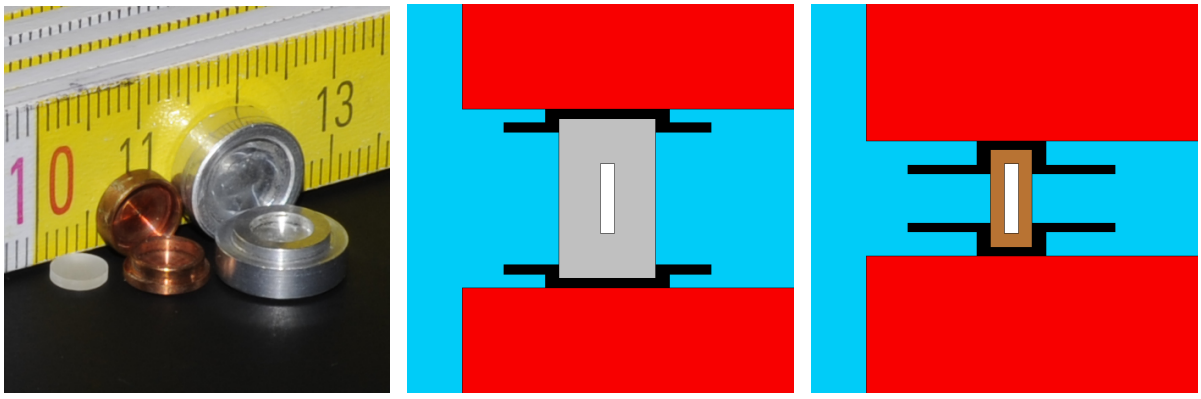

a. TLD chip, Cu- and Al- housing **b.** TLD with Al housing **c.** TLD with Cu housing

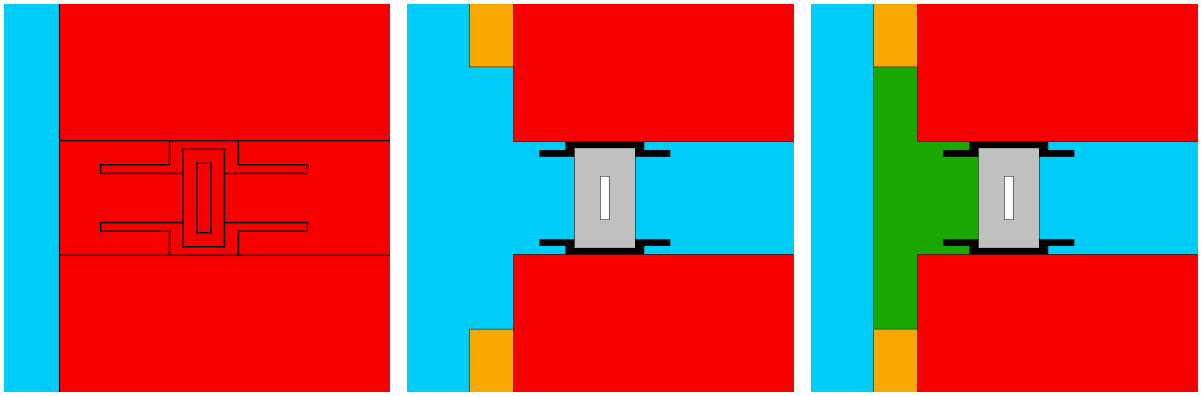

d. Brick only **e.** TLD and plaster on wall **f.** Glue in front of drill hole

Figure 4.2: Simulation of TLD

a: The Al_2O_3 chip (left) is encapsulated in a copper (middle) or aluminum housing (right). The TLD chip has a diameter of 5 mm.

The plots of the simulation setup show cross sections through the middle of the TLD, the source is on the left. **b:** Simulation of the TLD in the Al housing, 3 mm thickness. **c:** Simulation of the TLD in the Cu housing, 1 mm thickness. **d:** The *brick only* configuration where the brick volume at the location of the chip in the TLD configurations is sampled. **e:** A layer of plaster with variable thickness was attached to the brick wall. **f:** The front of the drill hole was simulated to be filled with glue. Color scheme: Brick: red, TLD: white, tube: black, Al-case: silver, Cu-case: brown, air: blue, plaster: orange, glue: green.

4.1.2.2 Simulation of the Spectrum Above Soil

A series of Monte Carlo calculations was carried out to evaluate the energy spectrum at different heights above the ground, produced by a source in soil.

The geometry consisted of a layer of soil at the bottom, with a layer of air on top. The air was simulated as shown in table A.1.

The simulation was performed for two soil types, the soil suggested in Eckerman and Ryman [37] with a density of 1.6 g cm^{-3} and the soil suggested in Saito and Jacob [92] with a density of 1.0 g cm^{-3}. The elemental composition for the two soil types is shown in table A.2.

The results of both soil types were compared and shown to produce similar results. For the following calculations, the soil according to Eckerman and Ryman [37] was used. The difference between the soil types is discussed in section 6.1.1.

The source distribution in soil was uniform up to a depth of 30 cm. The source emitted photons in the range of 0.03 – 3.00 MeV.
The flux of photons crossing surfaces in air was scored. The scored surfaces were in heights of 1 m to 100 m above the ground.
The spectrum was recorded in equally spaced bins on a log scale in the range of 0.03 – 3.00 MeV.

4.1.3 Determination of the Conversion Factors

4.1.3.1 Doses in Brick and TL Dosimeters

The dose simulated in the detector was divided by the air kerma [83] of the appropriate energy using the mass energy-absorption coefficient tables provided by Hubbel and Seltzer [49].

The air kerma per source photon was calculated as

$$K_{air}(E_s) = \frac{1}{A_s} \cdot \frac{\mu_{en}}{\rho}(E_s) \cdot E_s, \tag{4.1}$$

where A_s is the source area, E_s the energy of the source photons and $\frac{\mu_{en}}{\rho}(E_s)$ the mass energy-absorption coefficient.

The ratio R of dose in the material to the air kerma calculates as

$$R_{TLD}(E_s) = \frac{D_{TLD}(E_s)}{K_{air}(E_s)} \tag{4.2}$$

and

$$R_{brick}(E_s) = \frac{D_{brick}(E_s)}{K_{air}(E_s)}, \tag{4.3}$$

with $D_{TLD}(E_s)$ and $D_{Brick}(E_s)$ the dose calculated by MCNP in the TLD and in the brick.

The dose per air kerma for the brick (green curve in Fig. 4.3) shows a peak at small energies, with a maximum ratio of dose per air kerma of more than 2.5 at 0.06 MeV. The curve of the Cu-shielded TLD (blue) does not show this behavior at small energies. The ratio rises quite steeply from 0 to a constant 0.8 in the range of 0.05 – 0.1 MeV. The curve for the Al-shielded TLD (orange) follows the peak of the brick at 0.06 MeV up to a level of almost 1.5. The slope is steeper for the Al-shielded TLD than for the brick in the region of 0.01 – 0.03 MeV.

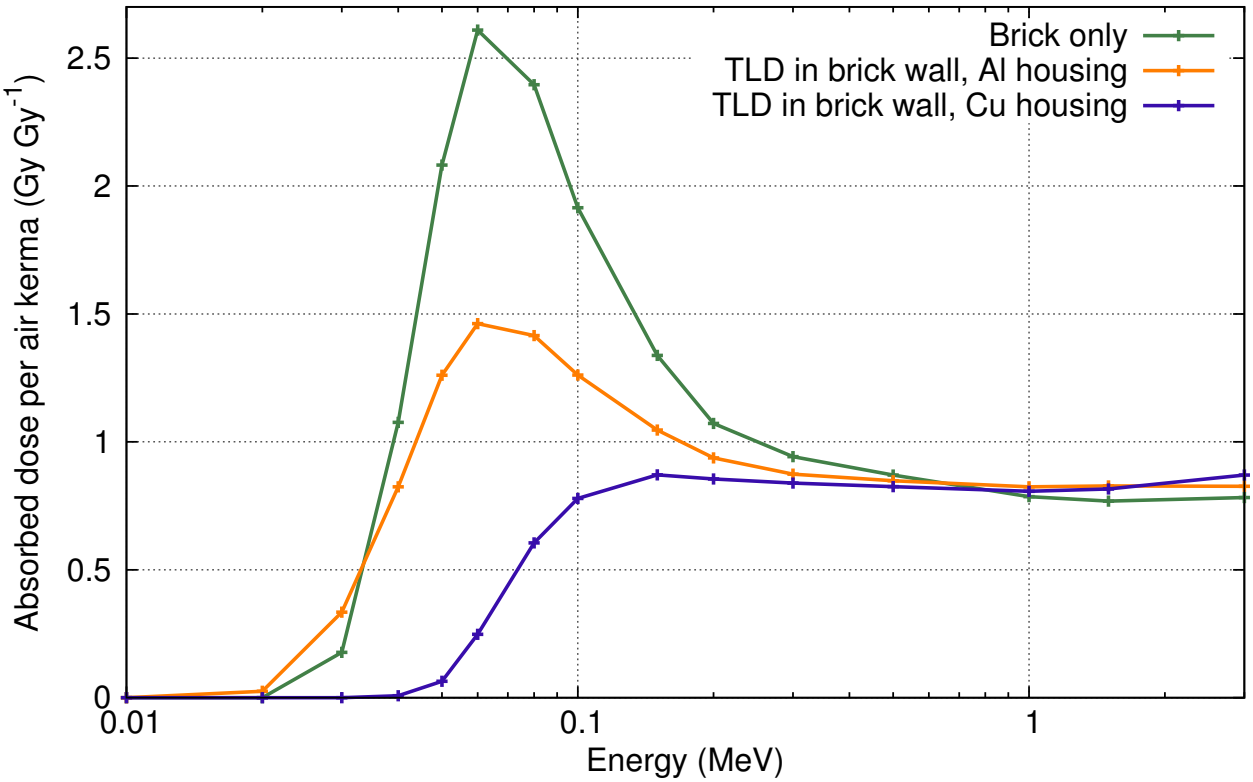

Figure 4.3: Absorbed Dose per Air Kerma
This plot shows the dose per air kerma of brick samples compared to Cu- and Al- shielded TLD. The brick shows a higher response for low energy photons, while they have similar ratios at energies above 0.1 MeV.

For higher energies, above 0.10 MeV up to 3.00 MeV, the ratio is nearly constant: All three curves meet at a dose per air kerma ratio of about 0.7 – 0.8.

For low energies, the same effect as shown in section 4.1.1 accounts. For the Cu shielded TLD, the photons are stopped in the shield, thus the Cu curve only starts at about 50 keV, gradually rising up to a constant factor of about 0.8 at 100 keV. The Al shield does not stop the photons that drastically and the curve for the Al- shielded TLD also shows a peak at low energies.
For free TLD, a ratio of 1 would be expected, at least for higher energies. But these TLD are inserted 1 cm deep into the brick. The brick absorbs the radiation and reduces the dose per air kerma to a factor of about 0.8.
It can be seen that the energy response of the Al shielded TLD better reproduces the energy response of the brick than the Cu shielded TLD. This can be because Al corresponds better to the density and material of the brick. Al has a density of 2.79 g cm^{-3}, brick a density of 1.6 g cm^{-3}, the density of Cu is much higher, 8.96 g cm^{-3}. Also, the brick consists of various light elements (see Tab. A.3). Simulations were carried out with the heavy elements like Fe, Ti, etc. removed from the brick

composition. These simulations showed an even better agreement between the curves for the Al shielded TLD and the brick dose.
The brick dose in the wall can only be calculated, not measured. The brick could also underestimate the dose from the low energy photons as it is done by the TLD chip (see section 4.1.1). This uncertainty has to be taken into account, when considering the conversion factor.

4.1.3.2 Spectra Above Soil

The simulated energy spectrum is described by the fluence at energy E, for a source energy E_s and at altitude h:

$$\phi(E_s, E, h). \tag{4.4}$$

The spectrum was recorded in various altitudes above ground in the range of 1 – 100 m. An exemplary plot, for the source energy of ^{137}Cs with 0.66 MeV in ground and the altitudes of 1 m (position of lowest sample at the church tower) and 20 m (position of highest sample) is shown in figure 4.4.

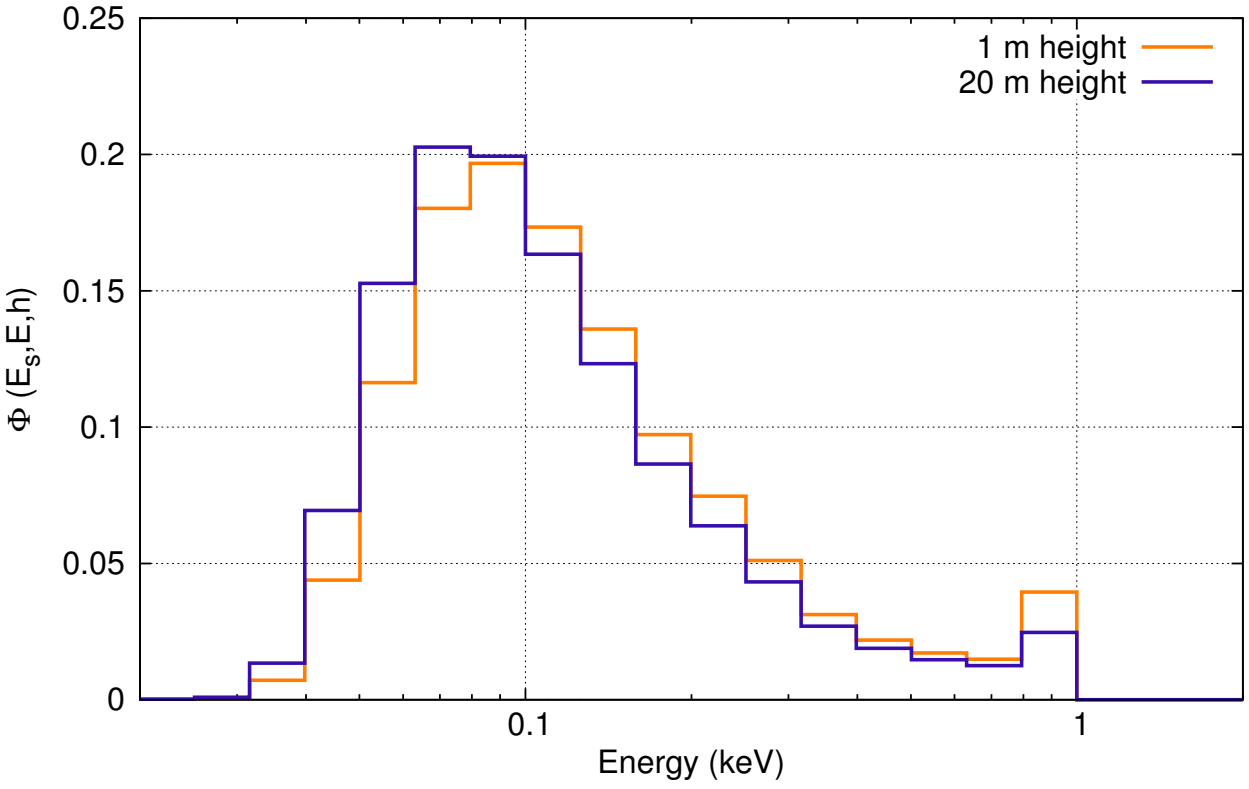

Figure 4.4: Spectrum Above Soil
The calculated spectrum of a monoenergetic photon source in soil with an energy of 0.66 MeV at the altitudes of 1 m and 20 m above ground was simulated.

4.1.3.3 Conversion Factors Between Doses in Brick and Doses in TLD

With the ratio between the simulated dose in the brick or the TLD to the air kerma and with the energy spectrum of a mono energetic source in soil, the conversion factors between the dose in TLD and the dose in brick can be calculated.

The conversion factor gives the ratio of the integrated dose in TLD, $D^{int}_{TLD}(E_s)$ to the dose in the brick, $D^{int}_{brick}(E_s)$ depending on the source energy E_s. The dose for TLD and brick was calculated as:

$$D^{int}_{TLD}(E_s) = \int dE\ R_{TLD}(E_s)\ \cdot\ \phi(E_s, E, h)\ \cdot\ \frac{\mu_{tr}}{\rho}_{air}(E_s) \cdot\ E \tag{4.5}$$

and

$$D^{int}_{brick}(E_s) = \int dE\ R_{brick}(E_s)\ \cdot\ \phi(E_s, E, h)\ \cdot\ \frac{\mu_{tr}}{\rho}_{air}(E_s) \cdot\ E. \tag{4.6}$$

The conversion factor between the dose in TLD and the dose in brick calculates as

$$CF(E_s) = \frac{D^{int}_{TLD}(E_s)}{D^{int}_{brick}(E_s)}. \tag{4.7}$$

The resulting curve of the conversion factor between the dose in an Al- or a Cu- shielded TLD and the brick is shown in figure 4.5 for the altitudes of 1 m and 20 m over ground.
For the source energy of ^{137}Cs of 0.622 MeV, the conversion factors for the Al- and Cu- shielded TLD are given in table 4.1.

Height	**1 m**	**20 m**
CF_{Al}	0.83	0.80
CF_{Cu}	0.63	0.56

Table 4.1: Conversion Factor
The conversion factor between the dose in TLD and the dose in brick for the heights of 1 m and 20 m above ground and the source energy of 0.622 MeV.

As expected from figure 4.3, the value for the Al shielded TLD is closer to one than for the Cu shielded TLD. But there is still a difference of about 20 % between the brick and the Al shielded TLD. Nevertheless, a clear improvement in matching TLD and brick response is observed when using the Al shielding instead of the Cu shielding. For this reason, only the results from the Al shielded TLD were used for analysis throughout this work.
This conversion factor is attributed with several uncertainties: There is an uncertainty towards the response of the brick at low doses, the brick has only been simulated, not measured. As it was shown before, this causes a maximal error of 20 %. There is a difference in the conversion factor with the

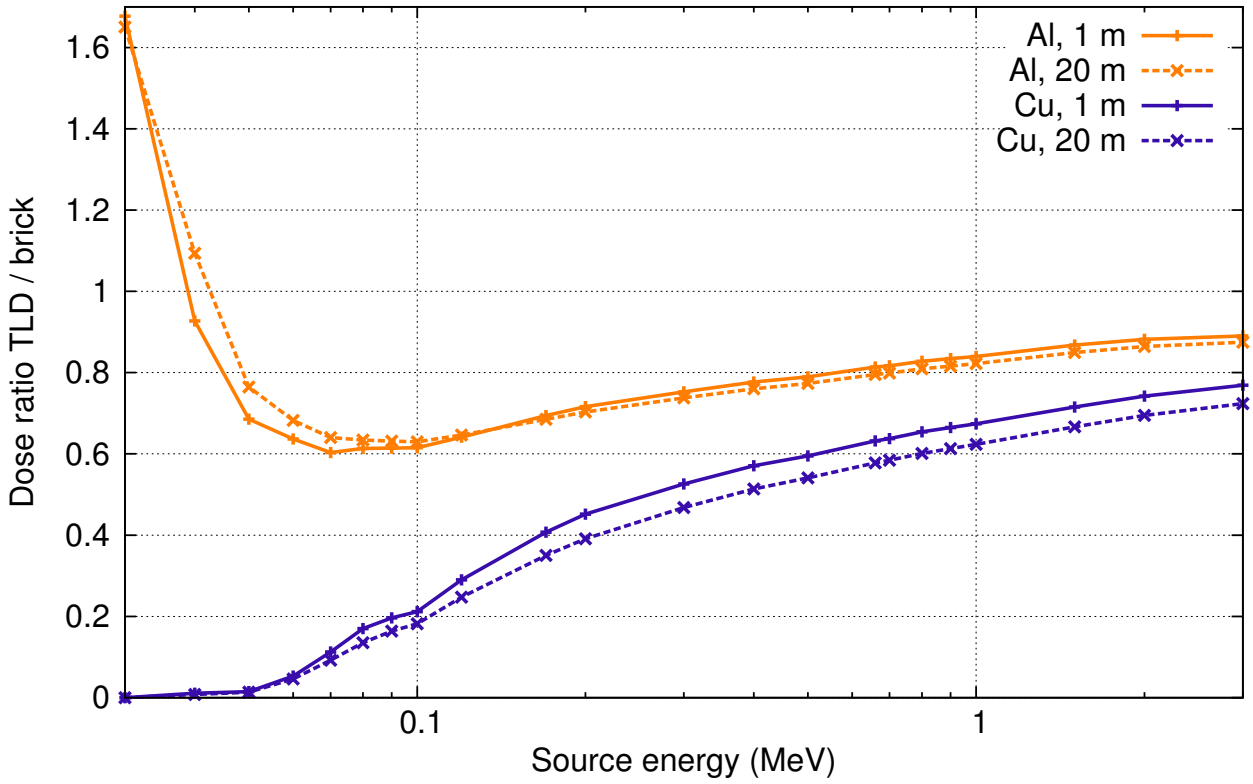

Figure 4.5: Conversion Factor
The conversion factor between a dose in Cu- or Al- covered TLD and a dose in brick due to a source in ground is shown for the altitudes of 1 m and 20 m over ground.

height of the detector, as it can be seen from the plot. The effect of the angular dependence is discussed in the following paragraph.

With this conservative approach of a 20 % error, a conversion factor of CF = 0.82 ± 0.16 was estimated for the following calculations in this work.

4.1.3.4 Angular Dependence

In the case of the church tower in Metlino, the detector is not irradiated at 90° from the front, but under a range angles between approximately 20° and 75°. To evaluate the influence of this change in the irradiation conditions on the dose conversion factor, a sensitivity analysis was carried out, in which the detectors shown in the sections above were simulated to be irradiated under various discrete angles between 0° and 90°.

The angular dependence of the conversion factor was simulated with a source emitting particles at angles of 0°, 15°, 30°, 45°, 60° and 75°. This simulation was carried out for Cu- and Al- shielded

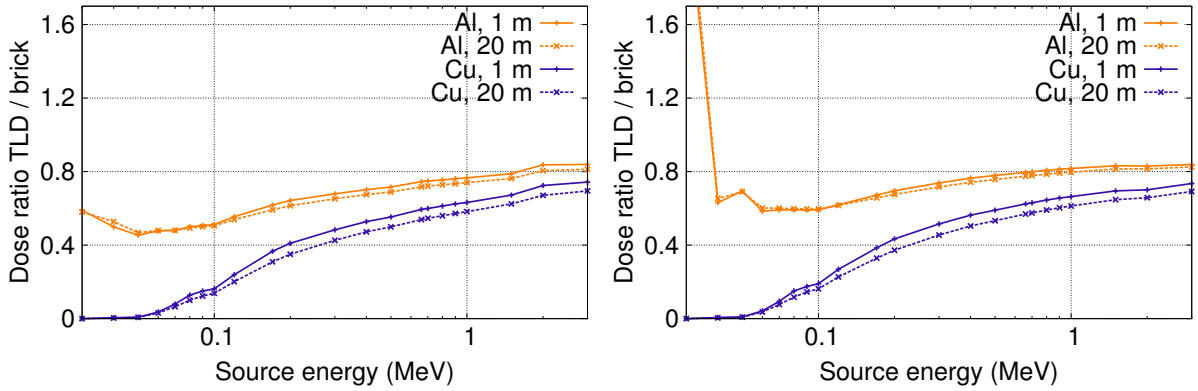

a. Source angle 15°

b. Source angle 45°

Figure 4.6: Angular Dependence
The plots show the conversion factor between a dose in TLD and a dose in brick for a source emitting particles in a direction of 15° and 45°.

TLD as well as for the brick only configuration.

The conversion factors for the calculations with 15° and 45° at an altitude of 1 m and 20 m over ground are shown in figure 4.6.
For 15°, the difference goes below 20 % for energies higher than 0.1 MeV and below 10 % for energies over 0.3 MeV.
For 45° the overall difference is smaller than for 15°. The error is below 10 % for energies over 0.07 MeV and below 5 % in the range of 0.17 MeV to 1.5 MeV.
The difference between angular biased sources and the isotropic source rises for extreme angles ($\leq$15°, $\geq$75°) and gets lower towards 45°.

These calculations show, that the conversion factor is only strongly affected for extreme angles. But for the angles between 20° and 75° that are in question at the church tower, the effect stays below the 20 % error that was initially assumed for the conversion factor.

4.1.3.5 Effects of Plaster and Glue at the Wall

A further uncertainty when measurements are compared with simulations comes from the plaster on the wall. The walls were covered with a variable amount of plaster. On many places of the sampling site, the plaster was completely fallen off, but on other areas of the wall, a thicker layer of plaster was still present. In the simulations presented so far, a bare brick wall was considered.
To account for the variable plaster amount on the wall, a layer of plaster was simulated on top of the brick wall with a variable thickness from 0.5 cm to 5 cm (see Fig. 4.2e).

When the TLD was installed in the brick wall, it was fixed there by filling up the front of the drill hole with glue, (see Tab. A.8). This was also integrated into the simulation and versions with and without glue were compared (see Fig. 4.2f).

Figure 4.7 shows the dose on the Al- shielded TLD for various plaster thicknesses compared to the wall without plaster for altitudes between 0.5 m and 100 m over ground.
The plaster thickness of the brick samples taken was estimated to be about 1.5 – 2 cm. In the sampling heights of 4 – 20 m, the dose is about 70 – 80 % of the dose compared to a wall without plaster.
The presence of glue in the drill hole does not show any difference to simulations without glue.

In the following calculations at the church tower, which was not simulated with a plaster layer, the results will be reduced by a factor of 0.75 $\pm$ 0.05 to account for the absorption by the plaster of a thickness between 1.5 and 2 cm and at altitudes of the samples between 4 and 20 m.

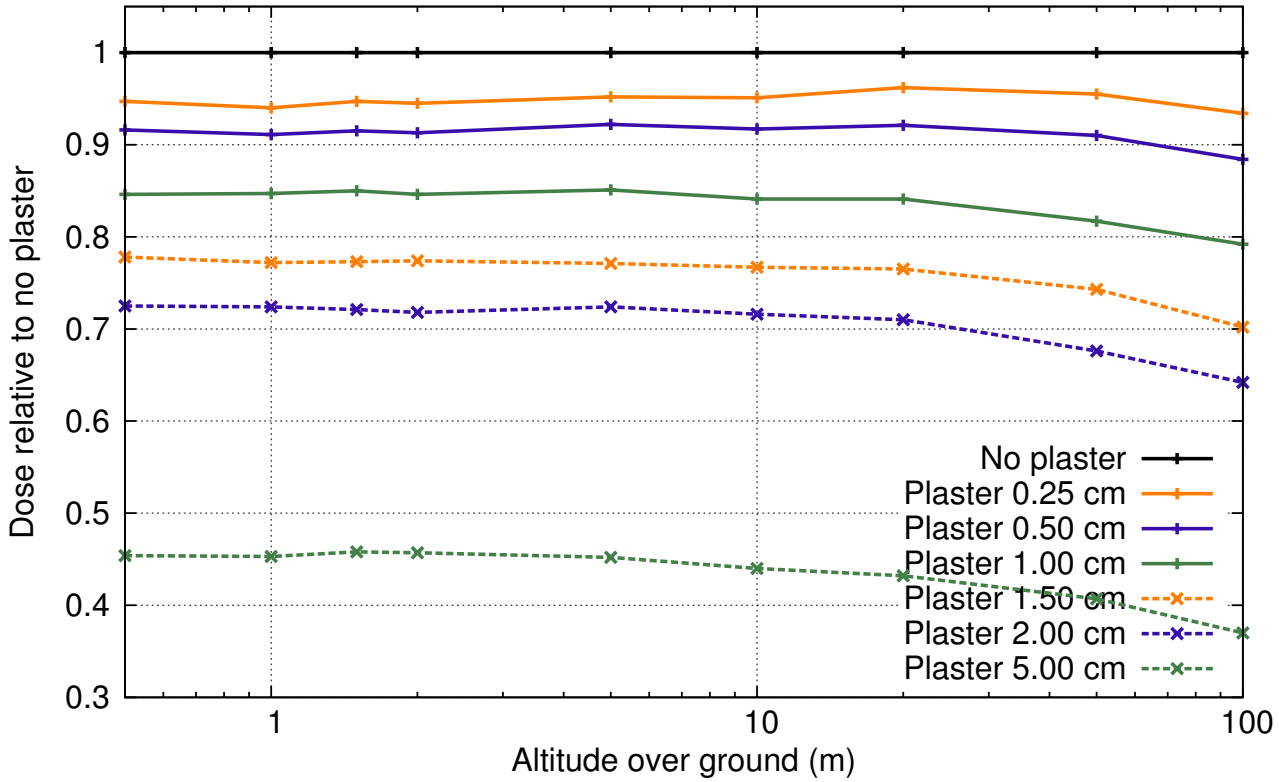

Figure 4.7: Plaster on the Brick Wall
A layer of plaster with a thicknesses between 0.5 cm and 5 cm was simulated. The relative dose compared to a wall without plaster is shown.

4.2 Geometric Dose Profile at a Brick Wall

To investigate the height profiles of brick samples on a wall, some sample calculations were performed before investigating the difficult geometric and source configurations on the church tower in Metlino. Therefore, a brick wall perpendicular to a flat soil surface was simulated (see Fig. 4.8a). The source was simulated in soil in front of the wall and cells for scoring were made at three different heights on the wall.

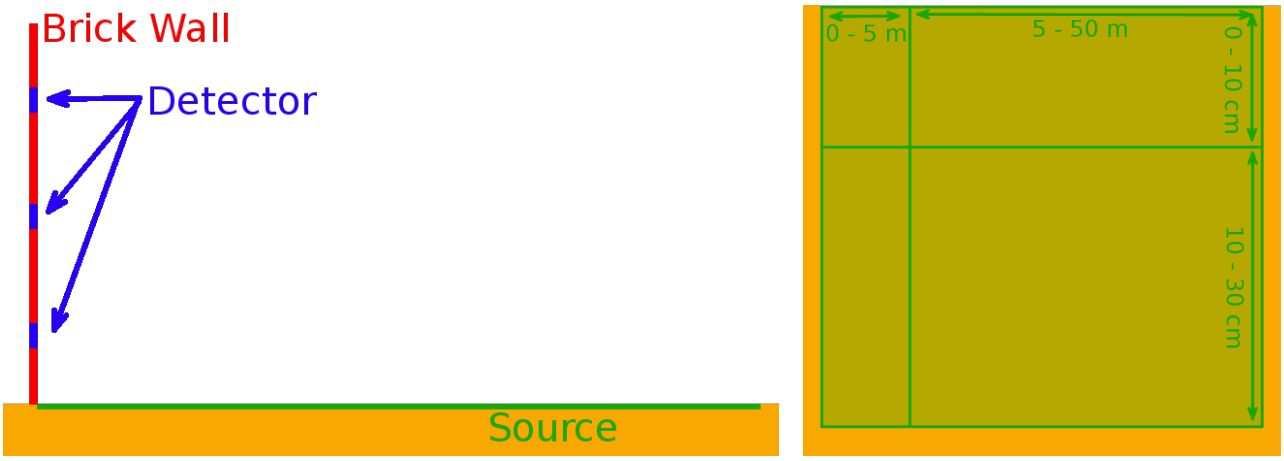

a. Side View **b.** Source

Figure 4.8: Source in Front of Brick Wall
a: A source in front of a brick wall was simulated to investigate the influence of different source distributions on the height profile of the dose in brick at the wall. **b:** The source was segmented into a section at the brick wall and a section further away. The depth was distributed in two layers, up to 10 cm and up to 30 cm. Drawings not to scale.

4.2.1 Setup

The source was simulated in the ground in front of the wall and separated into several sections (see Fig. 4.8b). The source depth was simulated in two sections up to 10 cm in the soil and from 10 cm to 30 cm. The spatial distribution away from the brick wall was sectioned into a part at the wall in a distance of 0 – 5 m and a part from 5 – 50 m.

The height of the detectors in this example corresponds to the heights that were sampled on the church tower : 3.6 m, 11.8 m and 19.6 m (see Tab. 3.1).
Each sampling site consists of a cylindrical disc inserted 0.5 cm deep in the brick wall with a thickness of 1 cm. These were the same detectors as used in the model of the church tower (see section 4.4.1 and Fig. 4.14).

4.2.2 Observations

The height profiles of the dose in the detectors in brick along the wall were studied under various conditions:

- A close source from 0 – 5 m.
- An extended source from 0 – 50 m.
- An extended source with a *dead strip* of 5 m with and a source distance from 5 – 50 m.

All source configurations were simulated with a source depth of 10 cm and 30 cm.

As it can be seen from figure 4.9, the dose decreases with the height of the detector. The further away the source is from the detector, the lower is the decrease with the height of the detector. Also, the deeper the source is, the lower is the decrease with the height. This can especially be seen for sources farther away.

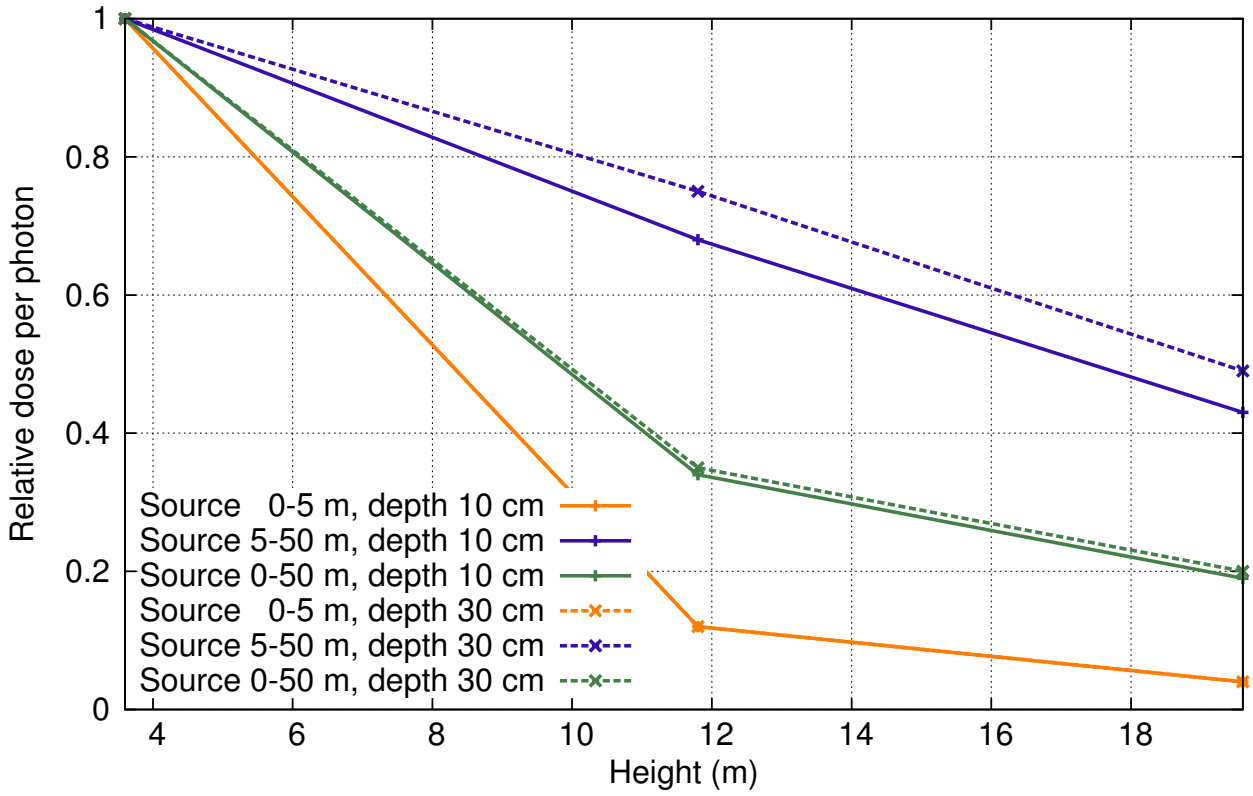

Figure 4.9: Dose Profile at the Brick Wall
The height profile of the dose distribution along the church tower was investigated for different source configurations. The further away from the wall and the deeper the source distribution in the ground, the lower the decrease of the dose with the height. The relative dose per photon is normed on the dose in 3.6 m height.

These effects can be explained by applying the attenuation law and trigonometric calculations. The attenuation law calculates the ratio of the number of particles I after covering a distance x to the initial number of particles I_0 as $\frac{I}{I_0} = e^{-\mu x}$ with μ the linear attenuation coefficient [104].

The ratio between the distance from the closest possible source particle in the close source (distance from the wall 0 m) to the bottom detector and the top detector is $\frac{4}{20} = 0.2$. The ratio of the furthest point in the close source (distance from the wall 5 m) between the bottom and top detector is $\frac{6.4}{20.6} = 0.3$.
This is also the ratio between the top and the bottom detector for the nearest possible source particle in the extended source with the *dead zone*. The ratio for the furthest possible source particle in this source (distance from the wall 50 m) is $\frac{50.1}{53.1} = 0.9$.
This shows, that the contribution of the height of the wall to the total distance between the source and the tally is much higher for the close source than for the extended source. Therefore the attenuation changes stronger with the height for the close than for the extended source.

In this rough estimate, the particles were assumed to leave the source at the surface of the soil. But the source has a depth of 10 cm to 30 cm. Photons emitted from deeper sources, further away reach the detectors under a flatter angle and thus penetrate a longer distance through the thick medium of the soil that absorbs them stronger than air.
For a close source, the effect of the penetration through the thick medium of soil is stronger than the absorption in air. So this strengthens the effect of a decreasing dose with the height.
But for the extended source, the ratio of air travel to travel through soil gets smaller, the larger the source gets, thus creating the opposite effect of a constant, or even increasing dose profile with the height.

It can be concluded, that first the distance a photon travels, and second, the depth of the source has an impact on the dose profile at the brick wall.

4.3 Absorption of a Source under a Water Layer

As it will be seen in section 4.4.2, some sources in the reservoir model for Metlino are covered with water. A series of Monte Carlo calculations was carried out to calculate the attenuation of a water layer on top of a source in soil.

The geometry (see Fig. 4.10a) consists of a soil layer (yellow) with a layer of water on top (dark blue), on top of the water is a layer of air (light blue). The thickness of the water layer was gradually raised between 1 cm and 1000 cm.

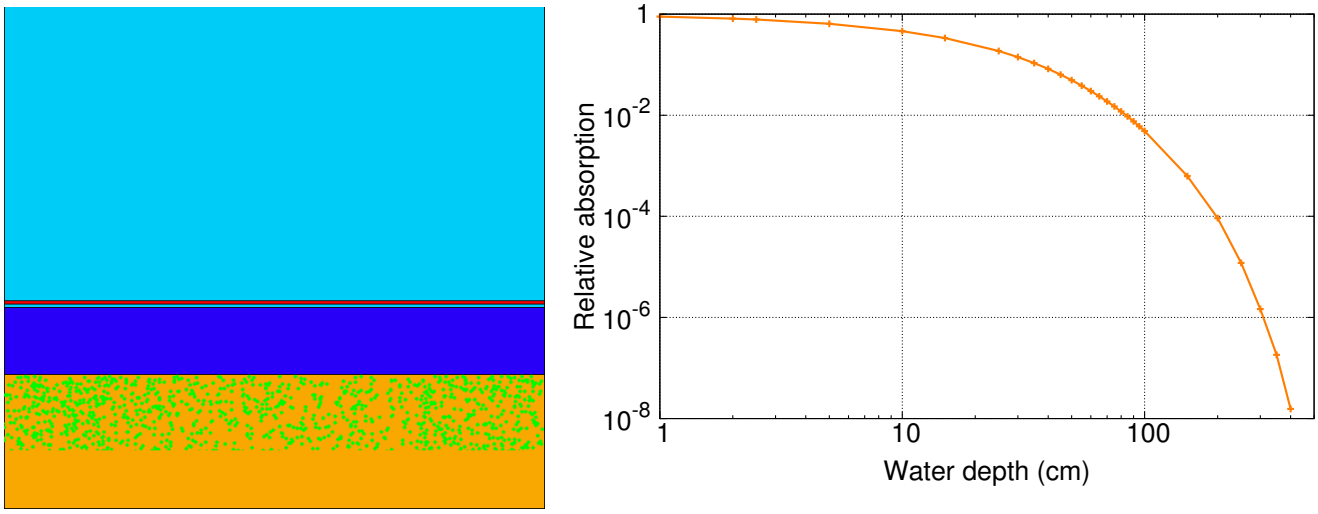

a. Geometry and source

b. Absorption

Figure 4.10: Calculated Absorption of a Water Layer
a: A layer of soil (yellow) with a layer of water (dark blue) and a layer of air (light blue) on top of each other. The radionuclide source is distributed in the ground (green). The particles crossing a surface 1 cm above the water (red) are counted. **b:** Relative absorption of a water layer above a source compared to the absence of a water layer.

The source was distributed 30 cm in the ground and emitted photons in the range from 0.01 – 3.00 MeV (green dots).

The simulations show a constant drop in the number of particles crossing the surface of the water layer. As it can be seen from figure 4.10b, with a water layer of 50 cm, only 5 % of the particles hit the detector compared to simulations with no water layer. With 100 cm of water, less than 0.5 % of the initial particles cross the surface. Sources covered by more than 100 cm of water can be neglected for the problems presented here.

4.4 Simulation of the Metlino Area

Two of the remaining buildings in Metlino, the church tower and the granary serve as data reservoirs for the research performed here. As it can be seen from the map in figure 3.1, the two buildings face in different directions, covering different sections of the area of Metlino. The remaining North-West wall of the granary faces towards the Metlinski pond and can give information about the contamination in this area. The church tower however faces the area where nowadays the reservoir lake R10 is and where the Techa river was flowing before the evacuation of Metlino.
Figure 4.11 shows the area of Metlino before and after the evacuation. The terrain in front of the granary stayed quite unchanged, the dam was raised and the shore became swampier. The changes

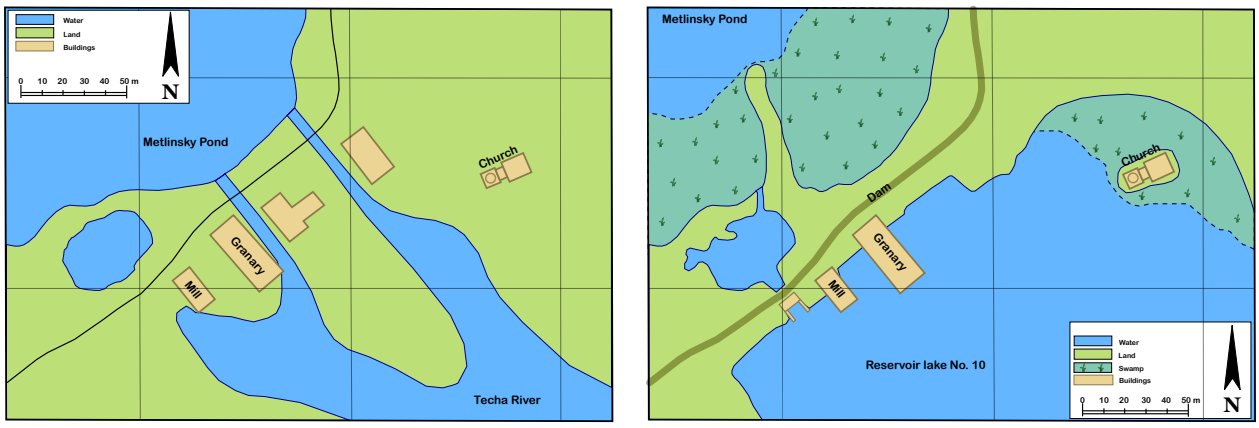

a. Before evacuation **b.** After evacuation

Figure 4.11: Metlino Before and After Evacuation
Before the evacuation of Metlino, the Techa river crossed the village South-East of the Metlinski pond. After the evacuation in 1956, the reservoir lake covered most of the land South of the dam up to the church tower.

at the church tower region are more drastic. Before the evacuation, the church tower was on dry land and the Techa river was about 30 m away. The reservoir lake created after the evacuation now covers the whole area up to the church tower. The church tower is now on a small platform at the shore of the lake. The area to the North and East of the church tower is marsh land, that is flooded from time to time by water from the reservoir lake.

The following sections first describe the model for the church tower and focus on the creation of models for the geometry of the area before the evacuation of Metlino, called *Metlino model* and after the evacuation and creation of the reservoir lake, called *reservoir model*. These models were used for radiation transport calculations to determine the conversion coefficients between the dose in brick and the integral air kerma at shoreline.

4.4.1 The Church Tower

The geometry of the church tower was modeled according to the measurements taken in the field trips (see section 3.3). Figure 4.12 shows different views and intersections of the church tower. The brick in the walls was simulated according to Taranenko et al. [99] (see Tab. A.3).

The sampling positions at the church tower (see Fig. 3.4 and Tab. 3.1) were integrated into the MCNP model. Their location in the model can be seen in figure 4.13 that shows intersection of the church tower model at heights of 3.6 m, 11.8 m and 19.6 m.

Several different sampling cells were integrated at each sampling position. Therefore a cylinder

with radius 18 cm, perpendicular to the wall was divided into ten subsequent sections of 1 cm width from 0.5 cm to 10.5 cm into the wall (see Fig. 4.14).
The section of 0.5 – 1.5 cm into the brick corresponds to the first section of the analyzed brick sample, while the deeper sections correspond to deeper layers in brick that were analyzed for selected samples (see section 2.5.1 and Tab. 3.2).
The section of 0.5 – 1.5 cm into the air was also sampled. This enabled the comparison of the dose in brick to the dose in air at the sampling location. These measurements were compared to the dose rate measured with the hand held dose rate meter at the sampling site.

To compare the simulation for brick with the TLD measurements, the conversion factors shown in section 4.1 were used.

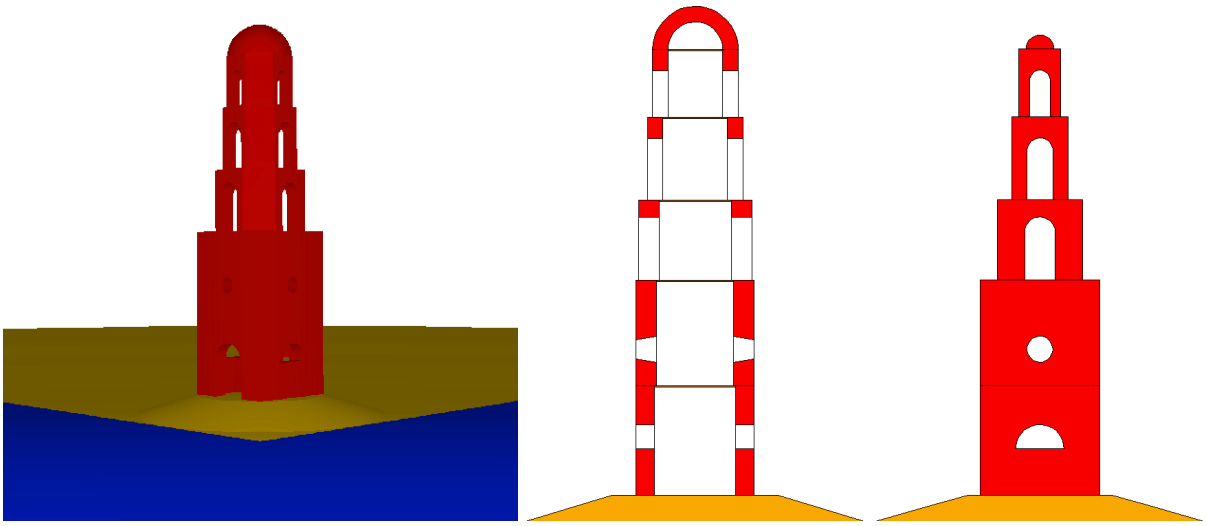

Figure 4.12: Church Tower Model
The figures shows a rendered 3D plot of the church tower model and two intersections of the church tower. The church tower was surrounded by water on two sides and was slightly over the water level.

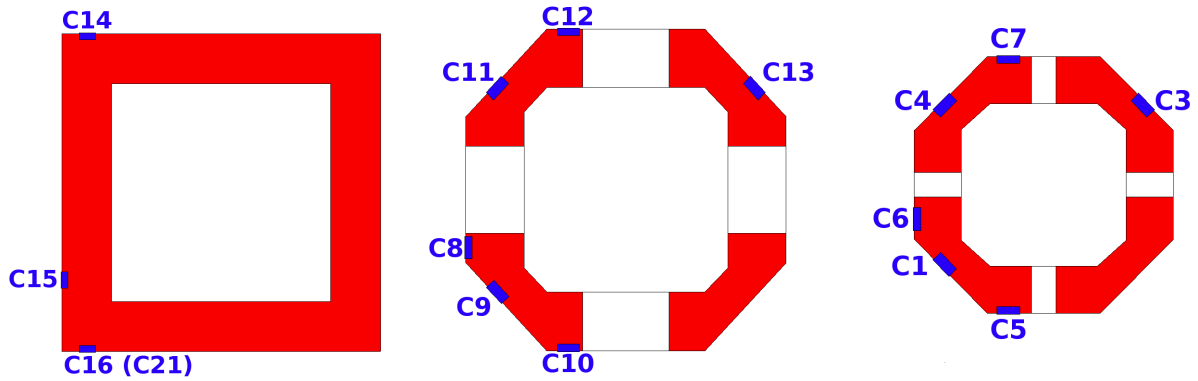

a. Ground floor **b.** 2nd floor **c.** 4th floor

Figure 4.13: Brick Sample Locations
Locations of detectors in brick in the model of the church tower at heights of 3.6 m, 11.8 m and 19.6 m. Sample C21 is below C16 at 1.3 m.

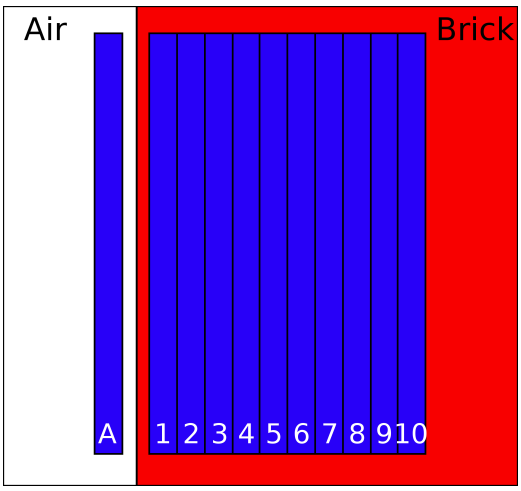

Figure 4.14: Simulated Sampling Site
Simulation of a brick sampling site. One layer of air and ten layers of brick were sampled.

4.4.2 The Reservoir model

The surrounding of the church tower was reconstructed using aerial views of the site (see Fig. 4.15) and measurements taken during the field trips (see chapter 3.1). The distances in the grid used for the dose rate mapping were used to model the surrounding of the church tower.

The present-day source configuration for the area around the church tower was determined from measurements performed in the field trips. The church tower is surrounded by water on its West and South side. To the North and to a short band at the South, there is swampy ground. East of the church tower is the church.
The areas to the North and South were mapped with dose rate measurements in the 2012 and 2013 field trips (see section 3.1). The mapped area was divided into sectors with similar ranges of dose rates (see Fig. 4.16). A part of the source to the South of the church tower is below the water level. The absorption coefficients shown in section 4.3 were used to relate the dose rates from areas covered with water to the uncovered areas. The source distribution in the model is shown in figure 4.17.

The depth of the source was estimated to 30 cm. The depth distribution of the activity was also measured with in situ gamma spectroscopy (see section 3.5). It was shown that 98 % of the activity is distributed in the first 30 cm of the soil.
The calculations shown in section 4.4.4 fortify this assumption, showing that the relative source activity in soil deeper than 30 cm is below 10 % of the total source activity 60 years after the contamination (see Fig. 4.22b). This also motivated simulating the depth distribution of the source up to 30 cm.

Figure 4.15: Reservoir Lake

The areal image shows the reservoir lake in 2010. To its North is the Metlinski pond, the dam and the remaining walls of the mill and the granary. To its East is the church and the church tower. In the South is the reservoir lake R10. © 2014 DigitalGlobe. © 2014 Google.

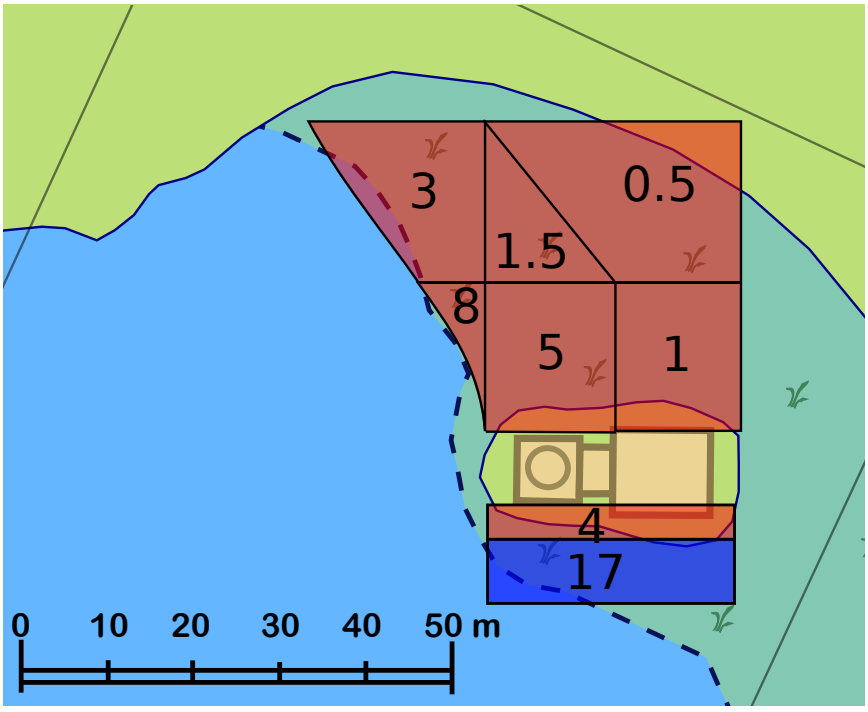

Figure 4.16: Source Distribution

The sketch shows the source distribution around the church tower in the reservoir model. The area to the North and the South of the church tower was mapped with dose rate measurements and was then sectioned into areas with similar dose rate. Numbers give the dose rate in $\mu Gy\,h^{-1}$.

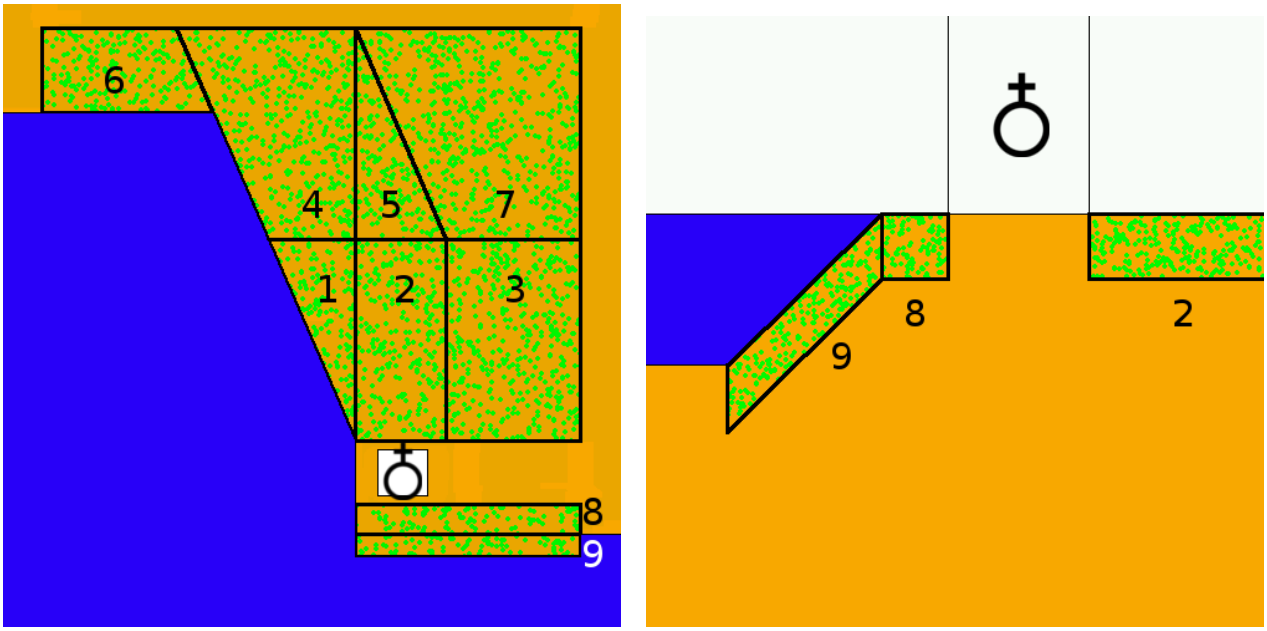

a. Top view **b.** Side view

Figure 4.17: Source Distribution in the Reservoir Model
The source in the reservoir model from a top view **(a)** and a side view **(b)**. The water is in blue, soil in yellow and the source areas are indicated with green dots. The number of the source is indicated. Drawings not to scale.

In the reservoir model, flat discs of 1 cm thickness and diameters in the range of several meters were implemented as detectors in air. They were used to estimate the present day dose rate in air for the areas where the dose rate was measured with the Automess dose rate meter (see section 3.1).

4.4.3 The Metlino Model

The reconstruction of the historic geometry in Metlino required extensive research. Only a very limited amount of sources give detailed information about the area before the evacuation or about the evacuation process. A description on the chronology of the changes in the Metlino area is described in Vorobiova et al. [112].
In a paper of Mokrov et al. [74], some sketches of the dam and a map of the area are shown. That map is one of the main sources of the geometry reconstruction (see Fig. 4.18). The other main source to reconstruct the area was based on the measurements of four transects across the reservoir lake, performed during the 2012 field trip (see section 3.4). These transects enabled the reconstruction of the height profile of the bottom of the reservoir lake, as the ground of the reservoir lake is the surface of the former floodplain and the Techa river arms. Figure 4.18 shows the transects laid over the map of the village.

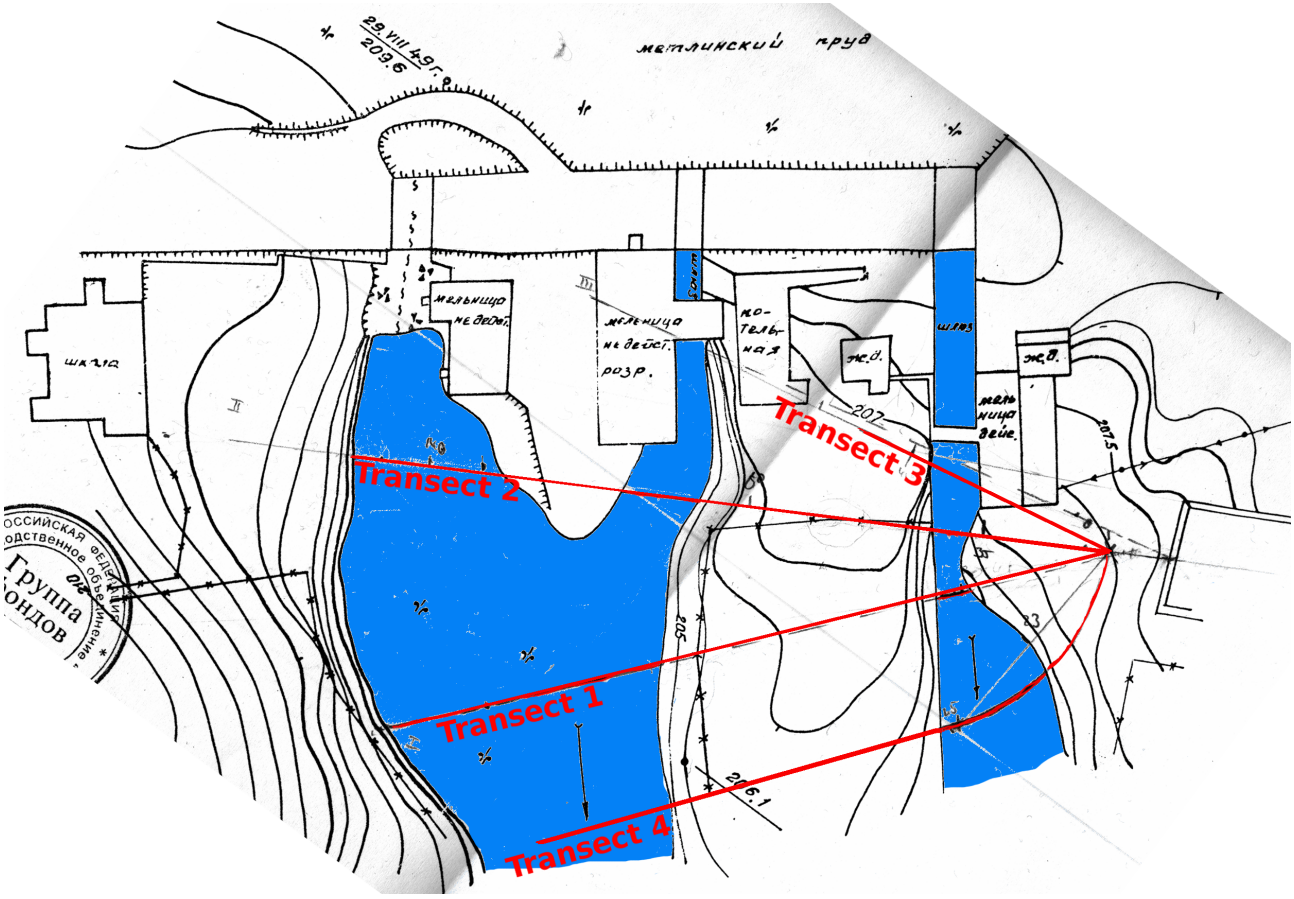

Figure 4.18: Historic Map

The map shows the mill and granary complex in the village of Metlino and the course of the Techa river to the South of the dam. The dam is shown on the top, the two arms of the Techa river are channeled from the Metlinski pond in the very top through the dam. They flow into each other after a few hundred meters (below the end of the map). The transects that were measured across the reservoir lake are indicated as red lines. Map after Mokrov et al. [74].

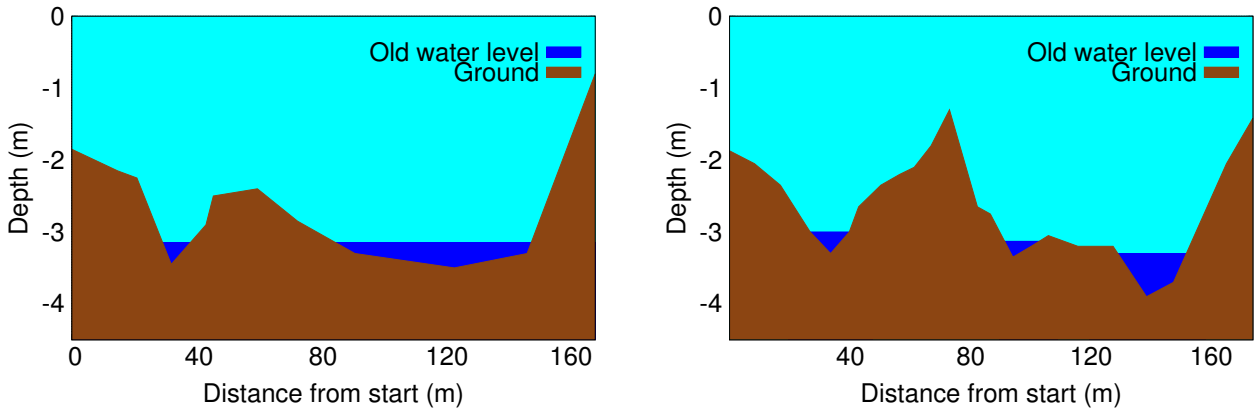

a. Transect 1

b. Transect 2

Figure 4.19: Landscape Elevation

The landscape elevation along the transects 1 and 2 across the Reservoir Lake shows the position and depth of the Techa river.

From the depth measurements along the transects shown in Fig. 3.8, the position and depth of the arms of the Techa river was determined. Figure 4.19 shows the reconstructed elevation profile along the ground and the position of the arms of the Techa river. The Techa river is not very deep, between 30 – 80 cm.

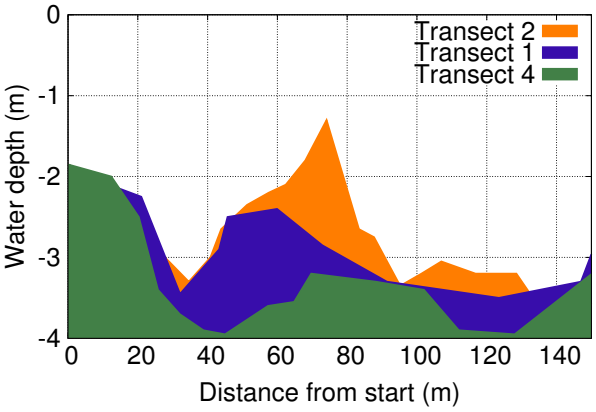

Figure 4.20: Elevation of Peninsula
The graph shows the elevation of the peninsula between the two arms of the Techa river. The further away from the dam, the lower the elevation of the peninsula. Distance from dam at peninsula: Transect 2: 50 m, transect 1: 69 m, transect 3: 96 m (see also Fig. 3.8).

The source distribution of the Metlino geometry was analyzed using the map and transects shown in figures 4.18 and 4.19. The source areas were identified by analyzing possible floodplains in the map. The positions of the sources in the model are shown with green dots in figure 4.21a. The sources cover the area between the two arms of the Techa river and to the East of the right arm of the river. The height profile of the three transects across the reservoir lake indicate that the peninsula between the two arms gets lower as it gets farther away from the dam (see Fig. 4.20). Transect 2 is at a distance of about 50 m from the dam, transect 1 at a distance of about 69 m and transect 4 at a distance of 96 m. The elevation is 1.9 m higher at transect 2 and 0.8 m higher at transect 1 than at transect 4. This is also supported by the fact that there are buildings shown in the area of the peninsula nearest to the dam in the map (see Fig. 4.18), it seems very unlikely that these buildings were flooded frequently.

This assumption is also supported by the activity measurements along these transects. While the activity profile for the transect 2 near to the dam shows a clear drop in the activity for the location of the peninsula (see Fig. 3.8d), there is a constant activity in transect 4 over the area of the peninsula (see Fig. 3.8h). Transect 1 also shows one measurement with a drop in the activity, but this is the only measurement on this transect and a single measurement is not really trustworthy. Transect 4 in contrast shows four measurements with a reduced activity. This shows that the peninsula was weaker contaminated towards the dam. Only when the elevation of the peninsula gets lower (transect 4), the peninsula gets contaminated again. It was assumed that the peninsula was uncontaminated up to height line of 207 m.

The Eastern floodplain is limited by an elevation of the terrain.

The reservoir model was altered compared to the setup shown in the previous sections due to findings presented in section 5.1. The locations of the sources in this reservoir model were compared to the locations of the sources in the Metlino model. Figure 4.21b shows an overlay of the sources

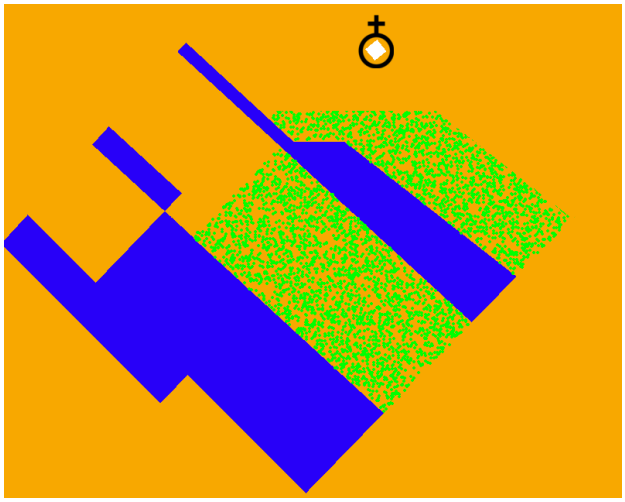

a. Sources in the Metlino model.

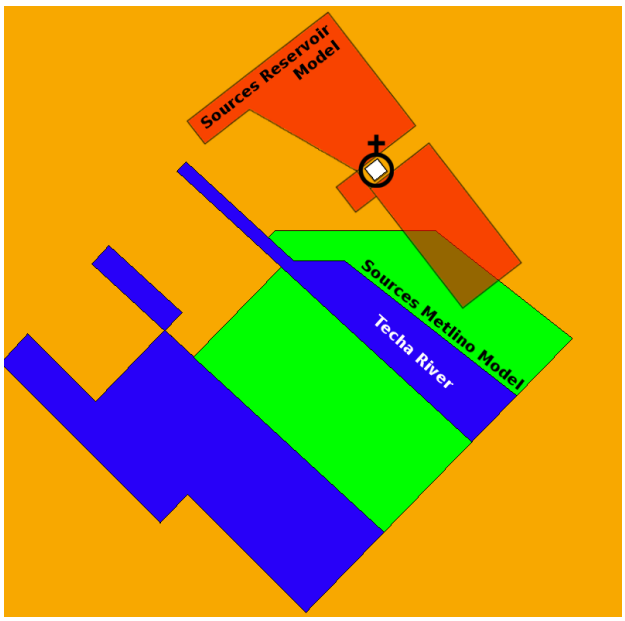

b. Metlino model and reservoir model compared.

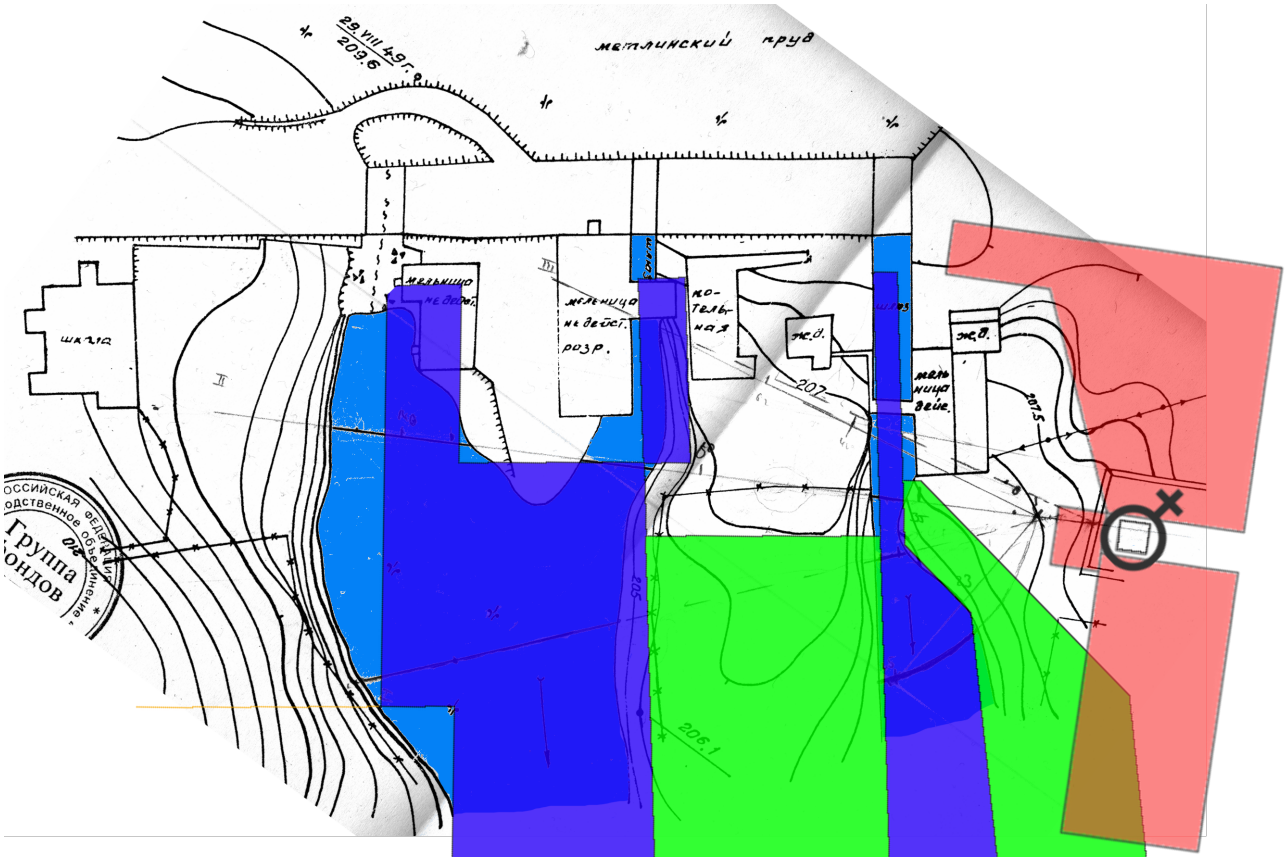

c. Overlay of sources and map.

Figure 4.21: Sources Compared

The distribution of the sources in the reservoir and the Metlino model are compared. **a:** Sources in the Metlino model. **b:** Overlay of sources in the Metlino and the reservoir model. **c:** Both sources marked on the historic map. Color scheme: Green: Sources in the Metlino model, red: Sources in the reservoir model, blue: Techa river, yellow: Soil.

in this final reservoir model with the historic contamination of the Metlino model. Figure 4.21c shows the locations of these sources on the historic map. These images illustrate the following:

- The ground level sources in the reservoir model are not overlapping the sources in the Metlino model.
- The under water level sources in the reservoir model overlap slightly the sources in the Metlino model. This seems plausible as the under-water sources are at the former surface level of Metlino which is identical to the ground of the lake nowadays, and thus was a part of the historic floodplain.
- The sources for the historic contamination stretch as far as the contour line for the houses but not farther.
- The location of the Techa river and the church are congruent with their respective position on the historic map and on the source plots created with MCNP. This indicates that the simulated geometry comes close to the actual geometry.

Different source configurations for the Metlino model are discussed in section 6.2.3.

The contamination in Metlino lasted for 7 years, between 1949 and 1956. Taranenko et al. [99] suggest a minimal source depth of 2 cm, a maximal source depth of 10 cm and an average source depth of 5 cm for this contamination.
This is also supported by the calculations in section 4.4.4 that suggests an activity distribution in soil with only 10 % of the initial activity having migrated into regions deeper than 5 cm for a time period of 10 years (see Fig. 4.22a). Only a minimal fraction of the initial activity is distributed deeper than 10 cm.
In this work, a standard source depth of 5 cm was assumed for the Metlino model. The cases of 2 cm and 10 cm source depth were calculated as lower and upper limits and are discussed in section 6.2.1.

The main source of contamination in Metlino is the long lived radionuclide ^{137}Cs. At the time of liquid radioactive waste discharge, also elements with a shorter half-life played an important role: e.g. ^{95}Zr, ^{95}Nb, ^{103}Ru and ^{140}Ba [71].
These isotopes have their main gamma energies in the range of 0.50 – 0.77 MeV. Simulations with energies between 0.50 – 0.77 MeV were performed on the Metlino model, and a spectrum comparable to that of ^{137}Cs as well as a comparable dose per photon in the detectors was calculated.
This shows, that the 0.66 MeV energy of ^{137}Cs can act as a substitute for the energies of the other isotopes, and that it is sufficient to consider ^{137}Cs in the calculations here.

For the estimation of the air kerma in the Metlino model, detectors in air at 1 m above ground were integrated into the model. Some of them were discs with a thickness of 1 cm over a larger area of ground, some of them were small tubes following the shoreline of the Techa river with a quadratic cross section of 15 $\times$ 15 cm.

4.4.4 Migration of the Radionuclide ^{137}Cs in Soil

To estimate the depth distribution of the sources, the migration of nuclides in soil was calculated using a formula by Minenko et al. [68]:

$$A(z,t) = A(0,0)\exp\left\{-\frac{z}{\beta(t)}\right\} \tag{4.8}$$

It is A(z,t) the activity concentration at depth z and time t, with A(0,0) the initial activity concentration at depth 0 and time 0. $\beta(t) = \beta(0) + vt$ describes the exponential distribution of the activity with the depth, with v the average downward migration rate .
Units: [z] = g cm^{-2}, [v] = g cm^{-2} a^{-1}, [β(t)] = g cm^{-2}.

The depth distribution in the range of a few months up to 60 years was calculated (see Fig. 4.22). After 10 years, there is only about 10 % of the initial activity in depths $\geq$ 5 cm; after 60 years there is less than 10 % activity in depth $\geq$ 30 cm.

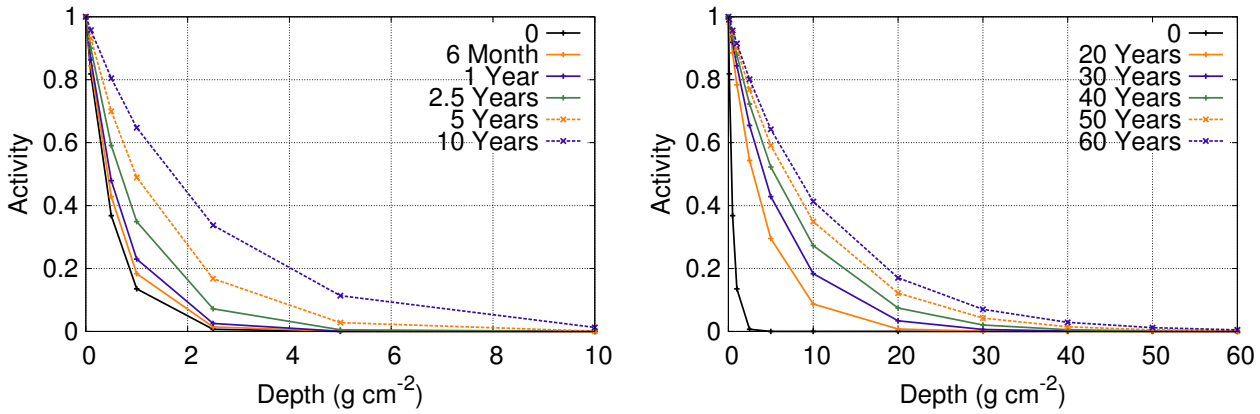

a. 0 – 10 years

b. 0 – 60 years

Figure 4.22: Migration in Soil
The plots show the migration of the ^{137}Cs activity concentration with the time. The activity distribution is plotted relative to A(0,0). About 10 % of the initial activity is in depth $\geq$ 5 cm depth after 10 years **(a)** and less than 10 % in depth $\geq$ 30 cm after 60 years **(b)**.

Chapter 5

Results – Determination of Air Kerma at Shoreline

5.1 Estimation of the Anthropogenic Dose from 1949 – 1956 in Brick

The principle of evaluating the air kerma above shoreline is shown in figure 5.1. First, the reservoir model and the TLD measurements are used to determine the dose accumulated in bricks during one year (2012). Then, with a model for the temporal development of the dose rate through the storage period, the brick dose between 1956 and 2012 can be calculated. The Metlino model is then used to determine a brick-to-air conversion factor matrix that allows to determine the integral air kerma at shoreline between 1949 and 1956.

5.1.1 Reservoir Model

To calculate the reservoir dose, the first approach was to determine the source strength by fitting it to the dose rate per unit source strength in air. For this task, the dose in air at 1 m above ground was simulated using a detector in air over each source cell (see section 4.4.2) and then it was compared with the dose rate measurements in air (see section 3.1). With these results, the source strength of each source cell and the total source strength was estimated.
It turned out, that the results of this approach were mathematically unstable. There was a strong variability in the results of the dose rate measurements so that slight variations lead to strongly different results. A different, mathematically more stable approach was used to overcome these issues.

In the second approach, the dose rate measurements were used to weight the source cells, based on the average of all dose rate measurements within one cell area (see Fig. 4.16).

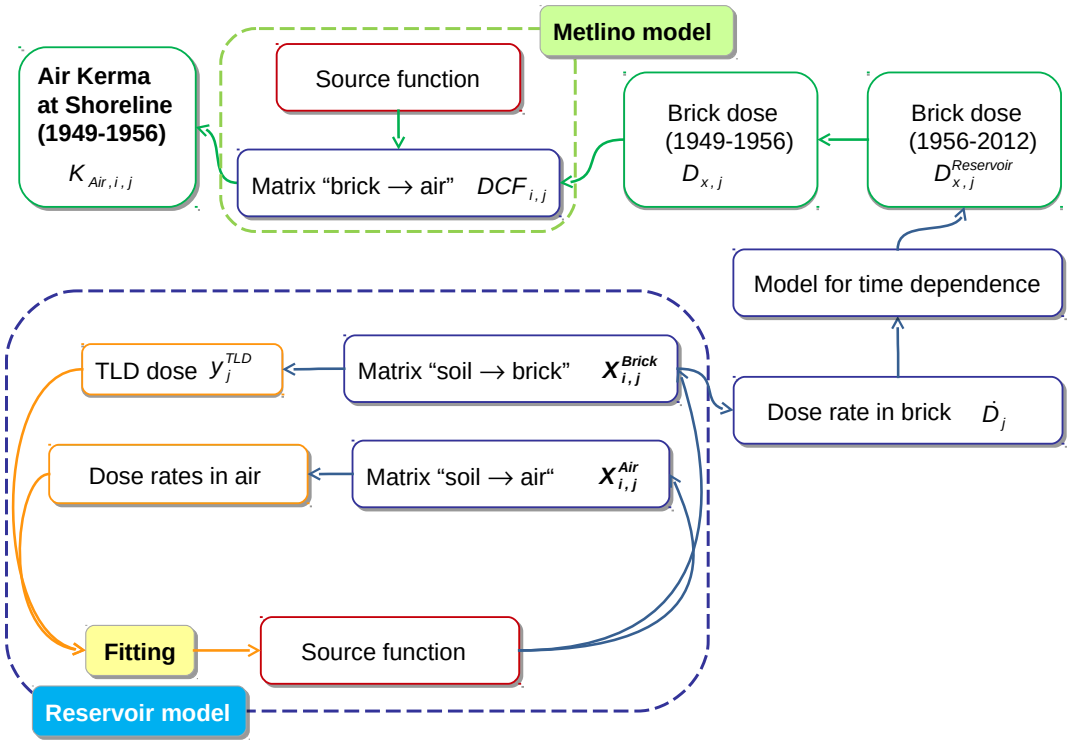

Figure 5.1: Determination of the Integral Air Kerma

For the determination of air kerma, first the reservoir dose was calculated. With a model for the effective half-life of the radionuclide ^{137}Cs, the dose in brick from 1949 – 1956 was estimated. With this, the integral air kerma at shoreline was reconstructed.

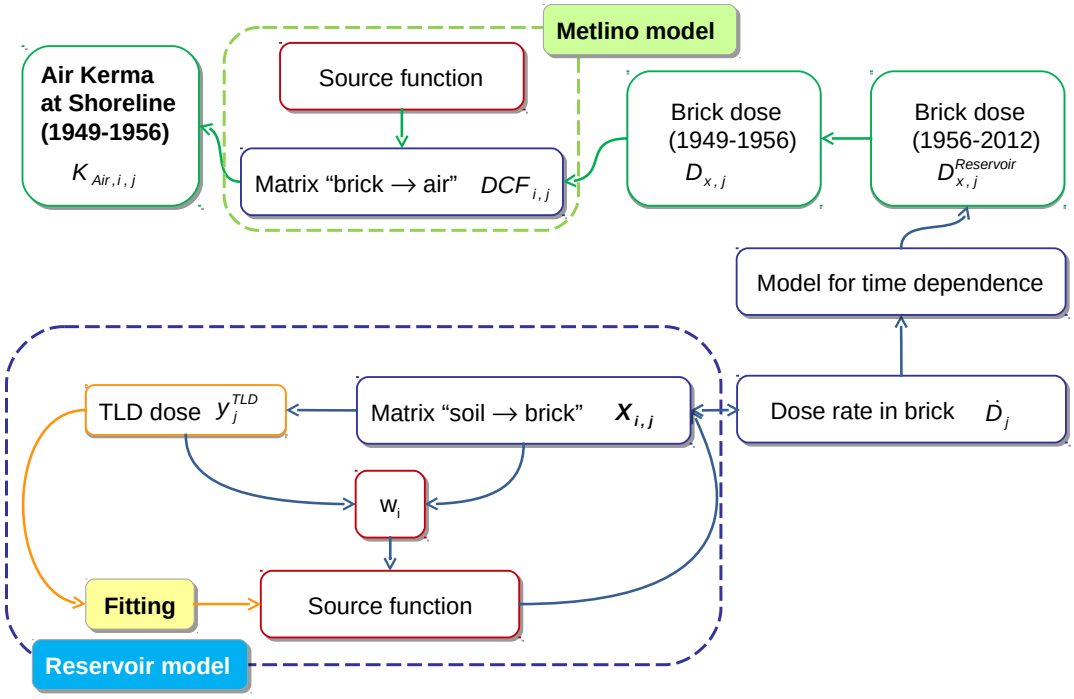

Figure 5.2: Determination of the Integral Air Kerma using Source Weights

In the reservoir model, the annual dose in brick is fitted using the matrix soil-to-brick, and by weighting the sources S_i with the factors w_i.

With this approach, the results became mathematically stable.
In the new calculation scheme, only the matrix soil-to-brick, modified by the weight of the source cells w_i, was used to fit the source function, not two matrices soil-to-brick and soil-to-air (see Fig. 5.2).

With the measured annual dose at the jth TLD, $\boldsymbol{y}_j^{TLD}$ and with the simulated annual dose per photon, $\boldsymbol{X}_j^{TLD}$ the activity was calculated as the linear fit between $\boldsymbol{y}_j^{TLD}$ and $\boldsymbol{X}_j^{TLD}$:

$$\boldsymbol{X}_j^{TLD} \cdot A = \boldsymbol{y}_j^{TLD}$$

The activity A_i of the different source cells S_i was calculated as $A = \sum_i \frac{w_i}{W} \cdot A_i$, the sum of weights of the source cells calculates as $W = \sum_i w_i$.

Figure 5.3 shows the measured annual dose in TLD and the calculated annual dose along the three height profiles of the church tower (see Fig. 3.4). Error bars indicate an error of one standard deviation.

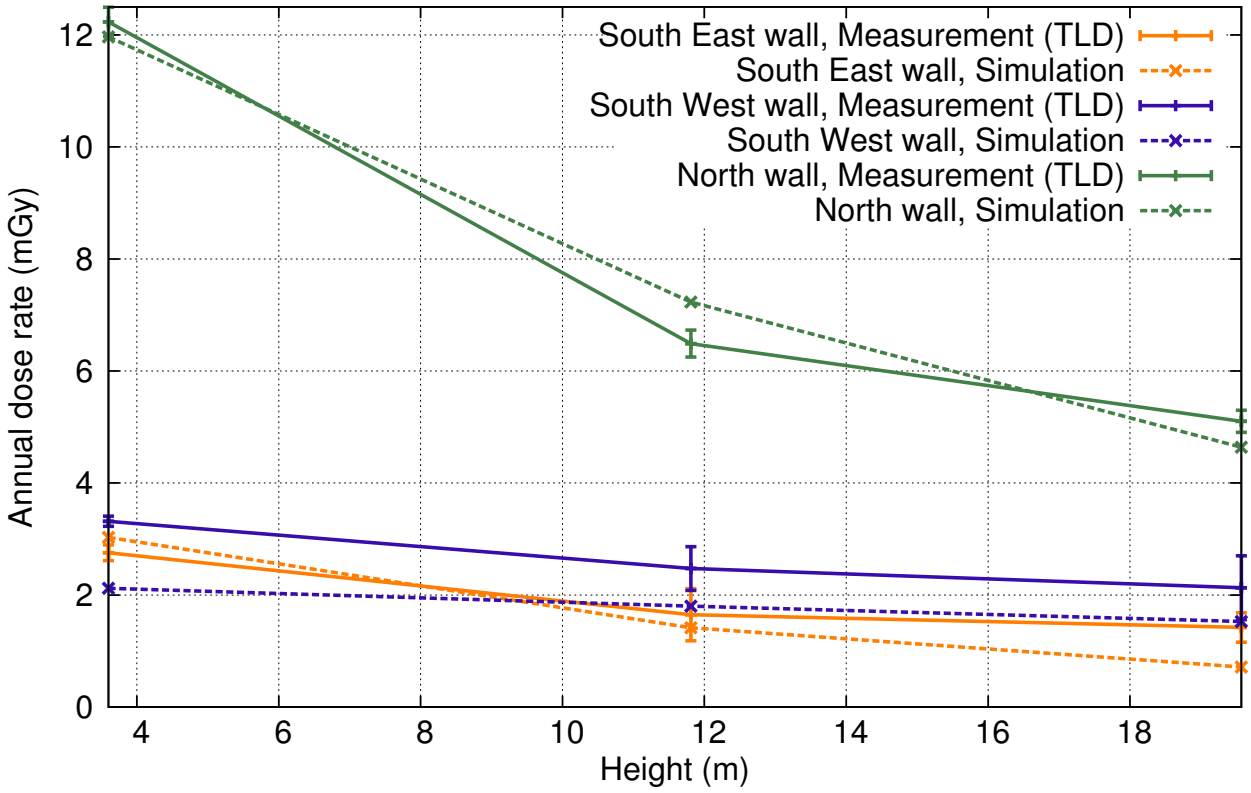

Figure 5.3: Height Profile
The height profiles along the church tower show that the calculated annual doses match the TLD measurements for the Northern profile, but that there is a discrepancy for the South-Western and South-Eastern profile.

The calculation based on the source distribution in the reservoir model (see Fig. 4.17) yields optimized simulated annual dose values in agreement with the TLD derived values for the height profile of the North-Western wall. The profiles on the South-Eastern and South-Western walls, facing the Techa river, do not match.

Calculated doses for the South-Western wall are continuously lower than the measured ones. The only source for these detector positions are the contaminated areas to the other side of the church tower, the North-West and the North. However, these sources are mainly determined by the detector positions in the North-Western walls, with the dose per photon being 1 – 2 orders of magnitude larger than for the corresponding detectors in the South-Western wall. With the optimized source strengths generally reproducing the measured annual doses for the North-Western wall, the same level of contamination obviously falls short of explaining the measured doses in the South-Western wall. This is a strong indication, that there must be additional sources to the South of the church tower, which had not been considered so far.

For the detector positions in the South-Eastern wall, the assumed source geometry produces a height profile, which shows a stronger dose increase with height than actually measured. According to the model calculations in section 4.2 this implies that the source has to have a greater extension to the South as it was assumed.
The problem with the sources on the South-Eastern and South-Western wall of the model was that the church tower is surrounded by water at these sides and thus was not accessible for dose rate measurements in this area. Consequently no sources were simulated on the West of the church and no more sources on the South than actually measured. But obviously, the contamination must not stop at these areas, but can extend along the bottom of the lake.
So in the next step, additional sources under water at both sides of the church tower were installed. (see Fig. 5.4).

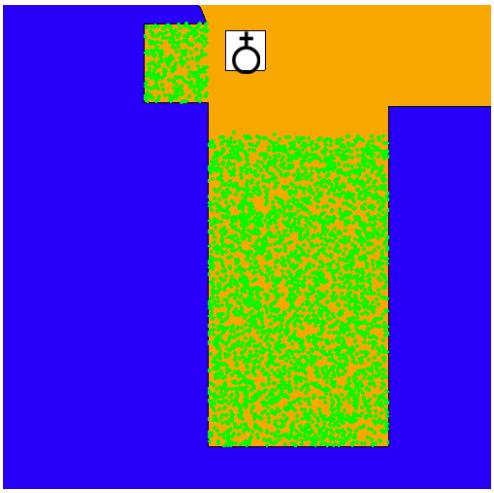

Figure 5.4: Additional Souces
Additional sources were installed at the Southern and Western side of the church tower. Green dots indicate the source areas.

With the updated source configuration, the calculated height profiles agree with the measurements also for the profiles facing the Techa river (see Fig. 5.5). The profile facing away from the Techa river to the area nowadays contaminated (shown in green) shows a steeper profile than the two profiles facing to the former Techa river (shown in blue and orange).

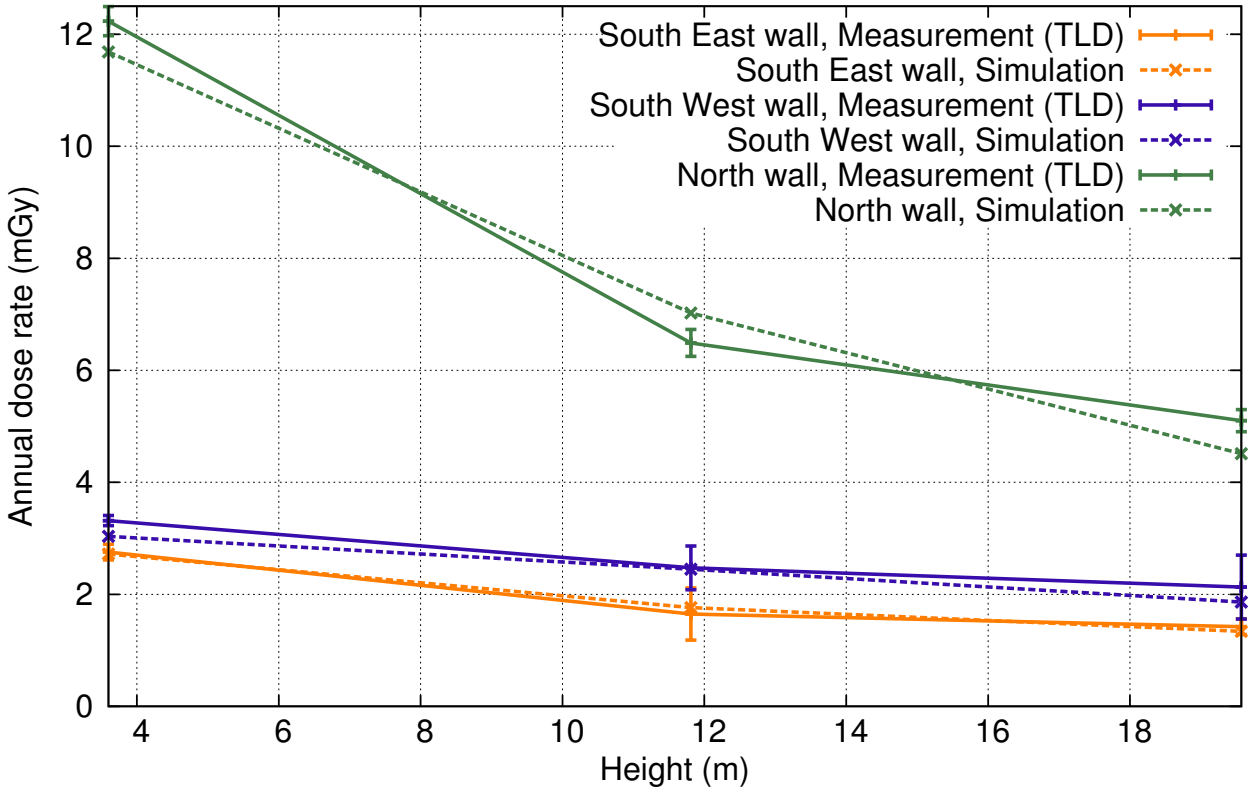

Figure 5.5: Height Profile using Updated Source Configuration
With the updated source configurations, the simulated annual doses at the church tower follow the measurements also on the profiles facing towards the former bed of the Techa river.

The source was segmented into 11 areas, nine of them had dose rate reference measurements and a source weight w_i associated with them (see Fig. 5.6). There were a total of 16 brick sample positions, 10 of them had measured TLD samples.

The result of the calculation by MCNP is the dose per photon from source sector i, $i = [1 \ldots 11]$ in TLD j, $j = [1 \ldots 10]$, resulting in the matrix $\boldsymbol{X}_{i,j}$. For sources 1 – 9, a corresponding source weight w_i was determined by taking the average of all measured dose rates in the source area. The dose rates from the areas and the appropriate weight is shown in table 5.1.
The contribution from the first 9 sources to each detector was added up, weighting the contribution of each source by w_i, resulting in a vector $\boldsymbol{x}_{1-9,j}$ with the combined contribution of the first nine sources to each detector:

$$\sum_{i=1}^{9} (\boldsymbol{X}_{ij} \cdot w_i) = \boldsymbol{x}_{1-9,j} \tag{5.1}$$

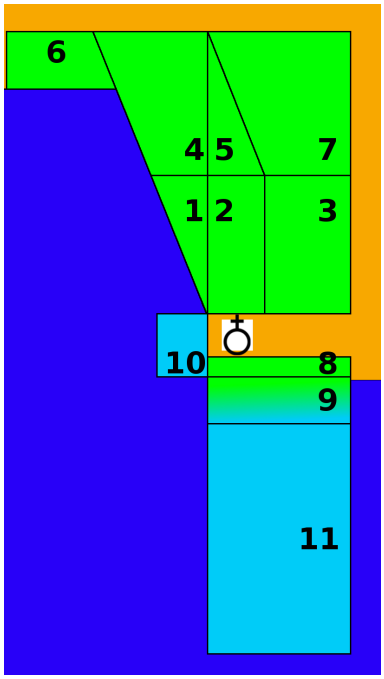

Figure 5.6: Source Numbers
The source numbers 1 – 9 are above the water, source 9 is partly under the water, sources 10 and 11 are completely under the water.

Source	Average dose rate ($\mu Gy\,h^{-1}$)
1	7.74
2	4.59
3	1.25
4	3.17
5	1.37
6	0.46
7	3.24
8	3.93
9	16.94

Table 5.1: Measured Dose Rates in Air over the Source Areas
The dose rate in air at 1 m over the source cells is averaged after subtracting the background dose (doses in $\mu Gy\,h^{-1}$). The average dose rate is used to weight the sources.

In the next step, the weighted results on each detector from the first nine sources $x_{1-9,j}$ and the contribution to sources ten and eleven $x_{10,j}$ and $x_{11,j}$ from each detector were combined in a matrix from which the annual dose in the j^{th} TL detector was calculated as

$$\begin{pmatrix} x_{1-9,1} & x_{10,1} & x_{11,1} \\ \vdots & \vdots & \vdots \\ x_{1-9,10} & x_{10,10} & x_{11,10} \end{pmatrix} \cdot \begin{pmatrix} A_{1-9} \\ A_{10} \\ A_{11} \end{pmatrix} = \begin{pmatrix} y_1^{TLD} \\ \vdots \\ y_{10}^{TLD} \end{pmatrix}, \tag{5.2}$$

with A_i being the activity of either the combined sources A_{1-9} or the activity of sources A_{10} and A_{11}. By fitting the calculated annual doses to the measured ones, optimized estimates for the activities were determined.

With the volumes V_i of each source cell, the specific activity of each cell was calculated:

$$A_i = A_{1-9} \cdot \frac{V_i}{\sum_{i=1}^{9} V_i} \quad \text{for } i = [1 \ldots 9] \tag{5.3}$$

$$A_i = \frac{A_i}{V_i} \quad \text{for } i = [10, 11] \tag{5.4}$$

Source cell	Volume (m^3)	Specific activity (10^{10} Bq m^{-3})
1	35.86	3.57 ± 0.16
2	72.00	7.17 ± 0.32
3	108.00	10.76 ± 0.48
4	111.94	11.15 ± 0.50
5	37.50	3.74 ± 0.17
6	150.00	14.95 ± 0.66
7	51.09	5.09 ± 0.23
8	26.10	4.88 ± 0.51
9	60.90	11.39 ± 1.20
10	57.87	4.17 ± 2.51
11	300.00	1.17 ± 0.24

Table 5.2: Specific Activity in the Source Cells
The table shows the volume and the calculated specific activity in each source cell.

The specific activity in each source cell is shown in table 5.2. The error of the specific activity was estimated in a weighted fit from the error of the TLD measurements.

For all the calculations, it was assumed that the contamination is homogeneously distributed up to 30 cm depth (see section 4.4.2).
To be mathematically more stable, the optimization was performed separately for the sources and the detectors to the North and to the South of the church tower. The impact of the sources in the North to the detectors in the South and vice versa was some orders of magnitude smaller than the contribution to the detectors of the same side.

With the estimation of the activity of the source cells, the annual dose at the sampling positions on the church tower was estimated from the calculations. Therefore the dose per photon matrix from equation (5.2) was multiplied by the activity of the sources. This was performed for the locations where TL dosimeter measurements were performed in order to verify the reservoir model and the determined doses.

$$\begin{pmatrix} x_{1-9,1} & x_{10,1} & x_{11,1} \\ \vdots & \vdots & \vdots \\ x_{1-9,10} & x_{10,10} & x_{11,10} \end{pmatrix} \cdot \begin{pmatrix} A_{1-9} \pm \Delta A_{1-9} \\ A_{10} \pm \Delta A_{10} \\ A_{11} \pm \Delta A_{11}. \end{pmatrix} = \begin{pmatrix} y_1^{calc} \pm \Delta y_1^{calc} \\ \vdots \\ y_{10}^{calc} \pm \Delta y_{10}^{calc} \end{pmatrix} \tag{5.5}$$

For the sampling sites without TLD measurement, $J = [11 \ldots 16]$, it was now possible to determine annual doses using the reservoir model with the same approach as before:

$$\begin{pmatrix} x_{1-9,11} & x_{10,11} & x_{11,11} \\ \vdots & \vdots & \vdots \\ x_{1-9,16} & x_{10,16} & x_{11,16} \end{pmatrix} \cdot \begin{pmatrix} A_{1-9} \pm \Delta A_{1-9} \\ A_{10} \pm \Delta A_{10} \\ A_{11} \pm \Delta A_{11} \end{pmatrix} = \begin{pmatrix} y_{11}^{calc} \pm \Delta y_{11}^{calc} \\ \vdots \\ y_{16}^{calc} \pm \Delta y_{16}^{calc} \end{pmatrix} \tag{5.6}$$

The measured annual doses in TLD are shown in figure 5.7 and table 5.3. The first section of the table shows the annual doses determined with the reservoir model for locations with a TLD measurement. The annual doses with no reference measurement are shown in the second section. As it was discussed before, analyzing the height profiles, the calculated and measured doses match for this source configurations. For the sampling sites where TLD measurements are available, the simulated doses are within the error of the measurements. This gives trust in the model and it was assumed that the doses for the sampling sites without TLD reference measurements were also correctly estimated.

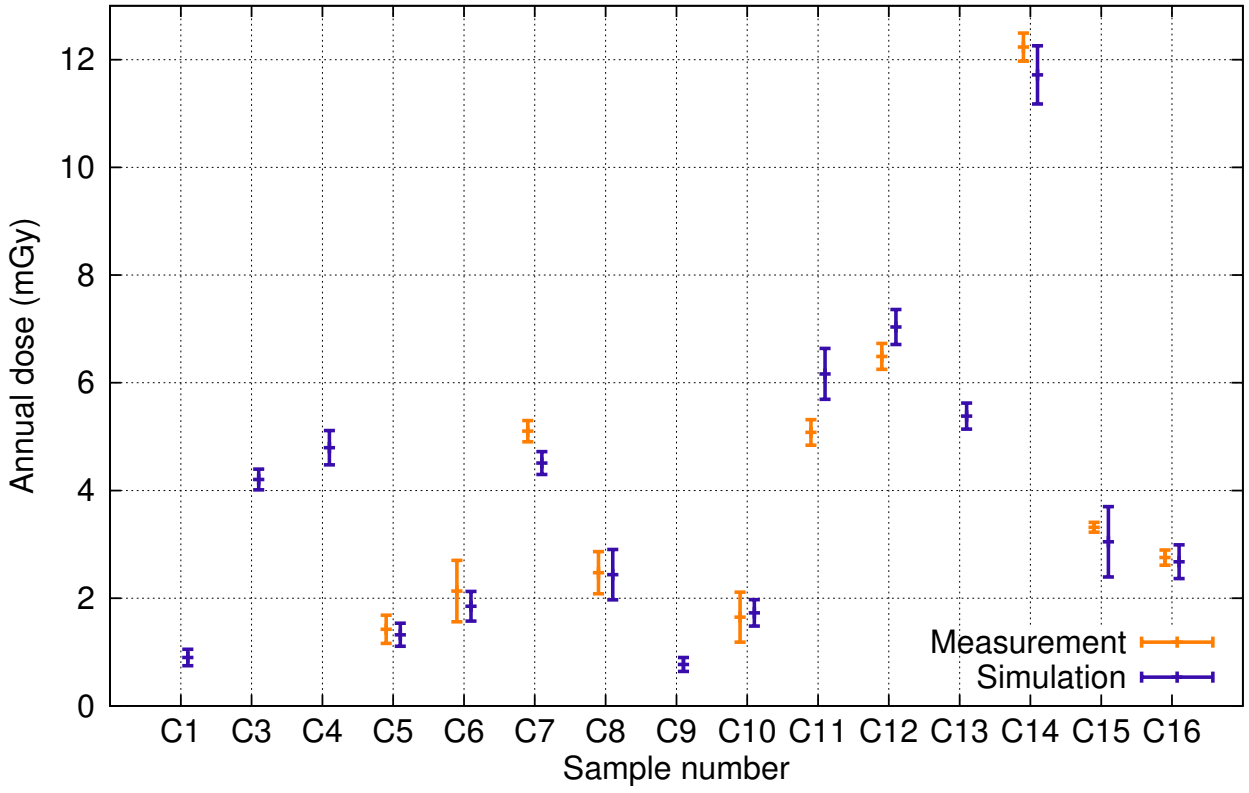

Figure 5.7: Annual Dose in TLD
The annual dose at the sampling sites was calculated using the reservoir model and measured using TLD.

Sample	Measured (mGy)	Calculated (mGy)	Sample	Calculated (mGy)
C5	1.421 ± 0.262	1.321 ± 0.214	C1	0.899 ± 0.154
C6	2.131 ± 0.571	1.851 ± 0.276	C3	4.205 ± 0.193
C7	5.102 ± 0.197	4.510 ± 0.212	C4	4.794 ± 0.319
C8	2.474 ± 0.390	2.437 ± 0.467	C9	0.769 ± 0.130
C10	1.648 ± 0.465	1.727 ± 0.245	C13	5.382 ± 0.243
C11	5.078 ± 0.236	6.165 ± 0.473		
C12	6.489 ± 0.240	7.035 ± 0.325		
C14	12.233 ± 0.260	11.716 ± 0.541		
C15	3.317 ± 0.091	3.046 ± 0.652		
C16	2.754 ± 0.141	2.677 ± 0.315		

Table 5.3: Annual Dose in TLD

The annual dose at the sampling site in mGy. The first section shows the annual doses for the sampling sites with a reference measurement while the section shows the calculated annual dose at the sampling sites with no TLD measurements.

5.1.2 Reservoir Dose

The reservoir dose, the dose accumulated in brick for the time after the creation of the reservoir lake (1956 – 2012) was assessed using the calculated annual doses. Therefore, and integral dose for this time was calculated using the doses rates estimated for the year 2012.

To calculate the reservoir dose for the time period from 1956 to 2012 based on the dose rates in 2012, not only the radioactive decay of ^{137}Cs nuclide, but also the migration of ^{137}Cs in the ground were considered, which are accounted for in the concept of the effective half-life.
This effective half-life, $T_{1/2,eff}$, was defined as the combination of physical half-life, $T_{1/2,phys}$, and ecological half-life $T_{1/2,ecol}$: "An ecological half-life describes the attenuation of a dose contribution due to ecological processes, e.g., due to migration into the soil or fixation to the soil matrix. An effective half-life describes the total attenuation rate taking radioactive decay into account." [39, 52, 53] The effective half-life is calculated as:

$$T_{1/2,eff} = \frac{T_{1/2,ecol} \cdot T_{1/2,phys}}{T_{1/2,ecol} + T_{1/2,phys}}. \tag{5.7}$$

The assessment of the effective half-life shown here was based on historic measurements and recent measurements of the specific activity of the radionuclide ^{137}Cs in the water of the reservoir lake. Such data was first compiled by Taranenko et al. [99] and complemented in this work by additional measurements from the URCRM archive [Shishkina et al., personal communication]. It was assumed, that the radionuclide activity in water is in a dynamic equilibrium with the activity in

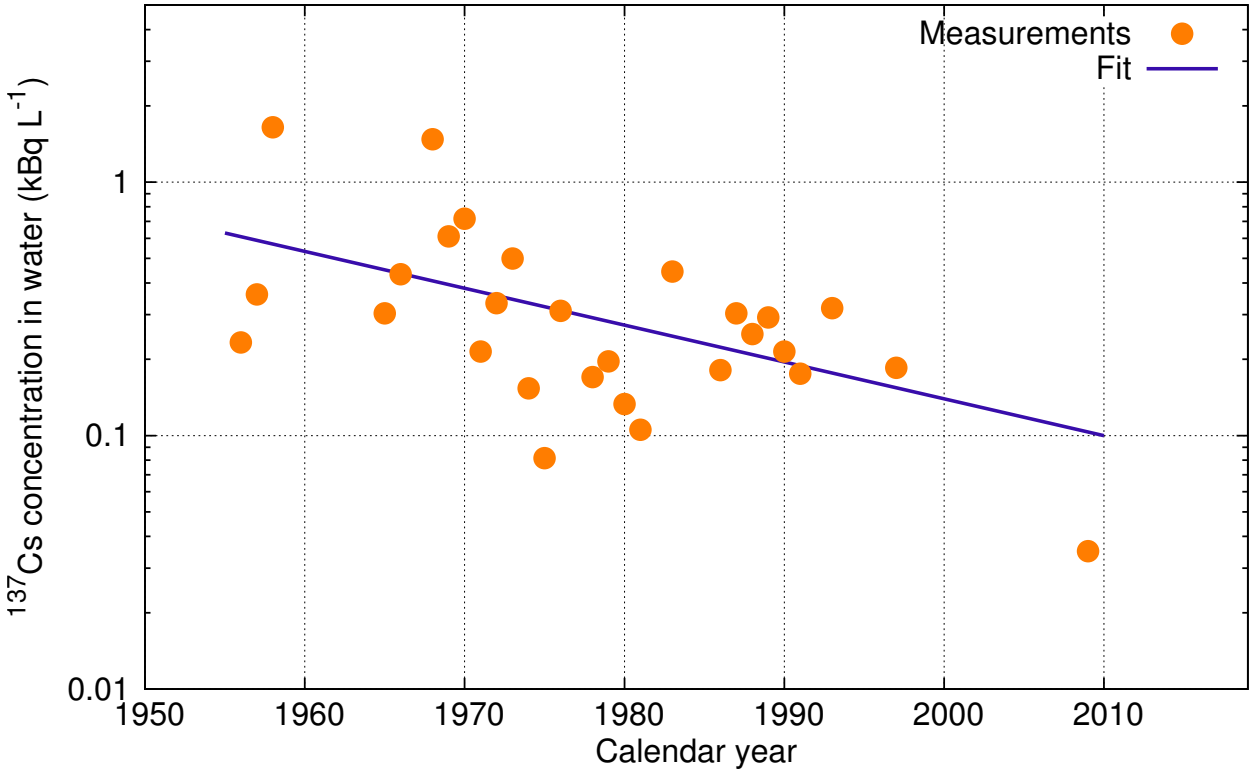

Figure 5.8: ^{137}Cs Concentration in Water as a Function of the Calendar Year
The effective half-life of ^{137}Cs was calculated using measurements of ^{137}Cs concentrations in the reservoir lake compiled by Taranenko et al. [99] and supplemented by newer data from the URCRM archive [Shishkina et al., personal communication].

the sediment, so that the former can be used as approximation for the latter.

The effective half-life of ^{137}Cs was evaluated by a linear fit to the logarithmic values of the data and was calculated to be 19.1 $\pm$ 5.3 a (see Fig. 5.8). This value is similar to the effective half-life of ^{137}Cs calculated by Jacob et al. [53] and to the effective half-life reported by Jacob et al. [52] for rural areas affected by the Chernobyl accident.
Due to the large scatter of the data, the error of the effective half-life is large, and amounts to over 50 % at the 95 % confidence level. The issues associated with this error are discussed later (see section 5.3.1).

With the effective half-life of the radionuclide ^{137}Cs and the annual dose in TLD, $\dot{D}_j^{2012}$ that was determined in the previous section, it was able to calculate the reservoir dose. The reservoir dose is the dose accumulated in brick between 1956 and 2012.

$$D_{X,j}^{Reservoir} = \int_{1956}^{2012} \dot{D}_j^{2012} \frac{P}{CF} e^{\lambda_{eff}(t-1956)} dt. \tag{5.8}$$

In this calculation, the conversion factor from dose in TLD to dose in brick of CF = 0.82 ± 0.16 was used to convert from doses calculated or simulated in the TLD to doses in brick (see section 4.1.3.3). Also a factor of P = 0.75 ± 0.05 for the absorption in plaster was considered (see section 4.1.3.5).
The reservoir dose was calculated for each brick sample separately. The results are shown in figure 5.9 and table 5.4.

The error of the reservoir dose $D_{X,j}^{Reservoir}$ includes the errors of the effective half-life $\Delta\lambda_{eff}$ and and annual dose $\Delta\dot{D}_j^{2012}$. The error was calculated with the law of the propagation of uncertainty:

$$\Delta D_{X,j}^{Reservoir} = \sqrt{\left(\frac{\partial D_{X,j}^{Reservoir}}{\partial \lambda_{eff}}\Delta\lambda_{eff}\right)^2 + \left(\frac{\partial D_{X,j}^{Reservoir}}{\partial \dot{D}_j^{2012}}\Delta\dot{D}_j^{2012}\right)^2} \tag{5.9}$$

It can be seen, that the sample positions facing towards the reservoir lake accumulate doses below 500 mGy, while the doses of the detectors facing towards the North have doses between 700 mGy and 2000 mGy.

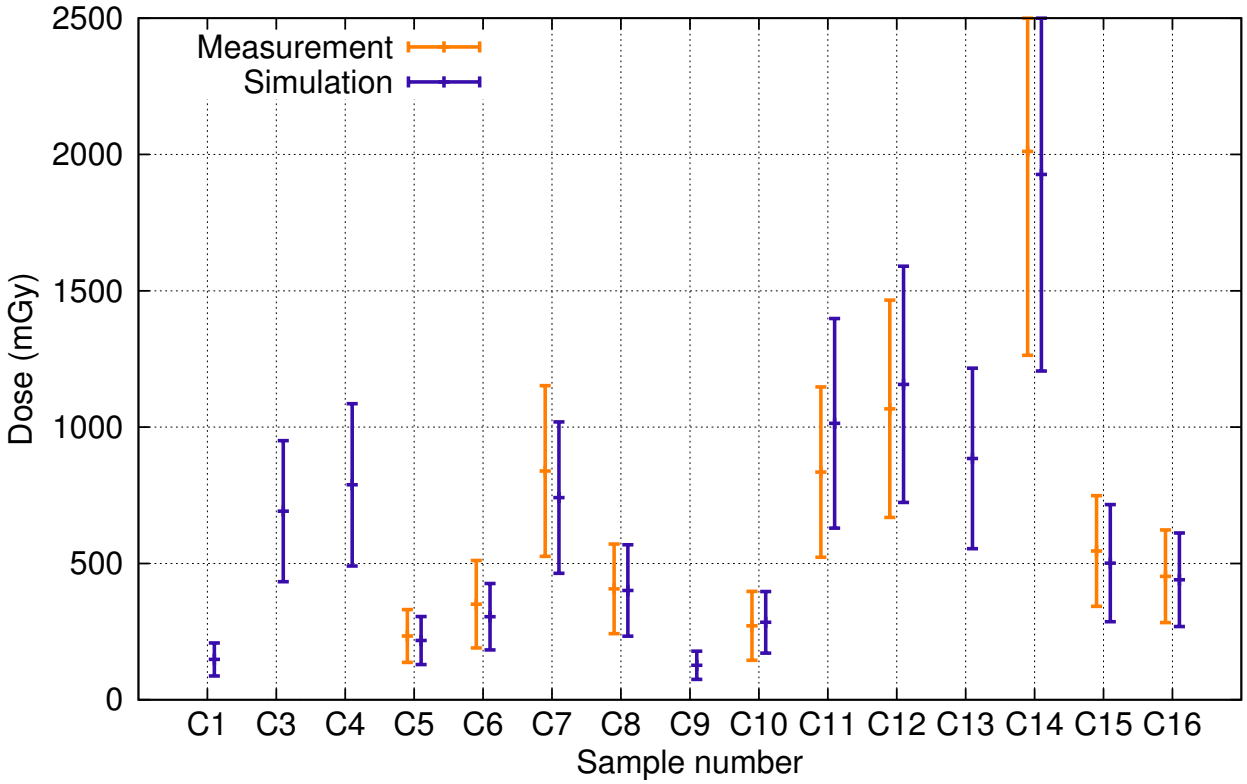

Figure 5.9: Reservoir Doses
The reservoir doses were estimated for all sampling sites using simulated contemporary dose rates and compared to doses derived from own TLD measurements where available.

Sample	Simulation (mGy)	Measurement (mGy)
C1	148 ± 60	
C3	691 ± 259	
C4	788 ± 298	
C5	217 ± 88	234 ± 97
C6	304 ± 122	350 ± 160
C7	742 ± 278	839 ± 313
C8	401 ± 168	407 ± 164
C9	126 ± 52	
C10	284 ± 113	271 ± 126
C11	1014 ± 385	835 ± 313
C12	1157 ± 433	1067 ± 398
C13	885 ± 331	
C14	1927 ± 721	2012 ± 749
C15	501 ± 215	546 ± 203
C16	440 ± 172	453 ± 170

Table 5.4: Reservoir Doses
The reservoir doses were estimated for all sampling sites using simulated contemporary dose rates and compared to doses derived from own TLD measurements where available.

5.1.3 Anthropogenic Dose in Brick from 1949 to 1956

The TL/OSL measurements of the brick samples (see section 3.2.2) showed the total anthropogenic dose accumulated in the brick $D_{X,j}^{Total}$. Together with the reservoir dose $D_{X,j}^{Reservoir}$ (Eq. 5.8), the anthropogenic dose in brick $D_{X,j}$ between 1949 and 1956 was calculated by subtracting the reservoir dose from the total dose in brick:

$$D_{X,j} = D_{X,j}^{Total} - D_{X,j}^{Reservoir} = D_{X,j}^{Total} - \int_{1956}^{2012} \dot{D}_j^{2012} \frac{P}{CF} e^{\lambda_{eff}(t-1956)} dt \qquad (5.10)$$

The error of the anthropogenic dose in brick from 1949 to 1956 $D_{X,j}$ includes the error of the effective half-life $\Delta\lambda_{eff}$, the error of the total dose in brick $D_{X,j}^{Total}$ and the error of the annual dose $\Delta\dot{D}_j^{2012}$. The error $\Delta D_{X,j}$ of the anthropogenic dose in brick from 1949 to 1956 was calculated with the law of the propagation of uncertainty:

$$\Delta D_{X,j} = \sqrt{\left(\frac{\partial D_{X,j}}{\partial D_{X,j}^{Total}} \Delta D_{X,j}^{Total}\right)^2 + \left(\frac{\partial D_{X,j}}{\partial \lambda_{eff}} \Delta\lambda_{eff}\right)^2 + \left(\frac{\partial D_{X,j}}{\partial \dot{D}_j^{2012}} \Delta\dot{D}_j^{2012}\right)^2} \qquad (5.11)$$

The results are shown in figure 5.10 and table 5.5. The first striking feature is, that the samples facing towards the North of the church tower show zero anthropogenic dose for the time from 1949 to 1956 (which is compatible with a zero dose within the error limits). This is reasonable as this area was not likely contaminated in the time before the creation of the reservoir lake. The calculations support this assumption (refer to section 4.4.3 for further discussion). The samples facing towards the Techa river show accumulated doses between 600 mGy and 800 mGy.

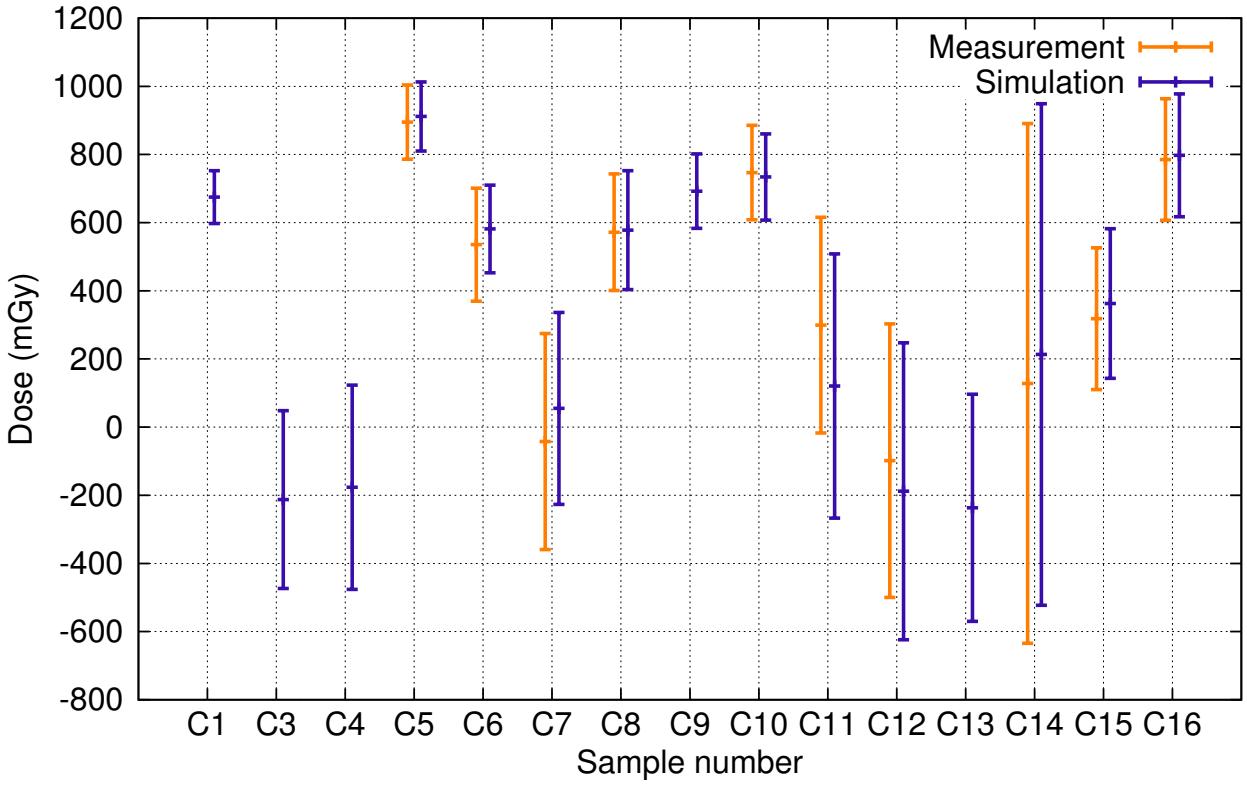

Figure 5.10: Anthropogenic Dose in Brick Between 1949 and 1956

Anthropogenic dose in bricks between 1949 and 1956 was estimated by subtracting the reservoir dose from the total dose in bricks.

Sample	Simulation (mGy)	Measurement (mGy)
C1	675 ± 77	
C3	-213 ± 261	
C4	-176 ± 300	
C5	912 ± 101	895 ± 109
C6	582 ± 129	535 ± 166
C7	55 ± 282	-42 ± 317
C8	578 ± 175	572 ± 171
C9	692 ± 109	
C10	734 ± 127	747 ± 139
C11	121 ± 388	299 ± 317
C12	-188 ± 436	-98 ± 401
C13	-237 ± 333	
C14	213 ± 736	128 ± 763
C15	363 ± 219	318 ± 208
C16	798 ± 180	785 ± 178

Table 5.5: Anthropogenic Dose in Brick Between 1949 and 1956
Anthropogenic dose in bricks between 1949 and 1956 was estimated by subtracting the reservoir dose from the total dose in bricks.

5.2 Estimation of the Time Integrated Air Kerma

It was possible to calculate the dose in brick for the time before the evacuation of Metlino using the reservoir model. The key parameter of the TRDS, the air kerma at shoreline, was evaluated using the Metlino model.

Little information is available about the distribution of the contamination and the activity in Metlino before the evacuation. Indirect indication of a heterogeneous contamination can be found from a few historic dose rate measurements at the shoreline and floodplain from 1951 – 1954, compiled in Taranenko et al. [99]. These measurements were however conducted at the right arm of the Techa river, South of the former mill and must not necessarily apply to the shorelines of the left river channel and floodplain close to the church. From the in-situ measurements of sediment activity, a uniform contamination of the entire area of interest is indicated. Therefore all sources were sampled equally in the Metlino model (see section 4.4.3).

To estimate the time integrated air kerma at the shoreline in Metlino, following steps were performed:

1. To test the validity of the Metlino model, the dose per photon in brick was calculated for corresponding sample positions on the South-Western and South-Eastern wall. The ratio of simulated doses was then corresponded with the measured ones.

2. The dose per photon in brick calculated with the Metlino model was compared to the dose per photon in air at shoreline calculated with the same model, resulting in a **D**ose **C**onversion **F**actor (DCF) between the dose in brick and the dose in air.
3. Multiplying the anthropogenic dose in brick $D_{X,j}$ for the years 1949 – 1956 with the conversion factor resulted in the integral air kerma at shoreline for the time between 1949 and 1956.

No absolute doses can be calculated for the Metlino model. But comparing the ratio of the anthropogenic dose in brick from 1949 – 1956 in two locations on the church tower derived from the measurement in the reservoir model with the ratio of the calculated dose per photon in the same locations in the Metlino model, should give the same ratio in both models, if the locations are sampled equally.
This was done for the samples along the South-Western and South-Eastern profile on the church tower that face towards the Techa river (see Fig. 3.4), and are therefore of interest in the Metlino model.

The ratio R of the dose in brick between the South-Western and the South-Eastern wall of the church tower for each sampling height was calculated:

$$R = \frac{D_{X,j}}{D_{X,j'}} = \frac{D_{X,j}^{Total} - \int_{1956}^{2012} \dot{D}_j^{2012} \frac{P}{CF} e^{\lambda_{eff}(t-1956)} dt}{D_{X,j'}^{Total} - \int_{1956}^{2012} \dot{D}_{j'}^{2012} \frac{P}{CF} e^{\lambda_{eff}(t-1956)} dt} \tag{5.12}$$

The error in the ratio R is calculated from the error of the effective half-life $\Delta T1/2_{eff}$, the errors of the doses in the two brick locations $\Delta D_{X,j}$ and $\Delta D_{X,j'}$ and the error of the corresponding annual doses $\Delta \dot{D}_j$ and $\Delta \dot{D}_{j'}$.

$$\Delta R = \sqrt{\left(\frac{\partial R}{\partial \lambda_{eff}} \Delta \lambda_{eff}\right)^2 + \left(\frac{\partial R}{\partial D_{X,j}} \Delta D_{X,j}\right)^2 + \left(\frac{\partial R}{\partial D_{X,j'}} \Delta D_{X,j'}\right)^2 + \left(\frac{\partial R}{\partial \dot{D}_j} \Delta \dot{D}_j\right)^2 + \left(\frac{\partial R}{\partial \dot{D}_j} \Delta \dot{D}_j\right)^2} \tag{5.13}$$

The sample positions compared were C15 with C16, C8 with C10 and C6 with C5 (see Fig. 5.11). The ratio of doses in the South-Western wall to doses in the South-Eastern wall is about 0.85 for the simulation with the Metlino model. The source distribution is uniform and no jumps in the dose are expected along the profiles of the church tower (see section 4.2, where a height profile along a brick wall is discussed). The best estimate for the ratio of the anthropogenic doses in brick from 1949 – 1956 derived from the measurements varies between 0.4 and 0.75. The comparatively large errors result of the dominant error of the effective half-life of ^{137}Cs. Within a 95 % confidence

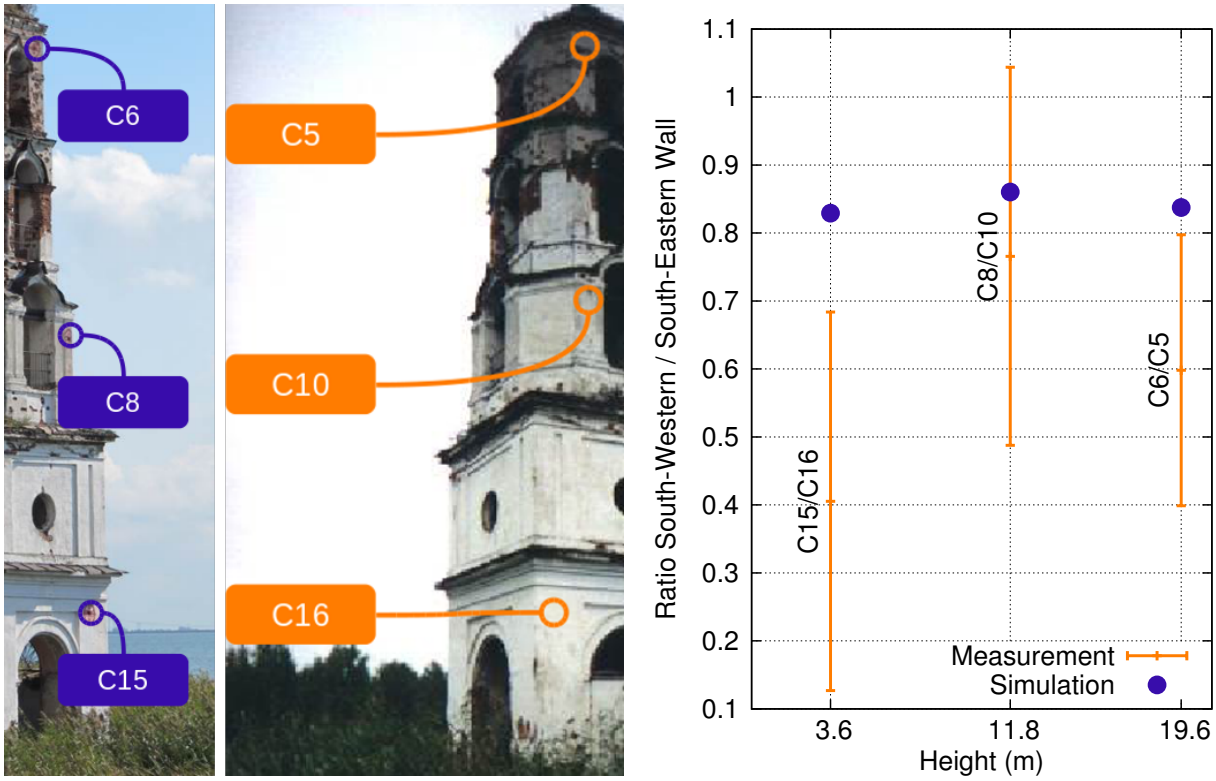

a. Sample positions

b. Ratio of doses at sample positions

Figure 5.11: Dose in Brick at South-Western and South-Eastern Wall

The dose in brick is compared between the calculations Metlino model and the anthropogenic dose in brick from 1949 to 1956 derived from the measurements for the South-Western and South-Eastern walls of the church tower.

interval (plotted errors are at the 1-σ level), an agreement between measured and calculated doses can be seen.

The height profile of the anthropogenic dose in brick from 1949 to 1956 of these samples (South-Western and South-Eastern profile) shows within the error margin a steady, or slightly rising dose with the height. The simulated and measured height profile agree within the error range. These height profiles are an indication of an extended, distant source.

The next step in the estimation of the integral air kerma at shoreline is to determine the ratio of the dose per source photon in the detectors in brick to the dose per source photon in the detectors in air. This ratio will give a matrix DCF to convert doses assessed for detectors in brick to doses in the reference locations in air.

The dose per photon in brick $D_{pp}^{brick}(C_j)$, given in units of 10^{-19} mGy, for all samples that face to the former Techa river is shown in table 5.6.

Detector Nr.	Dose (10^{-19} mGy)	Detector Nr.	Dose (10^{-19} mGy)
C15	3.73	C16	4.50
C8	4.78	C10	5.56
C6	4.49	C5	5.36
C1	8.37	C9	8.59

Table 5.6: Dose per Photon in Brick
The dose per photon in the detectors in brick D_{pp}^{brick} of the church tower facing towards the Techa river was calculated in the Metlino model. Doses are given in units of 10^{-19} mGy.

The dose per photon in air $D_{pp}^{air}(S_i)$ over the shoreline as well as over the floodplain and over other areas of the geometry was calculated with the Metlino model (see Fig. 5.12 and Tab. 5.7). Thirteen detectors in air S_i, $i = [1...13]$ were distributed along the shoreline. Detectors 1, 2, 3, 6, 7, 8, 10 and 11 were placed 1 m above source areas, while detectors 4, 5, 9, 12 and 13 were not in direct vicinity to sources.
Seven circular detectors S_i, $i = [101...107]$ were distributed in the Metlino model. Detectors 101 – 105 were over the floodplain while detector 106 was over the Techa river between two source areas and detector 107 was away from sources.
The detectors in air at shoreline showed average dose per photon of $3.85 \cdot 10^{-18}$ mGy while the floodplain detectors showed an average dose per photon of $7.02 \cdot 10^{-18}$ mGy. The detectors away from sources obviously showed much lower doses.
The shoreline detectors accumulate lower doses as there is no source to one side of the detector. The overall difference in calculated doses within the shoreline detectors and floodplain detectors, respectively, is low because the source is homogeneously distributed. The small numeric differences between e.g. detectors 101 and 105 are due to the different finite extension of the source areas.

The ratio of the dose per photon in brick, $D_{pp}^{brick}(C_j)$ to the dose per photon in air, $D_{pp}^{air}(S_i)$, called the **d**ose **c**onversion **f**actor (DCF), was calculated as:

$$DCF_{i,j} = \frac{D_{pp}^{brick}(C_j)}{D_{pp}^{air}(S_i)}. \tag{5.14}$$

The variability within the detectors in air at shoreline and the and the detectors in air over the floodplain is small, therefore an averaged dose conversion factor for shoreline and one for the floodplain detectors was calculated. The dose conversion factor shows different values regarding the selection of the corresponding detector in brick (see Tab. 5.8).

With the anthropogenic dose in brick between 1949 and 1956, $D_{X,j}$ (see Eq. 5.10), the integral air kerma at shoreline can be calculated as the product of the dose in brick and the dose conversion factor DCF.

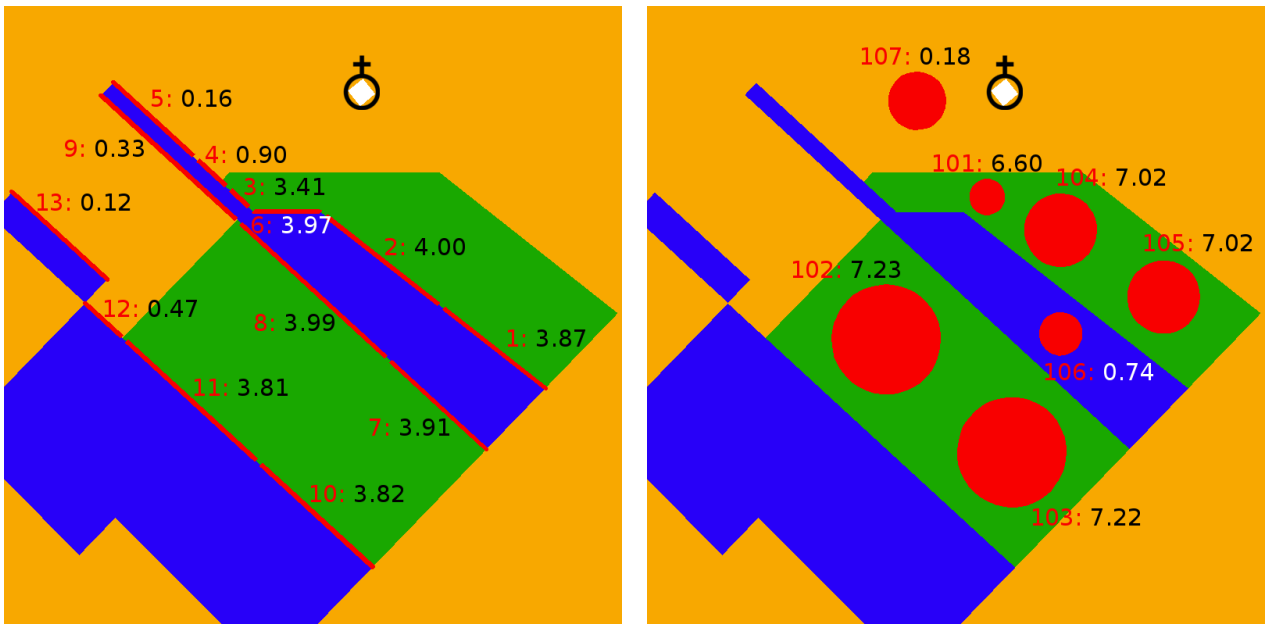

a. Shoreline detectors **b.** Floodplain detectors

Figure 5.12: Dose in Air

The dose in the simulated detectors in air at the shoreline and over the floodplain was calculated. The number of the detector is indicated in red, the dose per photon in 10^{-18} mGy is in black. The sources are indicated in green, the Techa river in blue and the detectors in air in red.

	Detectors at shoreline		Detectors at floodplain	
	Detector Nr.	Dose (10^{-18} mGy)	Detector Nr.	Dose (10^{-18} mGy)
Over sources	1	3.87	101	6.60
	2	4.00	102	7.23
	3	3.41	103	7.22
	6	3.97	104	7.02
	7	3.91	105	7.02
	8	3.99		
	10	3.82		
	11	3.81		
	Average	**3.85 ± 0.19**	**Average**	**7.02 ± 0.26**
Away from sources	4	0.90	106	0.74
	5	0.16	107	0.18
	9	0.33		
	12	0.47		
	13	0.12		

Table 5.7: Dose per Photon at Various Locations in the Metlino Model

The dose per photon in air D_{pp}^{air} for detectors over the shoreline and for the floodplain detectors was calculated.

Brick sample	DCF	Brick sample	DCF
C15	0.097	C16	0.117
C8	0.124	C10	0.145
C6	0.117	C5	0.139
C1	0.218	C9	0.223

Table 5.8: Dose Conversion Factors
The ratio of the dose per photon in the detectors in brick to the average dose at the shoreline was calculated.

Sample	Air kerma (Gy)	Sample	Air kerma (Gy)
C15	3.74 ± 2.26	C16	6.82 ± 1.54
C8	4.65 ± 1.40	C10	5.08 ± 0.88
C6	4.98 ± 1.10	C5	6.54 ± 0.73
C1	3.10 ± 0.36	C9	3.10 ± 0.49

Table 5.9: Time Integrated Air Kerma at Shoreline
The integral air kerma between 1949 and 1956 was averaged over the shoreline detectors.

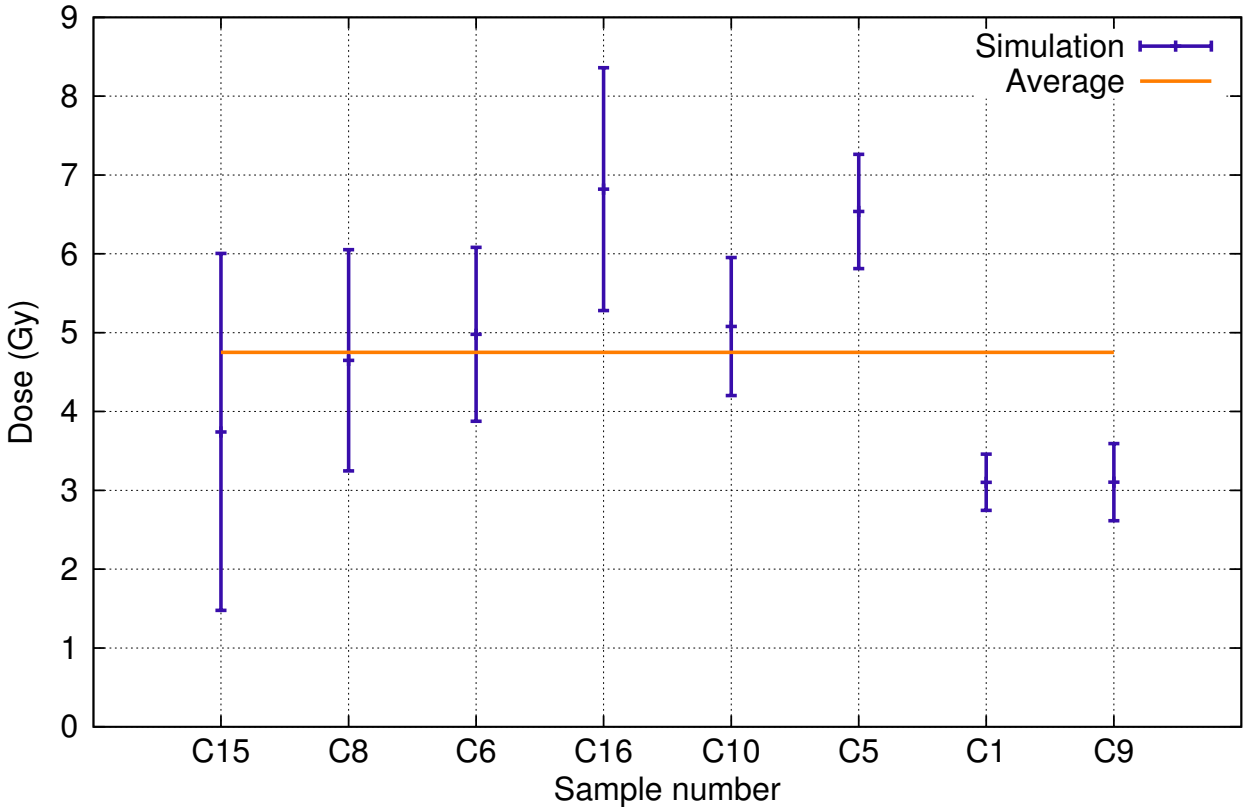

Figure 5.13: Time Integrated Air Kerma at Shoreline
The air kerma between 1949 and 1956 was calculated for the averaged detector over the shoreline.

$$K_{air,\,i,j} \;=\; DCF_{i,j} \cdot D_{X,j} \;=\; \frac{D_{pp}^{brick}(C_j)}{D_{pp}^{air}(S_i)} \cdot D_{X,j} \tag{5.15}$$

The error of the integral air kerma at shoreline $\Delta K_{air,\,i,j}$ depends on the error of the dose in Brick $\Delta D_{X,j}$. The dose conversion factor is directly determined from MCNP calculations and has a negligible error. The impact of different source configurations will be discussed in section 6.2.

$$\Delta K_{air,\,i,j} = \sqrt{\left(\frac{\partial K_{air,\,i,j}}{\partial D_{X,j}} \Delta D_{X,j}\right)^2}; \qquad \frac{\Delta K_{air,\,i,j}}{K_{air,\,i,j}} = \frac{\Delta D_{X,j}}{D_{X,j}} \tag{5.16}$$

Depending on the selected detector in brick at the church tower, the best estimate for the air kerma varies between 3.7 Gy and 6.8 Gy for the time period from 1949 to 1956 for the shoreline, the average is at 5.3 Gy (see Tab. 5.9 and Fig. 5.13). Figure 5.13 also shows, that the air kerma for the samples C15, C8 and C6 at the South-Western wall agree quite well, while the samples on the South-Eastern wall are more scattered.

5.3 Probabilistic Approach

The deterministic approach showed in clear and distinct steps the basic principle of the determination of the integral air kerma at shoreline. But it has two major drawbacks. First, not all sources of error could be considered (e.g. dose rate measurements). Secondly, the law of error propagation is only valid for errors being small compared to the data, so that the change of the dependent variable can be approximated by the linear term of the Taylor expansion. Especially for the parameter of the effective half-life it is questionable, whether this requirement is really met.
These issues can be overcome by a probabilistic approach, varying all (uncorrelated) input parameter within their uncertainty and assessing the distribution in the resulting air kerma value.

For this, the single calculations were implemented into a program using Matlab [101]. All measured and calculated input data were fed into the program with the associated errors.
In a large number of runs (20.000) a new value from within the error limit of the measurement was sampled. Finally, an air kerma matrix was evaluated referring each of the 20 detectors in air to each of the 8 detectors in brick:

$$\boldsymbol{K_{air}}(x_{i,j,n}). \tag{5.17}$$

With $i = [1 \ldots 20]$, the detectors in air (see Tab. 5.7), $j = [1 \ldots 8]$, the detectors in brick: C15, C8, C6, C16, C10, C5, C1, C9 (see Fig. 5.11 and Fig. 3.4) and $n = [1 \ldots 20.000]$ the runs.

From the matrix $\boldsymbol{K_{air}}(x_{i,j,n})$, air kerma ranges were evaluated for selected reference points in air.

The dose rate in air measurements had an error of 20 %. The activity of the sources was determined in a weighted fit, where the actually measured values of the TLD and their errors were used as an input. The effective half-life of the ^{137}Cs nuclide and the dose in brick were sampled within their error limits.

As it was shown before, there is only a little variability in the air kerma values at the shoreline. Therefore the air kerma values were calculated for the averaged shoreline (see Fig. 5.14). The 95 % confidence interval for the air kerma was estimated. While there is little variability depending on the detector in air, this shows the variability of the air kerma depending on the selected detector in brick.

The large error in the effective half-life of radionuclide ^{137}Cs introduces a large asymmetric uncertainty in the numerically determined air kerma values, the median does not accord with the best estimate. This approach shows, that the classical error estimation underestimates the error, it denotes a non-linear behavior of the function within the error limit. For some values, the error is not significantly distinguishable from zero.

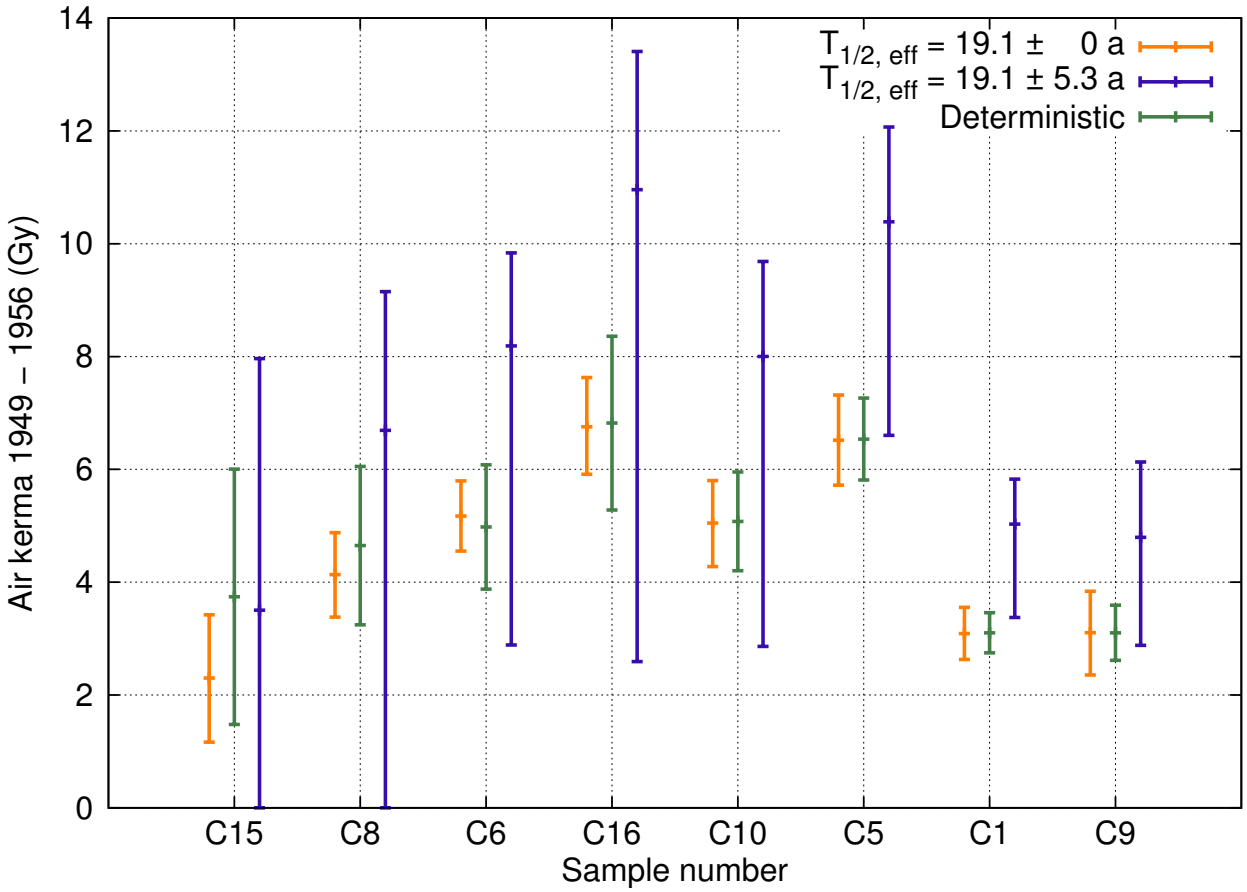

Figure 5.14: Integral Air Kerma at Shoreline

The integral air kerma at the shoreline between 1949 and 1956 was calculated with the probabilistic approach. The air kerma varies depending on the selected detector in brick.

5.3.1 Alternative Estimation of the Effective Half-Life of the Radionuclide ^{137}Cs

As it can be seen in figure 5.14, the large error in the effective half-life of the radionuclide ^{137}Cs acts as the main source of uncertainty in the estimation of the air kerma the shoreline. The estimation of the effective half-life is based on measurements of the ^{137}Cs concentration in the water of the reservoir lake (see figure 5.8). They show wide scattered data points, thus creating a large error on the effective half-life of 19.1 ± 5.3 a.

A different approach to estimate the effective half-life of the radionuclide ^{137}Cs can be made. Figure 5.10 shows, that in various samples an anthropogenic dose for the time period from 1959 – 1956 is measured that is compatible with a zero dose within the error limits. These samples, C3, C4, C7, C11 – C14 (see Fig. 3.4) face away from the Techa river and its contaminated floodplains (see Fig. 4.21). Therefore, it is probable, that they did not accumulate any dose above background in the time before the evacuation. Only after the creation of the reservoir lake, the area to the North of the church tower became contaminated (see Fig. 4.21b). All anthropogenic dose in these samples was thus probably accumulated after the evacuation.
Assuming there was no anthropogenic dose on the samples in the church tower facing away from the Techa river, other than the reservoir dose, the effective half-life can be calculated for these sample positions using the brick dose and the back-calculated integral annual dose in TLD.

With $\dot{D}_j^{2012}$ the annual dose in the TLD, and $D_{X,j}^{Total}$ the dose in brick, the effective half-life can be calculated for the four detectors j in question (C7, C12, C14 and C20) by solving the equation

$$D_{X,j}^{Total} = \int_{1956}^{2012} \dot{D}_j^{2012} \frac{P}{CF} \exp\left\{\frac{\ln(2)}{T_{1/2,eff}}(t - 1956)\right\} dt \tag{5.18}$$

for $T_{1/2,eff}$. The constant $\frac{P}{CF}$ accounts for the absorption in the plaster and the conversion factor between dose in brick to dose in TLD, as shown above.

Taking the average of the estimates for the four samples, shown in table 5.10 and calculating the standard deviation results in a value for the effective half-life of ^{137}Cs of $T_{1/2,eff} = 18.7 \pm 2.0$ a.

This value is within the errors in agreement with the value derived from the water measurements of the reservoir lake, but has a 50 % lower statistical uncertainty. Figure 5.15 shows the calculated integral air kerma at shoreline and compares the two approaches of determining effective half-life of ^{137}Cs. As it can be seen from the plots, the alternative estimation reduces the error of the integral air kerma at shoreline significantly.

Sample	Effective half-life (a)
C7	19.9
C12	20.6
C14	18.3
C20	16.0

Table 5.10: Effective Half-Lives Calculated for Selected Sites at the Church Tower
The effective half-life of the radionuclide ^{137}Cs was calculated for the spots facing away from the Techa river, they were not exposed to contamination before the creation of the reservoir lake.

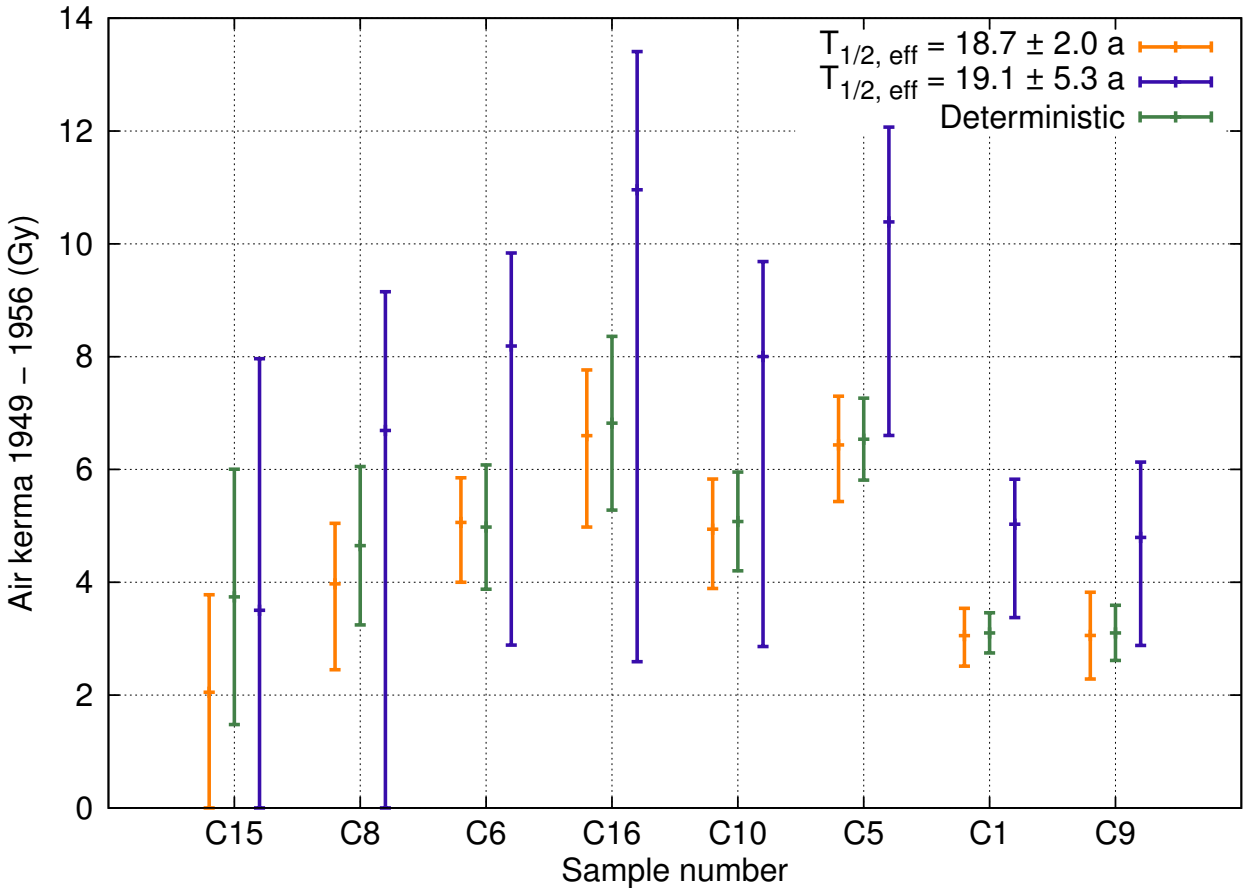

Figure 5.15: Integral Air Kerma at Shoreline
The integral air kerma at shoreline between 1949 and 1956 was calculated with the probabilistic approach. The two approaches of determining effective half-life of ^{137}Cs were compared.

Chapter 6

Discussion

In the following, several parameters influencing the integral air kerma above shoreline shall be discussed. The first section deals with external influences that can have an impact on the observation and measurements performed in the Metlino area. The second section discusses variations in the models for the Metlino area and their influence on the time integrated air kerma above shoreline. The last section compares the integral air kerma at the shoreline in Metlino as it was derived in this work with the air kerma values from the Techa River Dosimetry System.

6.1 Environmental Influences on Dosimetric Results

6.1.1 Soil Types

In section 4.1.2.2 two different soil types, from Eckerman and Ryman [37] with a density of 1.6 g cm^{-3} and from in Saito and Jacob [92] with a density of 1.0 g cm^{-3} were used in the simulation.
The influence of the two different soil types on the energy spectrum was investigated. There is an effect on the calculated result depending on the selected soil type, but this is very low. Both of them showed very comparable results. The soil type presented by Eckerman and Ryman in the *Federal Guidance Report Nr. 12* is widely used and tested, therefore it was decided to also use this soil type in the calculations for Metlino. This is also the soil type that was used by Taranenko et al. [99] for the simulations in Metlino.

6.1.2 Water Levels in Metlino

The observations from the field trips to Metlino in three subsequent years and also from reports of former field trips clearly show, that the water level in the swampy areas in Metlino changes strongly between the years.
In the 2011 field trip, the path from the North towards the church was comparatively swampy (see

Fig. 6.1), in the 2012 and 2013 field trips, the path was almost dry, with only a few wet spots. From the 2007 field trip, similar conditions or even conditions with higher water levels as during the 2011 field trip were reported.

Periods of strong rainfall or droughts can influence the water level in both the reservoir lake and the Metlinski pond. Section 4.3 shows the effect of the absorption by water.

a. 2007 **b.** 2011 **c.** 2012

Figure 6.1: Water Level Variation

The figure shows the variation in the water level in Metlino between the 2007, 2011 and 2012 field trips, all performed in September. The area to the North of the church tower was partly covered with water in 2007, swampy in 2011 and very dry in 2012.

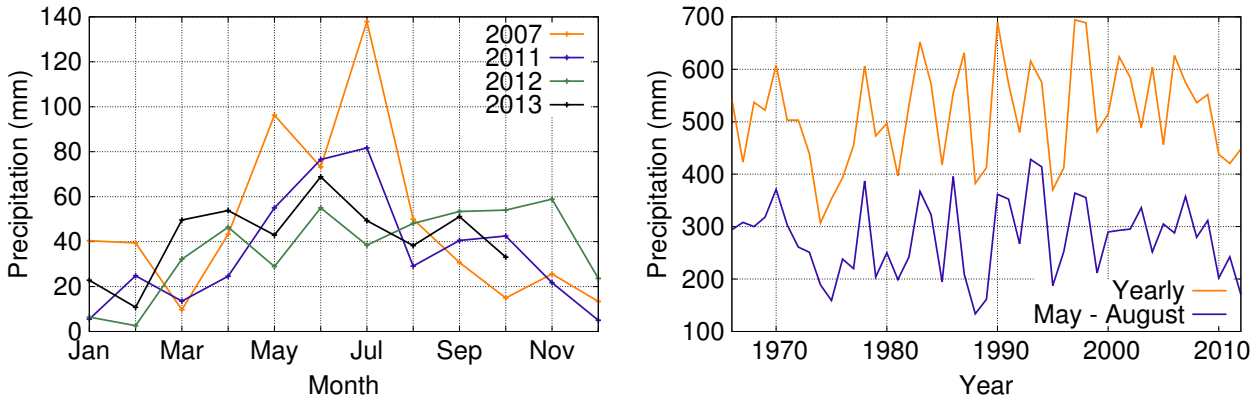

a. Monthly **b.** Annual

Figure 6.2: Precipitation in the Yekaterinburg Area

The precipitation varies strongly between the years of the field trips, 2007, 2011, 2012 and 2013 as well as in the years from 1966 to 2012. Data from RIHMI-WDC database. The annual precipitation rates show a strong variation between the total rainfall in the years as well as between the rainfall in the summer month.

To demonstrate the different precipitation rates between the month of a year and between different years, the precipitation rate in the Yekaterinburg area ($\approx$ 150 km away from Metlino) was analyzed. This was the nearest spot with reliable weather data information, using the RIHMI-WDC database.
Figure 6.2a shows the strong variation in the monthly rainfall for the Yekaterinburg area for the years 2007, 2011, 2012 and 2013, especially for the month of September when the field trips were performed.
As it can be seen from figure 6.2b, the rainfall in the Yekaterinburg varies quit a lot in the years from 1966 – 2012. Some years have almost 700 mm of rainfall others less than 400 mm.

6.1.3 Moisture Content in Soil

A bigger difference than through the soil type is introduced through the moisture content in the soil. The water content in the swampy areas of Metlino changes quite frequently between the month of a year and also from one year to the other with the variation of the precipitation (see section 6.1.2). Therefore, also the moisture content of the soil is expected to vary over the year and also between following years.

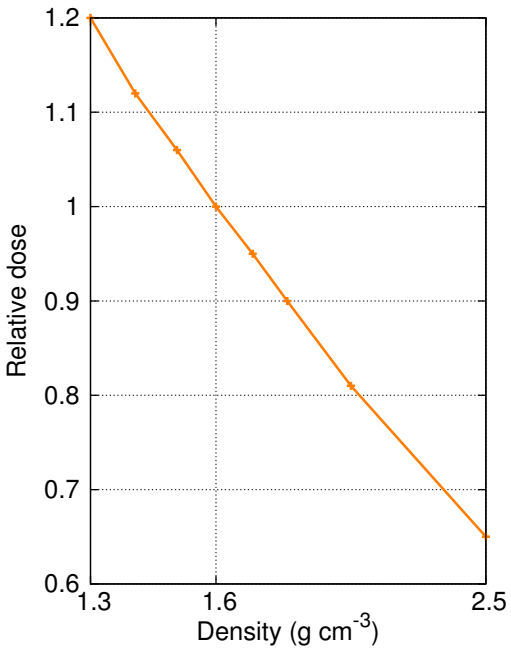

Figure 6.3: Water Content in Soil
The water content in soil was varied by altering its density between 1.3 g cm^{-3} and 2.5 g cm^{-3}. The relative dose per photon to the standard density of 1.6 g cm^{-3} is shown. The dose is rapidly decreasing with the density of the soil.

The water content in soil is assumed to mainly affect the density of the soil. The initial soil density of 1.6 g cm^{-3} of the soil taken from Eckerman and Ryman [37] was varied in a series of Monte Carlo calculations from lower values of only 1.3 g cm^{-3} to account for dryer periods to densities of up to 2.5 g cm^{-3} to account for wetter conditions.

The dose per photon in the detectors C1 – C21 was sampled at the reservoir model. The relative dose compared to a density of 1.6 g cm^{-3} was calculated and averaged over all detectors. Figure 6.3 shows that the dose rapidly decreases with the density. This also agrees with the calculations shown in section 4.3 where a source shielded by an increasingly thick water layer was simulated.

It can be concluded, that the radiation gets shielded quite effectively in times with high water levels in Metlino, thus reducing the dose at the sampling sites.

6.1.4 Snow Shielding Factor

The snow cover in the winter reduces the dose recorded in the TLD or bricks compared to an uncovered site. When dose rate measurements taken over a time period of a few minutes in the summer get extrapolated to a full year, the attenuation by the snow cover in the winter has to be considered for a more realistic estimate of the annual dose. This snow shielding factor of ≈ 0.85 was integrated into the calculations as proposed by Taranenko et al. [99] and Jacob et al. [54].

6.1.5 Effect of the Environmental Conditions on the Data Interpretation

The observations presented here show one of the main difficulties when analyzing data from the Metlino area: The weather conditions strongly affect the outcome of the observations. This influences the interpretation of the gathered data in various points:

- The dose rate measurements performed in air with the Automess only reflect the current situation in Metlino.
- Extrapolating the dose rate measurements in air to annual doses and comparing them to TLD measurements that average over a year is error-prone. The conditions are likely to change from time to time over the year, thus strongly influencing the dose rates.
- Comparing the measurements from different years is as risky. Very dry years follow very wet ones.
- The uncertainty for all these measurements is, that is not possible to describe the irradiation conditions over the time, and that it is thus not possible to compensate for all these variations.

The weather recordings give a hint for the observation, that the dose rates measured in Metlino change between the years. Higher water content in soil or a water layer on top of the soil (as shown in section 4.3) absorbs the radiation quite strongly and thus leads to measurements of a reduced dose rate. This makes a comparison of measurements from different years difficult. It can be recommended for future work, that all relevant data is gathered in the same year, to avoid contradictory results from different years due to different water levels.

6.2 Variation of the Source Configuration in the Metlino Model

6.2.1 Depth Distribution of Radionuclides

For the Metlino model, three different source depth configurations were simulated: A standard source depth with 5 cm and a flat- and a deep source configuration with 2 cm and 10 cm source depth (see section 4.4.3).

In the simulations of the Metlino model presented so far, the standard source with a depth of 5 cm was used for the calculations. The integral air kerma at shoreline for the time between 1949 and 1956 was also evaluated for the flat and for the deep source configuration.
The Monte Carlo calculations on the Metlino model with different source depths show, that the source depth has only a small influence on the integral air kerma at shoreline (see Fig. 6.4).

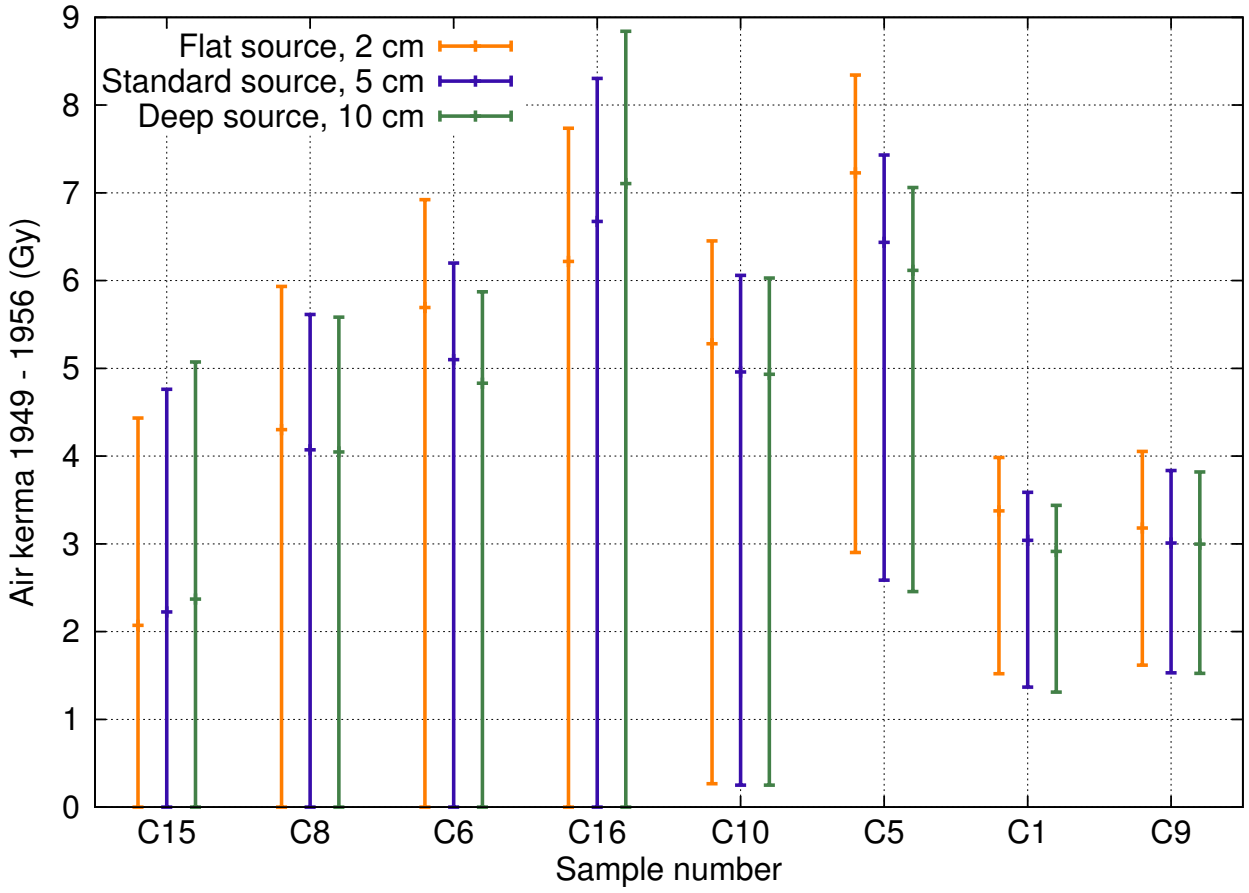

Figure 6.4: Impact of the Source Depth to the Integral Air Kerma at the Shoreline
The air kerma at shoreline was calculated for a flatter, 2 cm deep and a deeper, 10 cm deep source, compared to the standard 5 cm source in the Metlino model. The air kerma slightly varies with the source depth, about 2 % lower for the flatter source and 2.5 % higher for the deeper source. For these calculations, an effective half-life of ^{137}Cs of 19.1 $\pm$ 5.3 a was assumed.

There is only an about 2 % lower air kerma for the flatter source and an about 2.5 % higher air kerma value for the deeper source.

The calculations in section 4.2 show, that a deeper source configuration leads to a flatter height profile. This can also be seen in the case of the Metlino model, but the spatial distribution of the source is so large compared to the difference in the depth distribution that this effect plays only an insignificant role.

Figure 6.4 shows the air kerma on the shoreline with the source depth for the effective half-life of the radionuclide ^{137}Cs of 19.1 $\pm$ 5.3 a, while figure 6.5 shows the same for the alternative determination of the effective half-life with 18.7 $\pm$ 2.0 a. This again shows the impact of the error in the effective half-life on the air kerma.

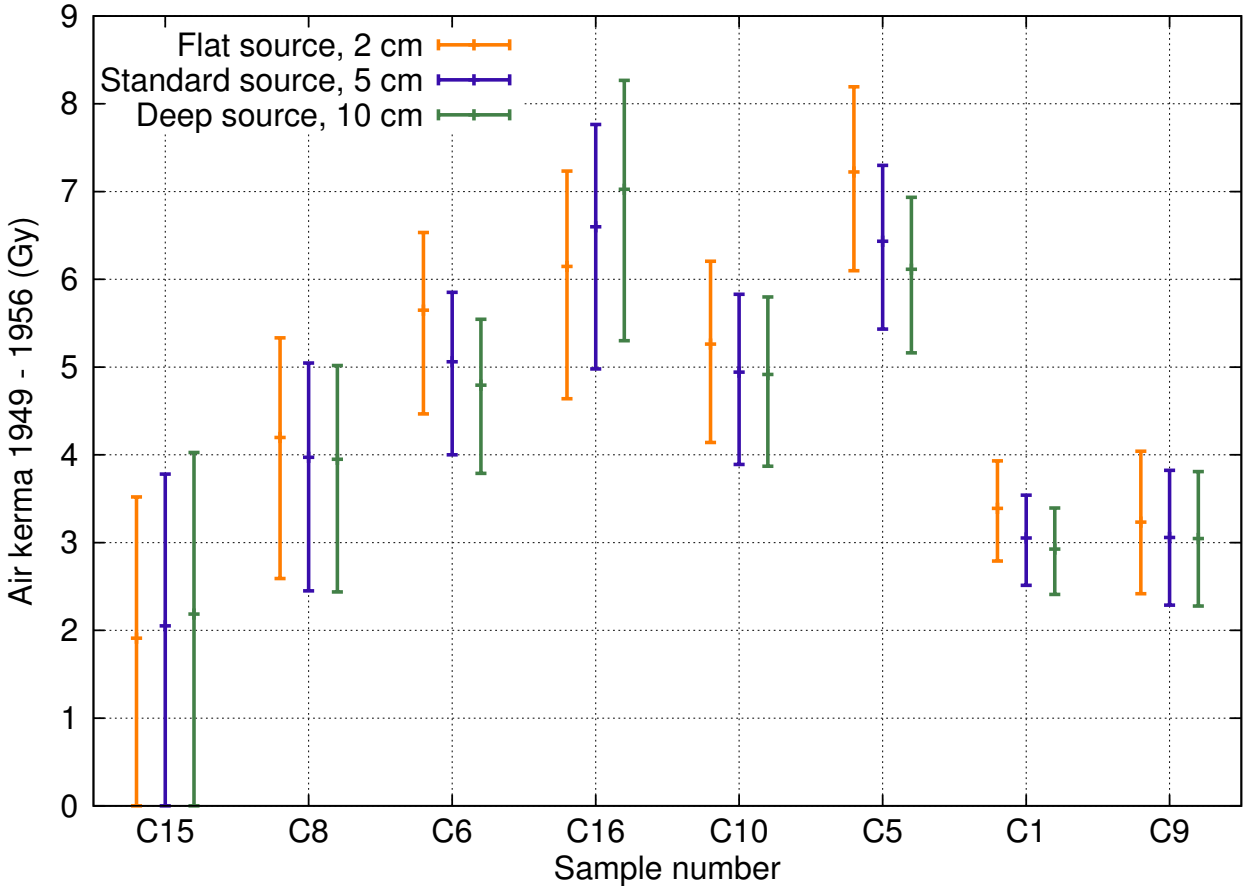

Figure 6.5: Impact of the Source Depth to the Integral Air Kerma at the Shoreline
The figure shows the same calculations as shown above but it uses the effective half-life of ^{137}Cs derived from the brick measurements with 18.7 $\pm$ 2.0 a.

6.2.2 Depth-Dose Distribution in Bricks

In the standard procedure, the brick sections from a depth of 0.5 – 1.5 cm and 2.5 – 3.5 cm were analyzed (see section 3.2.2 and Tab. 3.2). The analysis of several deeper layers in a brick allows insight in the depth-dose distribution in the brick. From this information, conclusions on the source distribution can be drawn. To get this insight, several brick samples were also analyzed in deeper sections and compared to the calculations in the Metlino model, where the brick was analyzed in 10 subsequent layers of 1 cm depth from 0.5 – 10.5 cm (see Fig. 4.13).
The calculated depth-dose distribution showed a good agreement with the measured distribution. The influence of the different source depth distributions was investigated. Only a minor change towards a stronger or lower decrease in the dose with the depth was seen for deeper or flatter sources respectively.

6.2.3 Spatial Radionuclide Distribution

As it was already mentioned in section 4.4.3, the the spatial distribution of the source in the Metlino model was determined by in-situ measurements of the sediment activity and the reconstruction with the historic map. There was sufficient data for a reconstruction on the area of the peninsula that separates two arms of the Techa river. But there was not enough data to clearly define the extension of the floodplain on the left shore of the Techa river (seen in flow direction).
The decision for one source configuration was made based on the measurements and the documents that where available.

Here, a variation in the source distribution is shown. This variation should account for the uncertainty in the determination of the floodplain to the left of the Techa river and changes the boarder of the floodplain in both directions, towards the Techa river and further apart from it. The standard floodplain (see Fig. 6.6a) of the source towards the church tower in the Metlino model was varied to cover a reduced floodplain (see Fig. 6.6b) or extended floodplain (see Fig. 6.6c).
The extension or reduction of the floodplain to the left of the Techa river is mainly motivated by the map shown in figure 4.21c. The standard source configuration stays away from the building in the North and crosses the 207 m contour line when the Techa river widens towards the South. The floodplain on the peninsula was determined to reach up to the contour line of 207 m.
In the reduced source configuration, the contour line is not crossed, and the simulated source stays in the area under 207 m.
For the extended configuration, the floodplain stretches up to the building in the North and then gets extended by about the same amount, that the reduced source was diminished. The extended source reaches up to the sources in the reservoir model.

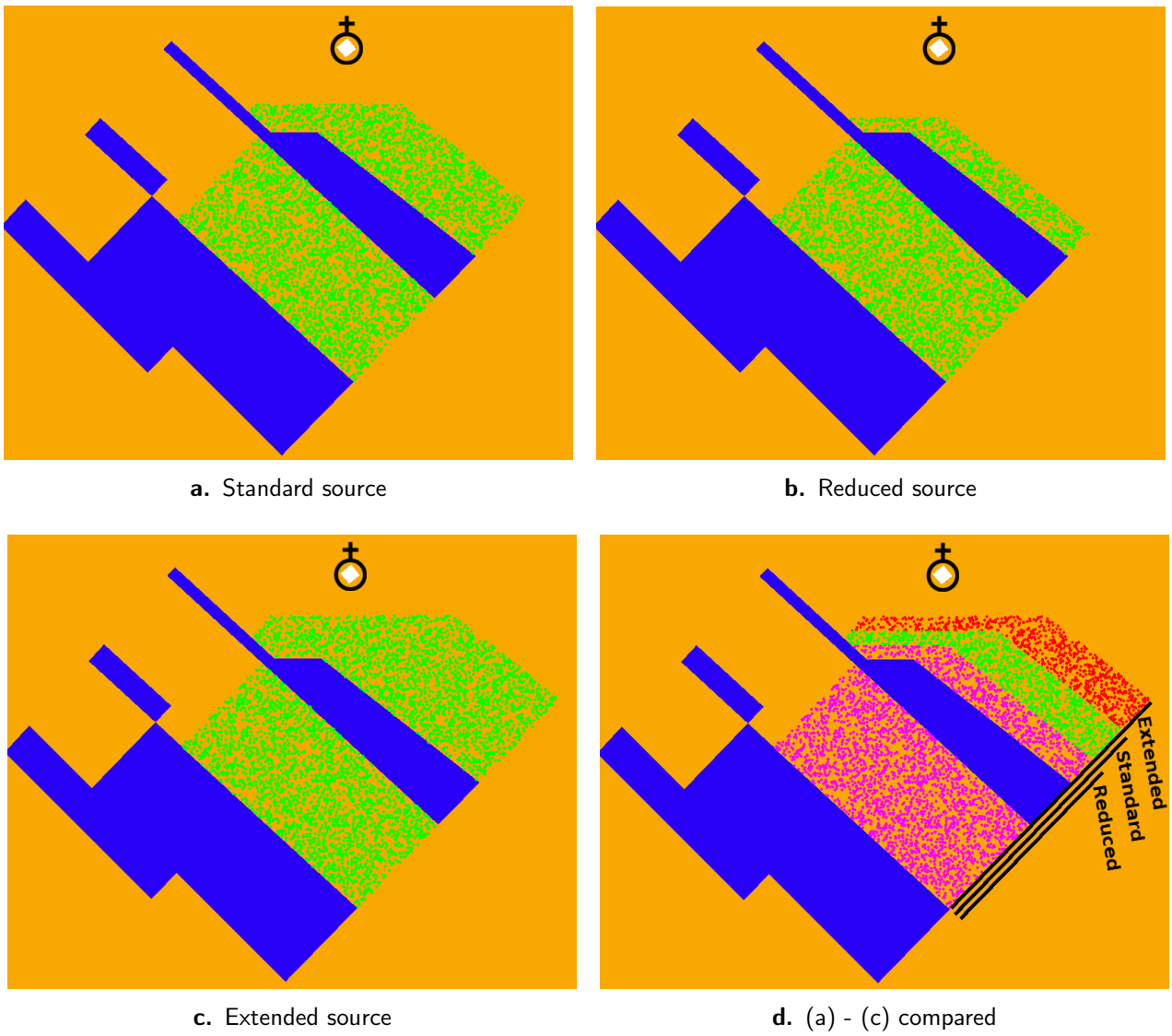

a. Standard source **b.** Reduced source

c. Extended source **d.** (a) - (c) compared

Figure 6.6: Source Distribution in the Reservoir Model
The standard floodplain of the source towards the church tower in the Metlino model **(a)** was varied to cover a reduced floodplain **(b)** or extended floodplain **(c)**. Figure **(d)** shows the difference in spacial distribution of the three configurations. The sources are indicated by dots, the Techa river is in blue, the soil in yellow.

The air kerma at the shoreline between 1949 and 1956 was calculated for the extended and reduced source configuration and compared to the standard source. The calculations show that the model is quite sensitive to the source configuration in the vicinity of the church tower (see Fig. 6.7). The impact of the spatial distribution of the source on the air kerma is more precisely seen using the estimation of the effective half-life of the radionuclide ^{137}Cs from the reservoir dose (see Fig. 6.8).

The reduced source shows an approximately 40 – 50 % increase in the air kerma at the shoreline, while the extended source shows an approximately 20 – 30 % reduction in the air kerma at the shoreline compared to the standard source.
The dose at shoreline stays constant for the detectors in air, independent of the extension of the

source, while the dose in the bricks decreases with increasing distance from the source.
Determining the correct floodplains and the appropriate distance from the source to the church tower is the crucial parameter in the estimation of the air kerma above shoreline. The source being too far away or too near to the church tower, a too high or too low activity is needed to produce the same dose at the church tower. This will influence the dose conversion factor (DCF) towards a lower value for the extended and a higher value for the reduced source. Finally this results in a higher air kerma value for the reduced source or a lower air kerma value for the extended source.

Further investigations should be performed to acquire more information on the contamination towards the church tower. The best possible knowledge of the source area is important for an accurate determination of the integral air kerma at shoreline.

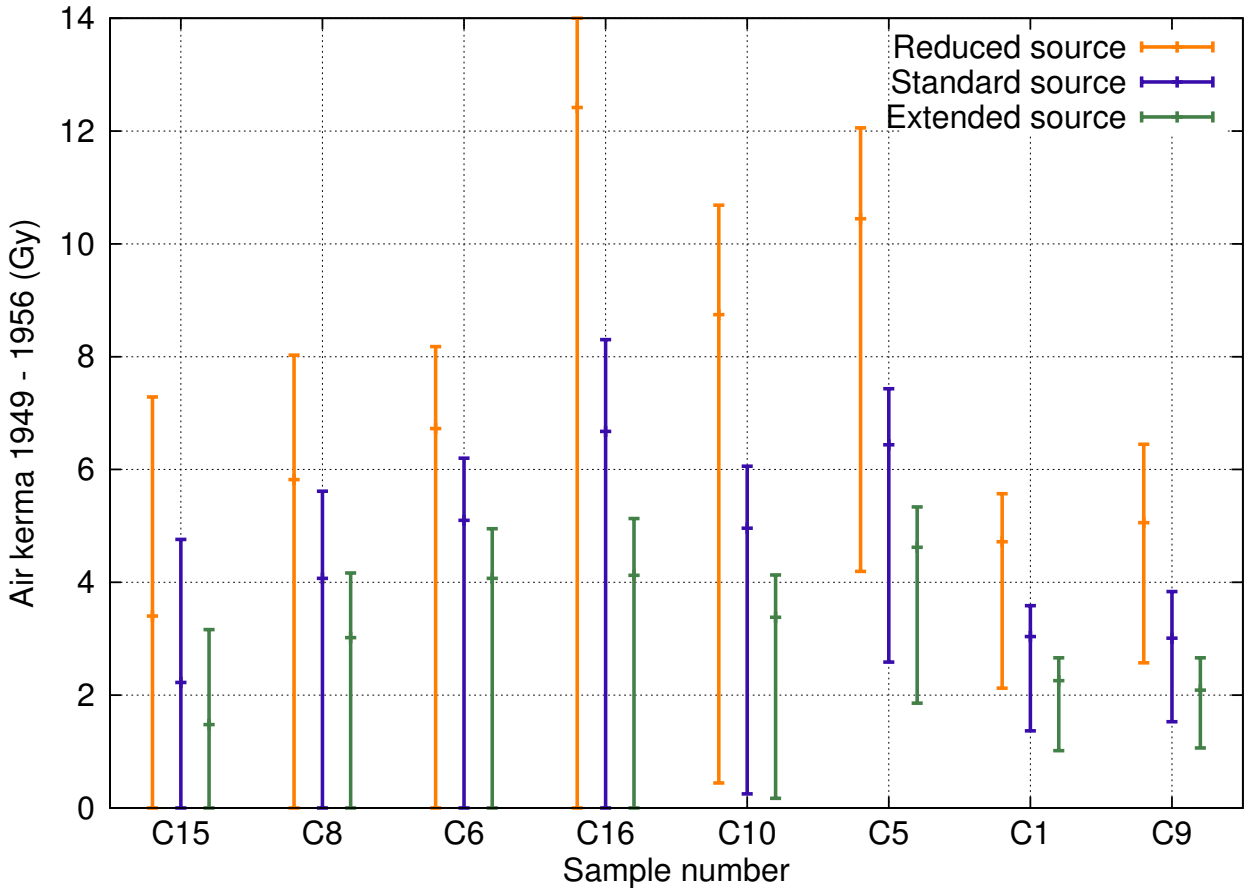

Figure 6.7: Impact of the Source Area to the Air Kerma at Shoreline
The simulations show a strong impact of the source area to the air kerma at shoreline. Extending the source towards the church tower reduces the air kerma while reducing the source towards the Techa river strongly increases the air kerma. For these calculations, an effective half-life of ^{137}Cs of 19.1 $\pm$ 5.3 a was assumed.

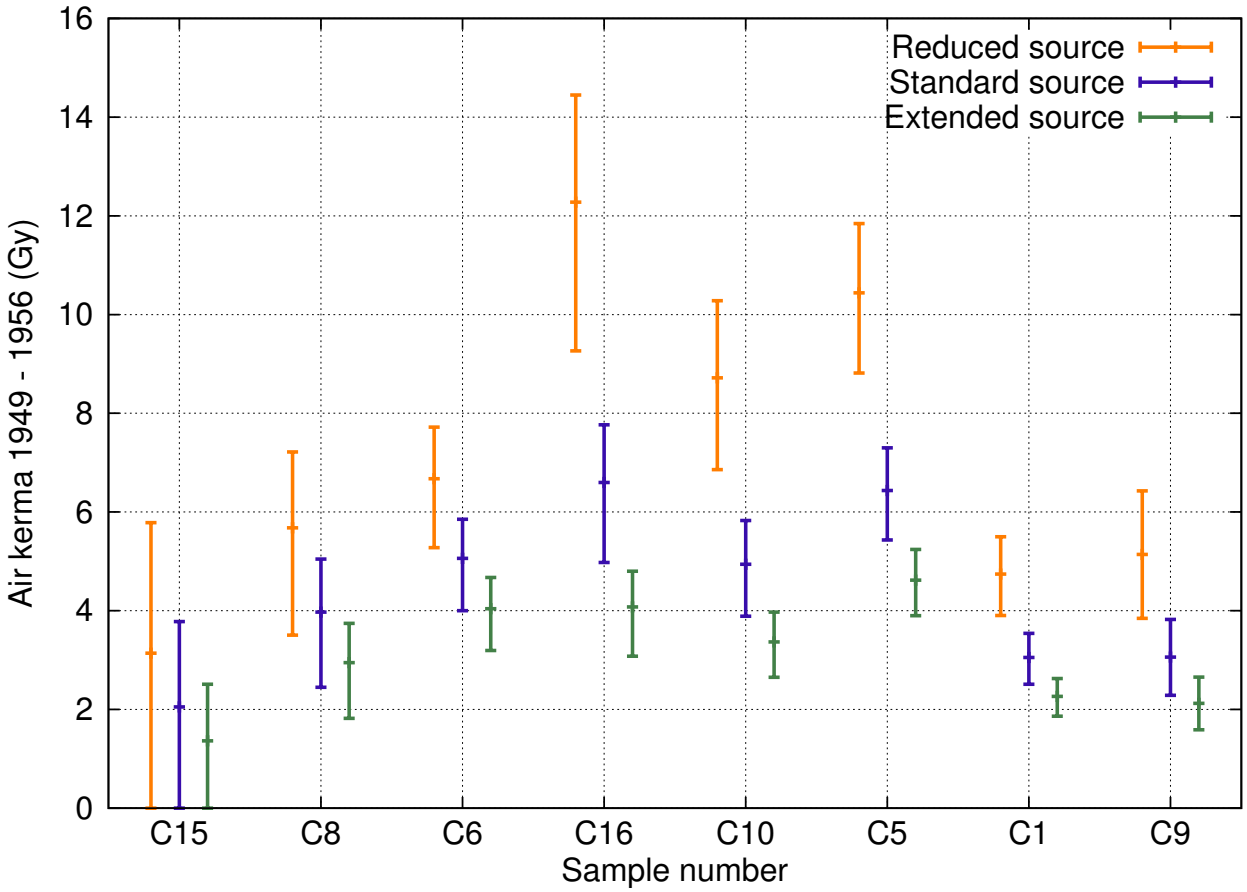

Figure 6.8: Impact of the Source Area to the Air Kerma at Shoreline
The effect of the spatial source distribution is more clearly seen using the effective half-life of ^{137}Cs of 18.7 ± 2.0 a determined by brick measurements.

6.3 Height Profiles on the South Side of the Church Tower

For the sampling positions at the church tower, three different approaches to determine the dose rate were followed in this work. First, the dose rate measurements in air with the hand held dose rate meters. Second, the dose rates measured with the TLD and third, the simulations of the dose at the sampling locations. From the Monte Carlo calculations using the reservoir model, dose conversion factors were derived that translate doses in brick to doses in air in front of the brick. Figure 6.9 shows the dose rates along the South side of the church tower determined by the different methods. All values were background corrected and converted to units of μGy h^{-1}.

The measurement and the simulation show a trend towards a higher dose rate at the bottom and a lower dose rate at the top of the church tower. The 2014 dose rate measurement shows a decrease in the dose rate between sample C21 and C16. The reservoir model estimates a slight increase between sample C21 and C16. As shown in section 4.2, an increase in the dose rate from a lower to a higher sample seems not very likely.

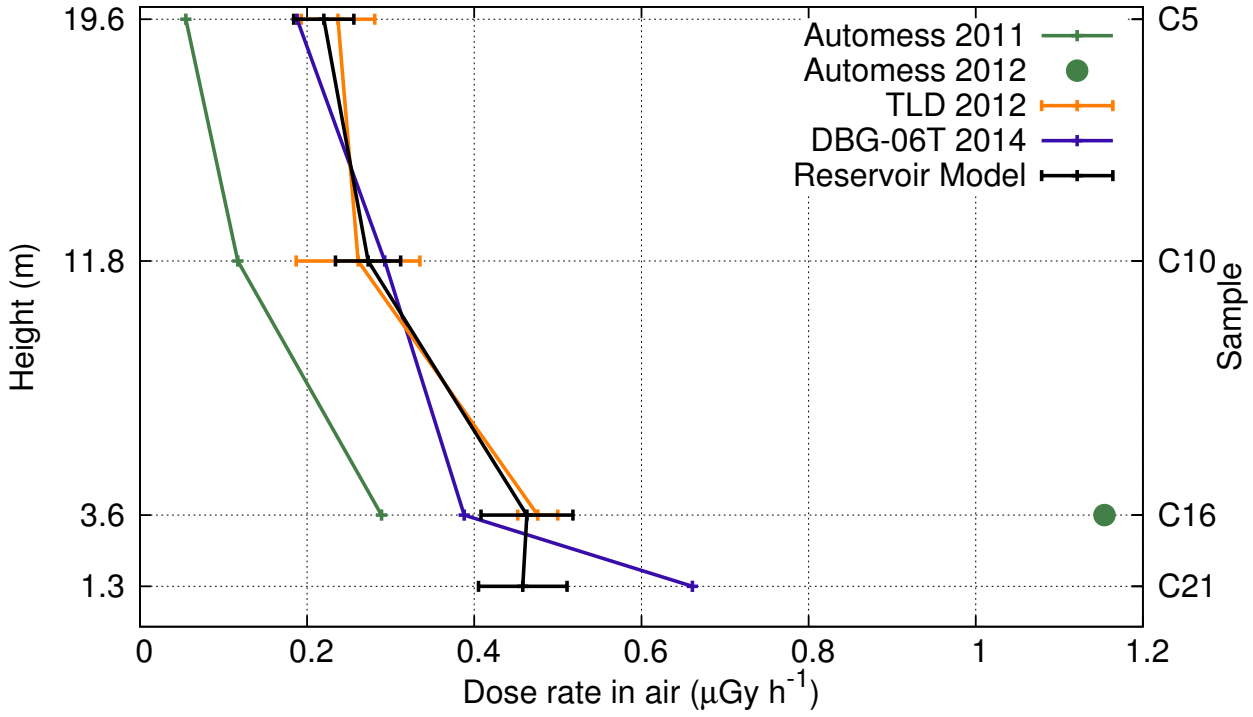

Figure 6.9: Profiles on the South Side

The height profiles of the different methods to derive the dose rate at the South side of the church tower show the variation in the estimated dose rates. All dose rates were translated into absorbed doses in air with units of µGy h^{-1}.

Measured reference for the sample C21 is only based on one dose rate in air measurement. A single dose rate measurement averaged only for a short time should not be given too much weight in these observations. These measurements are strongly affected by local effects, especially at only 1.3 m over ground as in the case of sample C21. Degteva et al. [30] also suggests taking higher samples from the church tower in Metlino in order to be independent of local changes in the contamination pattern.

No measurements over one year using TLD were performed in this corner, these could give more insight in the local effects that might explain the values of sample C21.

The reservoir model assumes an approximate dose rate of 0.4 µGy h^{-1} in the source next to C21 (see Tab. 5.1). But the measured dose rates in the vicinity of C21 show higher values (see Fig. 3.3). It shows, that this low sample is likely to be affected by local contamination patterns that are not covered by the reservoir model.

The variation in the dose rate measurements in air between the years 2011, 2012 and 2014 is quite strong. The years 2011 and 2014 show a similar pattern, but with a factor of 2 – 4.5 higher dose rates in 2014. The 2012 dose rate in air measurement is a factor 4 higher than the 2011 dose rate at sample C16. The TLD measurements of 2012 at the reservoir model show dose rates between these two measurements.

This comparison shows the strong variability and thus the large uncertainty on the dose rate measurements. A possible explanation for these strong variations in the dose rate in air between the years could be the influence of the weather conditions to the outcome of the dose rate measurements (see section 6.1).

6.4 Air Kerma Compared to the Techa River Dosimetry System (TRDS)

The TRDS-2009 shows an air kerma value for the location of Metlino of 19.8 Gy [M. Degteva, personal communication]. The work here shows air kerma values that are a factor of 2 – 4 lower than the TRDS-2009.
The calculations shown here, e.g. in section 5.2, show a strong dependence of the air kerma on the type of the detector in air. The detectors over the floodplain produce a higher dose per photon than the detectors at shoreline, and consequently a higher dose conversion factor and a higher integral air kerma. The dose in the detectors at shoreline is lower, because the adjacent river contributes no dose.

In this work, the averaged shoreline detector is used as the reference in air. Further investigations have to show, if this work here and the TRDS used a reference point with comparable contamination patterns and geometric conditions, or if the calculations presented here have to be redone with respect to a different configuration.

6.4.1 Validation of the TRDS by Taranenko et al.

The TRDS-2009 for the location of Metlino was verified by Taranenko et al. [99], but a different approach compared to this work was used.
First, they investigated the area in front of the mill, while the area of the church tower was investigated here.
Second, in this work, the floodplain was simulated as with a uniform contamination. Taranenko et al. simulated a 1 m wide strip along the shoreline with a higher contamination than the floodplain. Two different detectors in air were placed over the floodplain and over the shoreline sources. Then, they estimated, that the dose rate in 10 m distance from the shoreline, at the location of the floodplain

detector, is reduced by a factor of 6. With this, they were able to estimate that the relative source strength at the shoreline is a factor 30 higher than at the floodplain.

The environmental measurements performed in this work did not show evidence for a higher contaminated area close to the Techa river shoreline. It remains to be shown in future work, if the source configuration used in the Metlino model needs to be modified by introducing a higher contaminated narrow strip at the shoreline or, if the area in front of the church tower is contaminated differently than the area in front of the mill. These findings will show, if the TRDS is correctly estimating the dose at shoreline for the location of Metlino, or if an alternative approach for the determination has to be followed.

Chapter 7

Summary and Outlook

7.1 Summary

The study presented here deals with the reconstruction of the radiation exposure of persons living in the former village of Metlino, Southern Urals, Russia. This village was contaminated by radionuclides from the nearby Techa river, starting in 1949. The village was then evacuated and a reservoir lake was created on parts of its former area in 1956.
The key parameter in question is the time integrated air kerma at specific reference points at the shoreline. This estimate has to be used to evaluate the Techa River Dosimetry System (TRDS) for the location of Metlino. For this purpose, bricks of the walls were used as natural dosimeters and combined with radiation transport calculations to create an independent estimate of the air kerma for the time period of 1949 – 1956.

An important step in the dose reconstruction is the assessment of the contemporary gamma dose rate at the brick sampling positions. This work showed an improved method for the TL dosimetry. For this purpose, dose rate estimations using TLD, averaged over a year, have been shown to be more robust than dose rate measurements in air, where only the current dose rate is measured. This is especially important for Metlino, where the exposure conditions changed frequently.
The calculation of the conversion factors between doses in bricks and doses in TLD has shown that doses measured with Al- shielded TLD are closer to the doses measured in bricks than Cu- shielded TLD. Thus, for future experiments, it is recommended to use Al- shielded dosimeters.
It was shown, that the conversion from a dose in TLD to a dose in brick is relatively independent of the exposure geometry. In contrast to this, the dose rate in air, measured at the sampling positions at the church tower is strongly dependent on the incident angle of the geometry, thus more prone for systematic errors of the assumed geometry in comparison to the actual one.

The modeling of the Metlino site in this work showed, that the accessible sources in Metlino were

not sufficient to explain the height profile of the measurements at the brick wall. Additional sources had to be introduced under the water of the reservoir lake. These sources fit into the topological setting of Metlino and activities in a range comparable to the other sources were attributed to them. A reservoir model for the geometry of Metlino after the creation of the reservoir lake was created based on environmental measurements, TLD measurements and in situ gamma spectroscopy. It was shown, that the simulated dose rates were in good agreement with the measured annual doses in TLD. This made it possible to calculate annual doses for other sampling sites at the church tower, where no TLD dosimeters were deployed.

The combination of measurements and simulations showed that the measured doses in the North wall of the church tower were only accumulated in the time after the creation of the reservoir lake (from 1956 on). This allowed to reversely estimate the effective half-life of the radionuclide ^{137}Cs with improved precision compared to estimates of the value derived from measurements of ^{137}Cs concentrations in the water of the reservoir lake. The latter suffered from a large scatter of the ^{137}Cs concentration, introducing a large systematic error on the effective half-life. With this value, only an upper limit for the air kerma above shoreline could be derived. In contrast, with the effective half-life derived from the brick measurements, the air kerma could be assessed with greater precision.

With the model of the Metlino area for the time after the creation of the reservoir lake, called *reservoir model*, doses in the brick for the time period 1949 – 1956 could be calculated. These dose values were used in a second MCNP model, called *Metlino model*, that simulates the time before the creation of the reservoir lake. The foundation of the source definition in the Metlino model is based on historic hydrological maps and in situ gamma spectroscopic measurements. The source configuration rebuild by these measurement had to be slightly adjusted to represent the ratio of doses from the Southern to the South-Western wall of the church tower.
With the Metlino model, it was possible to evaluate the integral dose in air at the shoreline and over the floodplain.

Compared to the TRDS, the air kerma values estimated here are lower by a factor of 3 – 4. This discrepancy might be due to different reference locations and source configurations: In the TRDS, a source configuration is assumed with a strong contamination of the shoreline compared to the floodplain. This source configuration is based on historical dose rate measurements in air from the time between 1954 and 1956 around this area. The reference point for the TRDS is located over this strongly contaminated shoreline at the right side of the Techa river at the mill, 1 m above ground. In the configuration shown in this work, the in situ measurements did not give any indications that the floodplain and shoreline were significantly differently contaminated. Hence, they were simulated having the same activity, as the model presented here is based on these measurements. On the other hand, from the comparatively coarse resolution of the measurement points and the highly collimated

detector, it could be that a possible higher contaminated shoreline was simply missed. In contrast to the TRDS, the reference point in this work is on the left side of the Techa river, towards the church.
If the reference point of the TRDS is shifted from the shoreline into the floodplain, a reduced air kerma would be predicted near the church tower which would come closer to the air kerma value reconstructed in this work.
It remains to be shown in future work, if first, the source configuration has to reflect a higher contaminated shoreline on the left side of the Techa river towards the church, or if the source configuration assumed in this work remains to be correct. And second, if the reference points at the mill and at the church show a comparable contamination pattern and shall thus estimate comparable air kerma values, or if they are contaminated differently and are thus supposed to estimate different air kerma values. Only the answer to these questions can show if one of the air kerma values is true for both reference locations, or if both of the air kerma values are correctly estimated, each for its dedicated reference location.

The integral air kerma is used by the TRDS to calculate doses to the Metlino population as a village average [29, 35, 107]. This is done by assuming the relative time a person spent on three different locations:

1. At the shoreline.
2. Outside the house, but not at the shoreline.
3. Inside the house.

These three times add up to one. The TRDS then calculates the organ dose using the following equation [29, 35, 107]:

$$D_g = C_g \int_{\Delta T} dt K_r(t) \sum_L \omega_L \tau_L \tag{7.1}$$

With D_g the integral absorbed dose in organ g due to external exposure during time period ΔT, $K_r(t)$ the annual air kerma, ω_L the parameters accounting for air kerma reduction in specific locations compared to the air kerma at shoreline and τ_L the time spent at the specific location [107].
The TRDS then asses individual person doses, depending on the location of their house. The TRDS accounts for internal and external exposure. In this work, the external exposure was observed, which accounts for about one third of the total exposure at the location of Metlino (estimate after Degteva et al. [28]).

7.2 Outlook

For future investigations at the Metlino site, several extensions and improvements could be applied to the work presented here, provided additional data and measurements become available.
For the precise determination of the reservoir dose, the present day contamination should be de-

termined more precisely with TLD at more locations, especially at the South-West corner of the church tower at locations of C21 and C16. In situ gamma spectrometric measurements of sediment activity and dose rate measurements at the Southern side of the church tower would give a better possibility to reconstruct the distribution of the contamination there.
One should also monitor the weather conditions on site, e.g. with a digital thermometer and a rain gauge together with a dose rate logger to observe the change in the conditions over the year.
Any new insight into the floodplain of the Metlino model would help to improve the error range of the air kerma.

For a better description of the Metlino area in general, also the findings of the measurements at the mill and granary should be considered and integrated into one model. Dose measurements on bricks from the Southern and Eastern wall of the granary, which faced the former Techa river bed and the church, have already been performed in previous projects (see Fig. 7.1).
Next to the contaminated floodplain and shoreline of the Techa river, also the shoreline of the Metlinski pond is a source of exposure for the population of Metlino and is consequently also integrated into the TRDS. For this exposure, the North-Western wall of the granary is a suitable radiation archive, which has been sampled and analyzed in the SOUL project. A geometry model for the area of the Metlinski pond was created (see appendix D), but the validation of the TRDS for the Metlinski pond using the model and the measured doses in bricks of the granary was beyond the scope of this work.

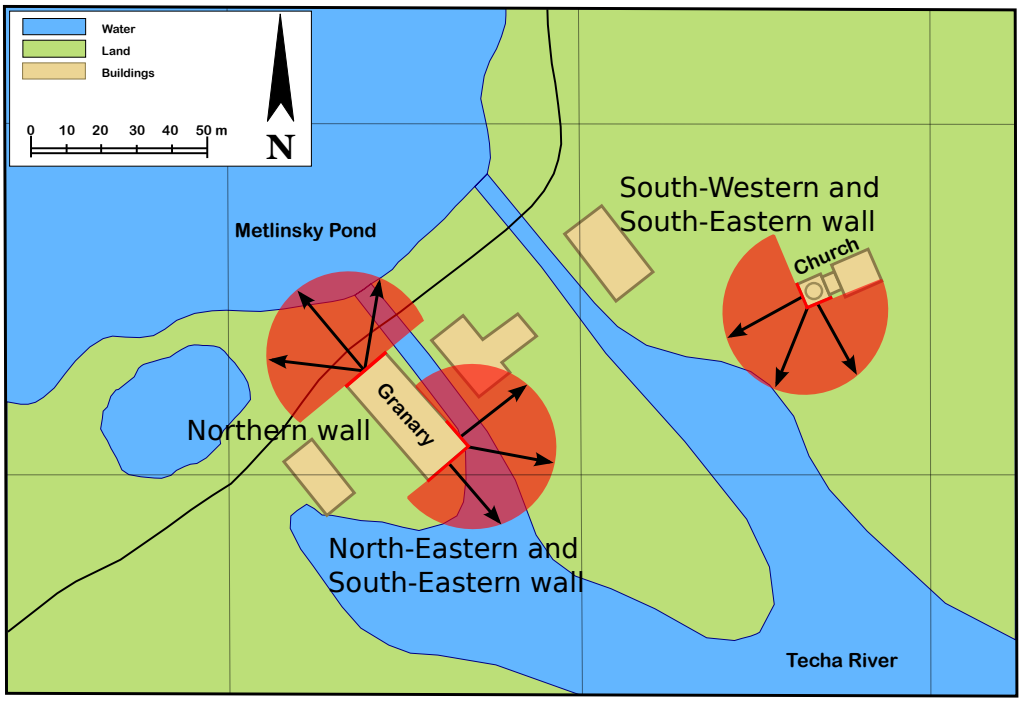

Figure 7.1: Sample Location Overview
The sketch shows the locations of the sampling sites at the buildings in Metlino.

Bibliography

[1] G. Adamiec and M.J. Aitken. Dose-rate conversion factors: Update. *Ancient TL*, 16(2):37–50, 1998.

[2] M.J. Aitken. *Thermoluminescence dating*. Studies in archaeological science. Academic Press, London, 1985.

[3] M.J. Aitken. *Introduction to Optical Dating: The Dating of Quaternary Sediments by the Use of Photon-stimulated Luminescence*. Oxford University Press, Oxford, 1998.

[4] H.L. Anderson. Metropolis, Monte Carlo, an the MANIAC. *Los Alamos Science*, LAUR-86-2600:96 – 108, 1986.

[5] L.R. Anspaugh, M.O. Degteva, and E.K. Vasilenko. Mayak Production Association: Introduction. *Radiat Environ Biophys*, 41(1):19–22, Mar 2002.

[6] T.V. Azizova, R.D. Day, N. Wald, C.R. Muirhead, J.A. O'Hagan, M.V. Sumina, Z.D. Belyaeva, M.B. Druzhinina, I.I. Teplyakov, N.G. Semenikhina, L.A. Stetsenko, E.S. Grigoryeva, L.N. Krupenina, and E.V. Vlasenko. The "clinic" medical-dosimetric database of Mayak production association workers: Structure, characteristics and prospects of utilization. *Health Phys*, 94(5):449–458, May 2008.

[7] T.V. Azizova, R.G.E. Haylock, M.B. Moseeva, M.V. Bannikova, and E.S. Grigoryeva. Cerebrovascular diseases incidence and mortality in an extended Mayak worker cohort 1948-1982. *Radiat Res*, 182(5):529–544, Nov 2014.

[8] M.C. Aznar, R. Nathan, A.S. Murray, and L. Bøtter-Jensen. Determination of differential dose rates in a mixed beta and gamma field using shielded Al2O3:C: Results of Monte Carlo modelling. *Radiation Measurements*, 37(4–5):329 – 334, 2003. Proceedings of the 10th international Conference on Luminescence and Electron-Spin Resonance Dating (LED 2002).

[9] I.K. Bailiff, L. Bøtter-Jensen, V. Correcher, A. Delgado, H.Y Göksu, H. Jungner, and S.A. Petrov. Absorbed dose evaluations in retrospective dosimetry: Methodological developments using quartz. *Radiation Measurements*, 32(5–6):609 – 613, 2000.

[10] I.K. Bailiff and S.A. Petrov. The Use of the 210°C TL Peak in Quartz for Retrospective Dosimetry. *Radiation Protection Dosimetry*, 84(1-4):551–554, 1999.

[11] I.K. Bailiff, V.F. Stepanenko, H.Y. Göksu, L. Bøtter-Jensen, L. Brodski, V. Chumak, V. Correcher, A. Delgado, V. Golikov, H. Jungner, L.G. Khamidova, T.V. Kolizshenkov, I. Likhtarev, R. Meckbach, S.A. Petrov, and S. Sholom. Comparison of retrospective luminescence dosimetry with computational modeling in two highly contaminated settlements downwind of the Chernobyl NPP. *Health Phys*, 86(1):25–41, Jan 2004.

[12] Fakultät Bauingenieurwesen Bauhaus-Universität Weimar. Bauleitung im Bestand und Lebenszyklusbetrachtung. 2010.

[13] E. Baur. *Saechtling-Kunststoff-Taschenbuch*. Hanser, München, 30th edition, 2007.

[14] Thomas & Betts. HSB750 Shrink-Kon.

[15] T.E. Booth. A Sample Problem for Variance Reduction in MCNP. *Report*, LA-10363-MS, 1985.

[16] T.E. Booth. Genesis of th Weight Window and the Weight Window Generator in MCNP. *Los Alamos Report*, LA-UR-06-5807, 2006.

[17] T.E. Booth and J.S. Hendricks. Importance estimation in forward Monte Carlo calculations. *Nuclear Technology/Fusion*, 5(1):90–100, 1984.

[18] N.G. Bougrov, A.V. Baturin, Y.H. Göksu, O.M. Degteva, and P. Jacob. Investigations of Thermoluminescence Dosimetry in the Techa River Flood Plain: Analysis of the New Results. *Radiation Protection Dosimetry*, 101(1-4):225–228, 2002.

[19] N.G. Bougrov, H.Y. Göksu, E. Haskell, M.O. Degteva, R. Meckbach, and P. Jacob. Issues in the reconstruction of environmental doses on the basis of thermoluminescence measurements in the Techa riverside. *Health Phys*, 75(6):574–583, Dec 1998.

[20] N.G. Bougrov, V.K. Vlasov, O.V. Kiryukhin, and N.L. Fatkulbayanova. Thermoluminescence measurements of ceramic samples from accidentally polluted territory of Southern Urals. *Radiation measurements*, 24(4):493–498, 1995.

[21] D.J. Brenner, R. Doll, D.T. Goodhead, E.J. Hall, C.E. Land, J.B. Little, J.H. Lubin, D.L. Preston, R.J. Preston, J.S. Puskin, E. Ron, R.K. Sachs, J.M. Samet, R.B. Setlow, and M. Zaider. Cancer risks attributable to low doses of ionizing radiation: Assessing what we really know. *Proc Natl Acad Sci U S A*, 100(24):13761–13766, Nov 2003.

[22] E.J. Calabrese and M.K. O'Connor. Estimating Risk of Low Radiation Doses - A Critical Review of the BEIR VII Report and its Use of the Linear No-Threshold (LNT) Hypothesis. *Radiat Res*, 182(5):463–474, Nov 2014.

[23] L.L. Carter and E.D. Cashwell. *Particle-Tranport Simulation with the Monte Carlo Method*. Technical Information Center, Office of Public Affairs - U.S. Energy Research and Development Administration, Los Alamos, 1st edition, 1975.

[24] A.V. Chesnokov, V.I. Fedin, A.P. Govorun, O.P. Ivanov, V.I. Liksonov an V.N. Potapov, S.V. Smirnov, S.B. Shcherbak, and L.I. Uruteskoev. Collimated Detector Technique for Measuring a ^{137}Cs Deposit in Soil under a Clean Protected Layer. *Appl. Radiat. Isot.*, 48:1265 – 1272, 1997.

[25] A.V. Chesnokov, A.P. Govorun, V.N. Fedin, O.P. Ivanov, V.I. Liksonov, V.N. Potapov, S.B. Shcherbak, S.V. Smirnov, and L.I. Urutskoev. Method and device to measure ^{137}Cs soil contamination in-situ. *Nuclear Instruments and Methods in Physics Research A*, 420:336–344, 1999.

[26] A.I. Chikshov, Y.V. Glagolenko, and Y.A. Malykh. Mayak Production Association "the fifty year old secret". *Radiat. Phs. Chem.*, 52:511 – 514, 1998.

[27] L.T. Dauer, A.L. Brooks, D.G. Hoel, W.F. Morgan, D. Stram, and P. Tran. Review and evaluation of updated research on the health effects associated with low-dose ionising radiation. *Radiat Prot Dosimetry*, 140(2):103–136, Jul 2010.

[28] M. Degteva, L. Anspaugh, and B. Napier. Techa River Population Dosimetry. *Joint Coordinating Committee for Radiation Effects Research*, 2009.

[29] M. Degteva, M. Vorobiova, V. Shved, E. Shishkina, D. Ivanov, S. Bayankin, E. Tolstykh, V. Zalyapin, A. Wieser, P Jacob, L. Anspaugh, and B. Napier. Validation of TRDS external dose estimates by EPR measurements supported by assessments of strontium-90 concentration and Monte Carlo simulations of electron transport in dental tissues. *Joint US-Russian Coordinating Committee for Radiation Effects Research*, 2004.

[30] M.O. Degteva, N.G. Bougrov, M.I. Vorobiova, P. Jacob, and H.Y. Göksu. Evaluation of anthropogenic dose distribution amongst building walls at the Metlino area of the upper Techa River region. *Radiat Environ Biophys*, 47(4):469–479, Nov 2008.

[31] M.O. Degteva, V.P. Kozheurov, E.I. Tolstykh, M.I. Vorobiova, L.R. Anspaugh, B.A. Napier, and A.N. Kovtun. The Techa River dosimetry system: Methods for the reconstruction of internal dose. *Health Phys*, 79(1):24–35, Jul 2000.

[32] M.O. Degteva, N.B. Shagina, E.I. Tolstykh, N.G. Bougrov, V.I. Zalyapin, L.R. Anspaugh, and B.A. Napier. An approach to reduction of uncertainties in internal doses reconstructed for the Techa River population. *Radiat Prot Dosimetry*, 127(1-4):480–485, 2007.

[33] M.O. Degteva, N.B. Shagina, M.I. Vorobiova, L.R. Anspaugh, and B.A. Napier. Reevaluation of waterborne releases of radioactive materials from the Mayak Production Association into the Techa River in 1949-1951. *Health Phys*, 102(1):25–38, Jan 2012.

[34] M.O. Degteva, M.I. Vorobiova, V.P. Kozheurov, E.I. Tolstykh, L.R. Anspaugh, and B.A. Napier. Dose reconstruction system for the exposed population living along the Techa River. *Health Phys*, 78(5):542–554, May 2000.

[35] M.O. Degteva, M.I. Vorobiova, E.I. Tolstykh, N.B. Shagina, E.A. Shishkina, L.R. Anspaugh, B.A. Napier, N.G. Bougrov, V.A. Shved, and E.E. Tokareva. Development of an improved dose reconstruction system for the Techa River population affected by the operation of the Mayak Production Association. *Radiat Res*, 166(1 Pt 2):255–270, Jul 2006.

[36] DTU Nutech. Denmark. Guide to "The Risø TL/OSL Reader". 2014.

[37] K.F. Eckerman and J.C. Ryman. Federal Guidance Report 12 - External Exposure to Radionuclides in Air, Water, and Soil. *Staff Report of the Federal Radiation Council*, 1993.

[38] P. Elsner, P. Eyerer, H. Domininghaus, and T. Hirth. *Domininghaus - Kunststoffe: Eigenschaften und Anwendungen*. VDI-Buch. Springer, Heidelberg, 8th edition, 2012.

[39] V. Golikov, M. Balonov, V. Erkin, and P. Jacob. Model validation for external doses due to environmental contaminations by the Chernobyl accident. *Health physics*, 77(6):654–661, 1999.

[40] H.Y. Göksu and I.K. Bailiff. Luminescence dosimetry using building materials and personal objects. *Radiat Prot Dosimetry*, 119(1-4):413–420, 2006.

[41] H.Y. Göksu, M.O. Degteva, N.G. Bougrov, R. Meckbach, E.H. Haskell, I.K. Bailiff, L. Bøtter-Jensen, H. Jungner, and P. Jacob. First international intercomparison of luminescence techniques using samples from the Techa River Valley. *Health Phys*, 82(1):94–101, Jan 2002.

[42] H.Y. Göksu, V.F. Stepanenko, I.K. Bailiff, H. Jungner, and European Study Group. Intercomparison of luminescence measurements of bricks from Dolon' village: Experimental methodology and results of European Study Group. *J Radiat Res*, 47 Suppl A:A29–A37, Feb 2006.

[43] G. Habenicht. *Kleben - Erfolgreich und Fehlerfrei: Handwerk, Praktiker, Ausbildung, Industrie*. Vieweg, Wiesbaden, 6th edition, 2008.

[44] J.S. Hendricks. Random Number Stride in Monte Carlo Calculations. *ANS 1990 Winter Meeting, Washington, D.C*, 1990.

[45] J.S. Hendricks. A Monte Carlo Code for Particle Transport an algorithm for all seasons. *Los Alamos Science*, 22:30 – 43, 1994.

[46] J.S. Hendricks and T.E. Booth. *MCNP Variance Reduction Overview*, volume 240 of *Lecture Notes in Physics*. Springer, Berlin, 1985.

[47] J.S. Hendricks and C.N. Culbertson. An assessment of MCNP weight windows. *Proc. of the PHYSOR 2000 ANS International Topical Meeting on Advances in Reactor Physics and Mathematics and Computation*, pages 7–12, 2000.

[48] J.S. Hendricks and G.W. McKinney. Pulse-Height Tallies with Variance Reduction. *Proceedings of the ANS Monte Carlo Topical Meeting*, 2005.

[49] J.H. Hubbell and S.M. Seltzer. Tables of X-Ray Mass Attenuation Coefficients and Mass Energy-Absorption Coefficients from 1 keV to 20 MeV for Elements Z = 1 to 92 and 48 Additional Substances of Dosimetric Interest. *NIST*, NISTIR 5632, 1996.

[50] N. Hunter, I.S. Kuznetsova, E.V. Labutina, and J.D. Harrison. Solid cancer incidence other than lung, liver and bone in Mayak workers: 1948-2004. *Br J Cancer*, 109(7):1989–1996, Oct 2013.

[51] O. Ivanov, A. Danilovich, V. Potapov, V. Stepanov, S. Smirnov, and A. Volkovich. Peculiarities of Environment Pollution as a Special Type of Radioactive Waste: Field Means for Comprehensive Characterization of Soil and Bottom Sediments and their Application in the Survey at the Floodplain of Techa River. In *WM2013 Conference, February 24 – 28, 2013, Phoenix, Arizona USA*, 2013.

[52] P. Jacob, S. Fesenko, I. Bogdevitch, V. Kashparov, N. Sanzharova, N. Grebenshikova, N. Isamov, N. Lazarev, A. Panov, A. Ulanovsky, Y. Zhuchenko, and M. Zhurba. Rural areas affected by the Chernobyl accident: Radiation exposure and remediation strategies. *Science of The Total Environment*, 408(1):14 – 25, 2009.

[53] P. Jacob, F. Gering, and R. Meckbach. Kerma rates in air several years after a ^{137}Cs deposition. *Kerntechnik*, 62(2-3):99–103, 1997.

[54] P. Jacob, Y. Göksu, V. Taranenko, R. Meckbach, N.G. Bougrov, M.O. Degteva, and M.I. Vorobiova. On an evaluation of external dose values in the Techa River Dosimetry System (TRDS) 2000. *Radiat Environ Biophys*, 42(3):169–174, Oct 2003.

[55] A. Jouve. SOUL - Southern Urals Radiation Risk Research - Final Report.

[56] M.H. Kalos and P.A. Whitlock. *Monte Carlo Methods - Volume I: Basics*. Wiley, New York, 1st edition, 1986.

[57] R. Karsten. *Bauchemie – Handbuch für Studium und Praxis*. C.F. Müller, Heidelberg, 10th edition, 1997.

[58] UHU GmbH & Co. KG. Technisches Merkblatt UHU Alleskleber.

[59] UHU GmbH & Co. KG. Sicherheitsdatenblatt gemäß 1907/2006/EG, Artikel 31. 2011.

[60] L. Krestinina, D.L. Preston, F.G. Davis, S. Epifanova, E. Ostroumova, E. Ron, and A. Akleyev. Leukemia incidence among people exposed to chronic radiation from the contaminated Techa River, 1953-2005. *Radiat Environ Biophys*, 49(2):195–201, May 2010.

[61] L.Y. Krestinina, F. Davis, E. Ostroumova, S. Epifanova, M. Degteva, D. Preston, and A. Akleyev. Solid cancer incidence and low-dose-rate radiation exposures in the Techa River cohort: 1956 2002. *Int J Epidemiol*, 36(5):1038–1046, Oct 2007.

[62] I. Lux and L. Koblinger. *Monte Carlo Particle Transport Methods: Neutron and Photon Calculations*. CRC Press, Boca Raton, 1991.

[63] M.R. Maynard, N.B. Shagina, E.I. Tolstykh, M.O. Degteva, T.P. Fell, and W.E. Bolch. Fetal organ dosimetry for the Techa River and Ozyorsk Offspring Cohorts, part 2: radionuclide S values for fetal self-dose and maternal cross-dose. *Radiat Environ Biophys*, Nov 2014.

[64] S.W.S. McKeever, M. Moscovitch, and P.D. Townsend. *Thermoluminescence dosimetry materials: Troperties and uses*. Nuclear Technology Pubublishing, Ashford, 1995.

[65] T.P. McLaughlin, S.P. Monahan, N.L. Pruvost, V.V. Frolov, B.G. Ryazanov, and V.I. Sviridov. *A Review of Criticality Accidents*, volume LA-13638. Los Alamos National Library, Los Alamos, 2000.

[66] R. Meckbach, I.K. Bailiff, Y. Göksu, P. Jacob, , and D. Stoneham. Calculation and Measurement of Depth Dose Distributions in Bricks. *Radiation Protection Dosimetry*, 66(1-4):183–186, 1996.

[67] N. Metropolis and S. Ulam. The Monte Carlo Method. *Journal of the American Statistical Association*, 44(247):335–341, 1949.

[68] V.F. Minenko, A.V. Ulanovsky, V.V. Drozdovitch, E.V. Shemiakina, Y.I. Gavrilin, V.T. Khrouch, S.M. Shinkarev, P.G. Voillequé, A. Bouville, L.R. Anspaugh, and N. Luckyanov. Individual thyroid dose estimates for a case-control study of chernobyl-related thyroid cancer among children of Belarus–part II. Contributions from long-lived radionuclides and external radiation. *Health Phys*, 90(4):312–327, Apr 2006.

[69] Y.G. Mokrov. Radioactive contamination of bottom sediments in the upper reaches of the Techa river: Analysis of the data obtained in 1950 and 1951. *Radiat Environ Biophys*, 42(3):155–168, Oct 2003.

[70] Y.G. Mokrov. Reconstruction of the radionuclide spectrum of liquid radioactive waste released into the Techa river in 1949-1951. *Radiat Environ Biophys*, 42(1):7–15, Apr 2003.

[71] Y.G. Mokrov. Dose assessment for the Metlino and Muslyumovo populations who lived along the Techa river from 1949 to 1954. *Radiat Environ Biophys*, 43(3):209–218, Sep 2004.

[72] Y.G. Mokrov. External radiation exposure of residents living close to the Mayak facility: Main sources, dose estimates, and comparison with earlier assessments. *Radiat Environ Biophys*, 43(2):127–139, Jul 2004.

[73] Y.G. Mokrov. Radioactive contamination in the upper part of the Techa river: Stirring-up of bottom sediments and precipitation of suspended particles. Analysis of the data obtained in 1949-1951. *Radiat Environ Biophys*, 42(4):285–293, Feb 2004.

[74] Y.G. Mokrov, P. Stukalov, and V. Martyushov. To the Problem of External Exposure Dose Estimation for the Residents of Metlino Village (the Techa River, Chelyabinsk region) in the early 1950s.

[75] W.F. Morgan and W.J. Bair. Issues in low dose radiation biology: The controversy continues. A perspective. *Radiat Res*, 179(5):501–510, May 2013.

[76] M.B. Moseeva, T.V. Azizova, E.S. Grigoryeva, and R. Haylock. Risks of circulatory diseases among Mayak PA workers with radiation doses estimated using the improved Mayak Worker Dosimetry System 2008. *Radiat Environ Biophys*, 53(2):469–477, May 2014.

[77] A.S. Murray and A.G. Wintle. The single aliquot regenerative dose protocol: Potential for improvements in reliability. *Radiation Measurements*, 37(4–5):377 – 381, 2003. Proceedings of the 10th international Conference on Luminescence and Electron-Spin Resonance Dating (LED 2002).

[78] B.A. Napier. Joint U.S./Russian studies of population exposures resulting from nuclear production activities in the southern Urals. *Health Phys*, 106(2):294–304, Feb 2014.

[79] B.A. Napier, N.B. Shagina, M.O. Degteva, E.I. Tolstykh, M.I. Vorobiova, and L.R. Anspaugh. Preliminary uncertainty analysis for the doses estimated using the Techa River dosimetry system–2000. *Health Phys*, 81(4):395–405, Oct 2001.

[80] R.H. Olsher. A practical look at Monte Carlo variance reduction methods in radiation shielding. *Nucl. Eng. Technol*, 38:225–230, 2006.

[81] The International Commission on Radiation Units and Measurements. Quantities and Units in Radiation Protection Dosimetry. *Journal of the ICRU*, 51, 1993.

[82] The International Commission on Radiation Units and Measurements. Gamma-Ray Spectrometry in the Environment. *Journal of the ICRU*, 53, 1994.

[83] The International Commission on Radiation Units and Measurements. Fundamental Quantities and Units for Ionizing Radiation (Revised). *Journal of the ICRU*, 85, 2011.

[84] International organization for standardization (ISO). X and gamma reference radiation for calibrating dosemeters and doserate meters and for determining their response as a function of photon energy – Part 3: Calibration of area and personal dosemeters and the measurement of their response as a function of energy and angle of incidence. *ISO, Geneva*, 4037-3:46, 1999.

[85] D.B. Pelowitz, J.T. Goorley, M.R. James, T.E. Booth, F.B. Brown, J.S. Bull, L.J. Cox, J.W. Durkee, J.S. Elson, M.L. Fensin, R.A. Forster, J.S. Hendricks, H.G. Hughes, R.C. Johns, B.C. Kiedrowski, R.L. Martz, S.G. Mashnik, G.W. McKinney, R.E. Prael, J.E. Sweezy, L.S. Waters, T.A. Wilcox, and A. Zukaitis. MCNP6 User's Manual Version 1.0. LA-CP-13-00634, May 2013.

[86] D.E. Peplow, T.M. Evans, and J.C. Wagner. Simultaneous optimization of tallies in difficult shielding problems. *Nuclear Technology*, 168(3):785, 2009.

[87] J.T. Randall and M.H.F. Wilkins. Phosphorescence and Electron Traps. I. The Study of Trap Distributions. *Proceedings of the Royal Society of London A: Mathematical, Physical and Engineering Sciences*, 184(999):365–389, 1945.

[88] P.F. Ricci, S.R. Straja, and A.L. Cox. Changing the Risk Paradigms Can be Good for Our Health: J-Shaped, Linear and Threshold Dose-Response Models. *Dose Response*, 10(2):177–189, 2012.

[89] A. Robertson, J. Allen, R. Laney, and A. Curnow. The cellular and molecular carcinogenic effects of radon exposure: A review. *Int J Mol Sci*, 14(7):14024–14063, 2013.

[90] K. Rybacek, P. Jacob, and R. Meckbach. In-situ determination of deposited radionuclide activities: Improved method using derived depth distributions from the measured photon spectra. *Health Phys*, 62(6):519–528, Jun 1992.

[91] V.L. Rybkina, T.V. Azizova, H. Scherthan, V. Meineke, H. Doerr, G.V. Adamova, O.V. Teplyakova, S.V. Osovets, M.V. Bannikova, and A.V. Zurochka. Expression of blood serum proteins and lymphocyte differentiation clusters after chronic occupational exposure to ionizing radiation. *Radiat Environ Biophys*, 53(4):659–670, Nov 2014.

[92] K. Saito and P. Jacob. Gamma Ray Fields in the Air Due to Sources in the Ground. *Radiation Protection Dosimetry*, 58(1):29–45, 1995.

[93] S.J. Schonfeld, L.Y. Krestinina, S. Epifanova, M.O. Degteva, A.V. Akleyev, and D.L. Preston. Solid cancer mortality in the techa river cohort (1950-2007). *Radiat Res*, 179(2):183–189, Feb 2013.

[94] R. Schwarz. The MCNP/MCNPX Visual Editor. 2013.

[95] J.K. Shultis and R.E. Faw. *Radiation shielding*. American Nuclear Society, La Garange Park, 2000.

[96] J.K. Shultis and R.E. Faw. *Fundamentals of nuclear science and engineering*. CRC Press, Boca Raton, 2008.

[97] C. Simonetto, T.V. Azizova, E.S. Grigoryeva, J.C. Kaiser, H. Schöllnberger, and M. Eidemüller. Ischemic heart disease in workers at Mayak PA: Latency of incidence risk after radiation exposure. *PLoS One*, 9(5):e96309, 2014.

[98] J. Spanier and E.M. Gelbard. *Monte Carlo Principles and Neutron Transport Problems*. Addison-Wesley series in computer science and information processing. Addison-Wesley, Reading, 1969.

[99] V. Taranenko, R. Meckbach, M.O. Degteva, N.G. Bougrov, Y. Göksu, M.I. Vorobiova, and P. Jacob. Verification of external exposure assessment for the upper Techa riverside by luminescence measurements and Monte Carlo photon transport modeling. *Radiat Environ Biophys*, 42(1):17–26, Apr 2003.

[100] X-5 Monte Carlo Team. MCNP – A General Monte Carlo N-Particle Transport Code, Version 5, including manuals vol. I & II. LA-UR-03-1987, April 24, 2003 (Revised 2/1/2008).

[101] The MathWorks Inc. Natick, Massachusetts, United States, MATLAB Release 2014b.

[102] E.I. Tolstykh, M.O. Degteva, L.M. Peremyslova, N.B. Shagina, M.I. Vorobiova, L.R. Anspaugh, and B.A. Napier. Reconstruction of long-lived radionuclide intakes for Techa riverside residents: ^{137}Cs. *Health Phys*, 104(5):481–498, May 2013.

[103] N.D. Toporkov. *Perm's eparchy Address calendar*. Publishing house of provincial government, 1882.

[104] J.E. Turner. *Atoms, Radiation, and Radiation Protection*. Wiley, Weinheim, 3rd edition, 2008.

[105] J.E. Turner, H.A. Wright, and R.N. Hamm. A Monte Carlo Primer for Health Physics. *Health Physics*, 48(6):717–733, 1985.

[106] A. Ulanovsky and C. Woda. Absorbed doses in bricks and TL-dosimeters due to environmental radiation sources. *in prep.*

[107] A. Ulanovsky, C. Woda, P. Jacob, N. Bougrov, M. Degteva, and O. Ivanov. Advanced validation of the TRDS external dose estimates in Muslyumovo with luminescence measurements. In *Soul conference*, 2010.

[108] Automation und Messtechnik GmbH. Ladenburg. Germany. Produktdatenblatt 6150ad. 2011.

[109] D. Vollenschaar. *Wendehorst Baustoffkunde*. Vencentz, Hannover, 25th edition, 1998.

[110] P. Vollhardt and N.E. Schore. *Organic Chemistry*. Freeman, New York, 7th edition, 2014.

[111] M.I. Vorobiova and M.O. Degteva. Simple model for the reconstruction of radionuclide concentrations and radiation exposures along the Techa River. *Health Phys*, 77(2):142–149, 1999.

[112] M.I. Vorobiova, M.O. Degteva, D.S. Burmistrov, N.G. Safronova, V.P. Kozheurov, L.R. Anspaugh, and B.A. Napier. Review of historical monitoring data on Techa River contamination. *Health Phys*, 76(6):605–618, Jun 1999.

[113] G.A. Wagner. *Altersbestimmung von jungen Gesteinen und Artefakten: Physikalische und chemische Uhren in Quartärgeologie und Archäologie*. Enke, Stuttgart, 1995.

[114] R.G. III Williams, C.J. Gesh, and R.T. Pagh. Compendium of Material Composition Data for Radiation Transport Modeling. *Pacific Northwest National Laboratory, Richland, Washington 99352*, 4 2006.

[115] C. Woda, P. Jacob, A. Ulanovsky, I. Fiedler, Y. Mokrov, and S. Rovny. Evaluation of external exposures of the population of Ozyorsk, Russia, with luminescence measurements of bricks. *Radiat Environ Biophys*, 48(4):405–417, Nov 2009.

[116] C. Woda, A. Ulanovsky, N. G. Bougrov, I. Fiedler, M. O. Degteva, and P. Jacob. Luminescence dosimetry in a contaminated settlement of the Techa River valley, Southern Urals, Russia. *Radiation Measurements*, 46(3):277–285, 3 2011.

[117] E.G. Yukihara and S.W.S. McKeever. *Optically Stimulated Luminescence: Fundamentals and Applications*. Wiley, 2011.

[118] P.A. Zharov, M.V. Goreleov, E.K. Vasilenko, and M.Y. Smetanin. Photon Spectra Reconstruction. *Soul Deliverable 1.1.10 WP 1.1 Sp1*, 2008.

Appendix A

Material Data used for MCNP Input

Materials can be specified in MCNP by their elemental composition. The following tables give the composition of the materials used in the simulations shown here.

The air composition was taken from Eckerman and Ryman [37] with a density of $0.00125\,\mathrm{g\,cm^{-3}}$.

H	C	N	O	Ar
0.001	< 0.001	0.751	0.236	0.013

Table A.1: Air Composition, given in weight fractions.

Two different soil compositions were studied. First the soil from Eckerman and Ryman [37] with a density of $1.6\,\mathrm{g\,cm^{-3}}$ and second the soil used in Saito and Jacob [92] with a density $1\,\mathrm{g\,cm^{-3}}$.

Soil Reference	H	C	O	Al	Si	K	Ca	Fe
Eckerman and Ryman [37]	0.021	0.016	0.577	0.050	0.271	0.013	0.041	0.011
Saito et al. [92]	0.022	–	0.575	–	0.262	–	–	0.056

Table A.2: Soil Composition, given in weight fractions.

The composition of brick samples in Metlino was evaluated by Taranenko et al. [99]. The bricks have a density of $1.8\,\mathrm{g\,cm^{-3}}$.

O	Na	Mg	Al	Si	S	K	Ca	Ti	Fe
0.475	0.005	0.017	0.085	0.296	0.002	0.026	0.040	0.006	0.048

Table A.3: Brick Composition, given in weight fractions.

Ordinary plaster consists of roughly one part slaked lime, $Ca(OH)_2$ [57] and 3.5 parts of sand, SiO_2 [109]. The density is about $2\,\mathrm{g\,cm^{-3}}$ [12]. The components add up as $7 \times Ca(OH)_2 + 2 \times SiO_2$.

H	O	Si	Ca
4	18	7	2

Table A.4: Plaster Composition, given in atomic fractions.

The wood used for floors in the church tower was taken from Williams et al. [114] with a density of $0.569\,\mathrm{g\,cm^{-3}}$.

H	C	O
0.058	0.483	0.459

Table A.5: Wood Composition, given in weight fractions.

The TL dosimeters used in this work had an Al_2O_3 chip with a density of $3.97\,\mathrm{g\,cm^{-3}}$ [64].

O	Al
3	2

Table A.6: Al_2O_3 Composition, given in atomic fractions.

The heat shrink tube consisted of a polyethylene bond with a composition of $(C_2H_4)_n$ and with a density of approximately $0.95\,\mathrm{g\,cm^{-3}}$ [14, 38].

H	C
4	2

Table A.7: Heat Shrink Tube Composition, given in atomic fractions.

Glue of the UHU® brand consists of 40 % polyvenylacetat (PVCA), $C_4H_6O_2$, [38] dissolved in 60 % acetone C_3H_6O, [110] with a density of $1.05\,\mathrm{g\,cm^{-3}}$, see technical and safety documentation of the UHU GmbH & Co. KG [58, 59]. After application of the glue, the acetate evaporates and the PVCA remains [43]. The remaining PVCA has a density of $1.17\,\mathrm{g\,cm^{-3}}$ [13].

H	C	O
6	4	2

Table A.8: Glue Composition, given in atomic fractions.

Appendix B

Results for Different MCNP Versions

The difference between MCNP5 version 1.60 [100] and the updated version MCNP 6.1 [85] for the problems used in this work was investigated. In the reservoir model, the dose per photon in the detectors in brick was scored. The reservoir model was calculated with both versions, MCNP5 and MCNP6. The dose per photon in the detectors using MCNP6 is plotted over the dose par particle using MCNP5 in figure B.1. The maximal difference between a tally in MCNP5 to MCNP6 is 0.35 %. This shows, that it is irrelevant for the calculation in these problems, which MCNP version was used. Both runs were performing $1.4 \cdot 10^{11}$ histories on the same machine. MCNP5 was running faster with $1.2 \cdot 10^{6}$ photons per minute of computer time, while MCNP6 was running at only $1.0 \cdot 10^{5}$ photons per minute.

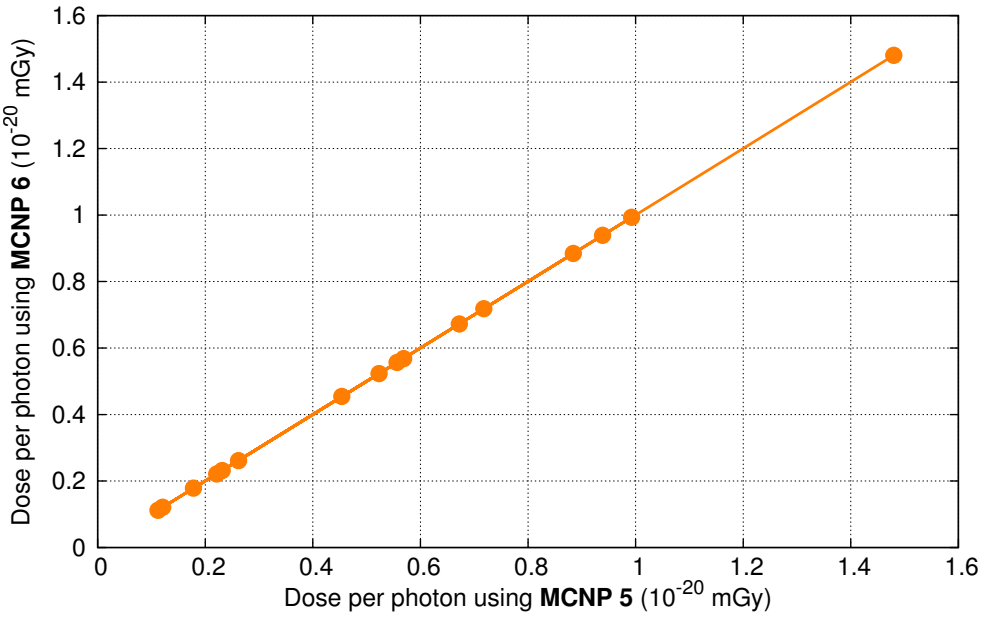

Figure B.1: Results of Calculations with two MCNP Versions
The dose per photon was calculated for the reservoir model using MCNP5 and MCNP6. No notable difference was seen in the dose per photon using either version.

Appendix C

Sampling Sites at the Church Tower

The following images show the sampling sites at the church tower.

a. Sample C5

b. Sample C5, brick extracted

c. Sample C6

d. Sample C7

Figure C.1: Sampling Sites at the Church Tower, Part 1

e. Sample C8

f. Sample C9

g. Sample C10 (right), Sample C9 (left)

h. Sample C11

i. Sample C12

j. Sample C13

Figure C.1: Sampling Sites at the Church Tower, Part 2

k. Sample C14

l. Sample C15

m. Sample C20, two bricks above C14

n. Sample C21

o. Sample C16

Figure C.1: Sampling Sites at the Church Tower, Part 3

Appendix D

Granary

In the area to the North of the granary, the dose rate was measured from the dam towards the Metlinski pond. The positions of the measurements are shown in figure D.1. The measurements were performed on a grid of approximately 5 m distance. One axis of the grid was laid out along the road on the dam, from this road it was measured perpendicularly towards the shore line.
In course of the dose rate measurements, not only the distances between points of interest, also the terrain elevation was measured.
The dose rate measurements in this area were performed in 2011 (see Tab. D.1) and repeated in 2012 (see Tab. D.2), to observe the variation between the years.

At a few positions along the shore, some TLD were placed on wooden sticks approximately 1 m over ground (see fig D.1b). The TLD stayed there for three month to get dose rates measurements averaged over a longer time period.

Brick samples were collected from the Northern wall of the granary and TLD were installed in the bricks along is central axis on a previous field trip (see Fig. D.2a).

From the measurements, a model of the granary was created (see Fig. D.2b). The geometry measurements were used to reconstruct the surrounding of the granary in the model. After the evacuation of Metlino, the dam was raised and fortified. These changes were not yet accounted for in the model. Also, there were no sources integrated into the model yet.

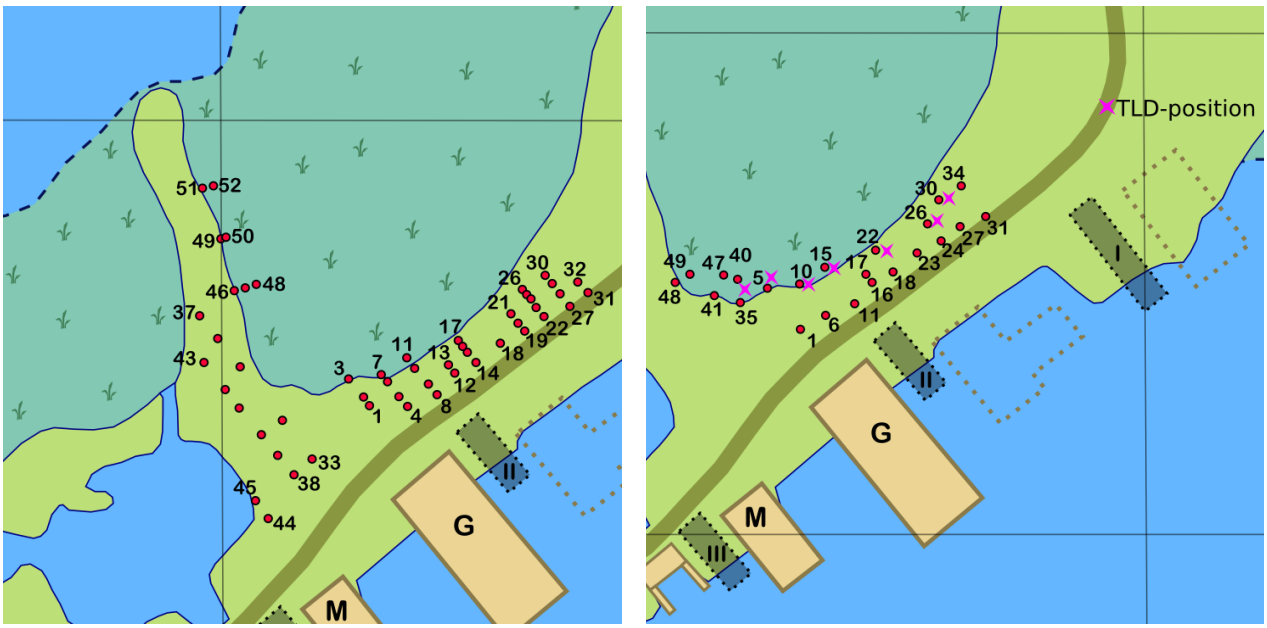

a. 2011 **b.** 2012

Figure D.1: Dose Rate Measurements at the Granary

The locations of the dose rate measurements in front of the granary that were performed in 2011 and 2012. At the locations marked with a purple star in **(b)**, TLD were installed for a few month.

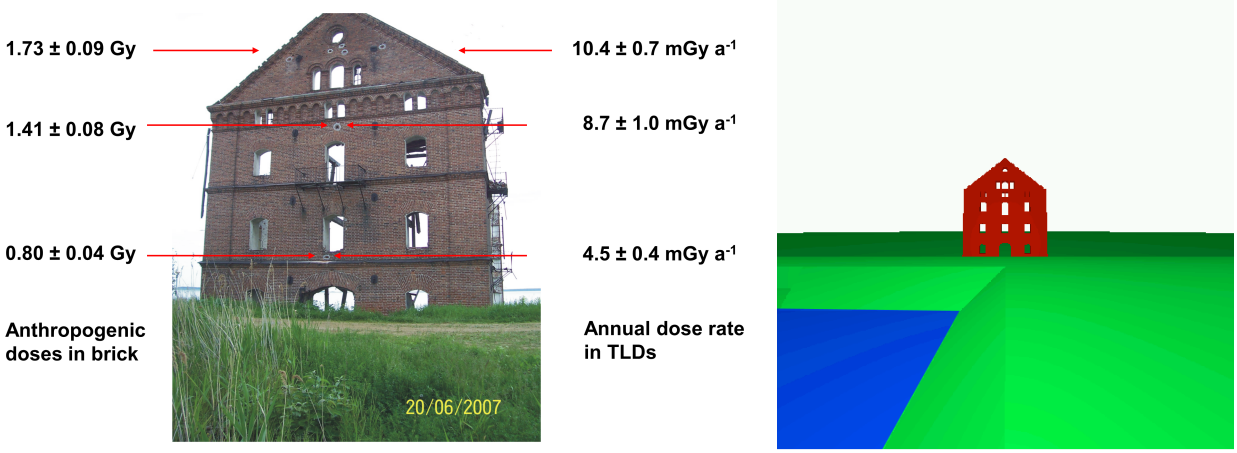

a. Northern wall **b.** Simulation

Figure D.2: Granary

a: From the Northern wall of the granary, brick samples were taken and TLD were installed along the central axes.

b: Simulation of the granary and the dam in front of it, seen from the Metlinski pond.

Nr.	Dose Rate ($\mu Sv\,h^{-1}$)	Nr.	Dose Rate ($\mu Sv\,h^{-1}$)	Nr.	Dose Rate ($\mu Sv\,h^{-1}$)
1	3.86	19	2.37	36	0.93
2	20.18	20	3.25	37	1.79
3	22.81	21	6.58	38	3.95
4	2.11	22	2.72	39	4.39
5	2.89	23	4.04	40	2.48
6	9.56	24	6.40	41	2.89
7	26.32	25	10.70	42	2.28
8	2.63	26	17.28	43	1.25
9	4.47	27	2.20	44	1.61
10	23.07	28	3.68	45	2.11
11	31.58	29	7.98	46	9.12
12	2.89	30	14.65	47	42.11
13	4.30	31	1.72	48	49.12
14	2.81	32	2.54	49	3.77
15	4.82	33	0.96	50	4.82
16	14.21	34	0.97	51	2.98
17	20.09	35	1.09	52	7.11
18	2.29				

Table D.1: Dose Rates at the Granary 2011

List of dose rate measurement at the granary region performed at the field trip in 2011. Dose rates in $\mu Sv\,h^{-1}$.

Nr.	Dose Rate ($\mu Sv\,h^{-1}$)	Nr.	Dose Rate ($\mu Sv\,h^{-1}$)	Nr.	Dose Rate ($\mu Sv\,h^{-1}$)
1	2.36	18	4	35	39
2	3.6	19	9.2	36	32
3	10.9	20	25	37	17.2
4	34	21	32	38	4.7
5	37	22	34	39	4.2
6	2.3	23	2.9	40	3.1
7	6.1	24	4.1	41	38
8	14.4	25	6.4	42	36
9	37	26	10.7	43	27
10	20	27	4.1	44	9.3
11	3.4	28	8.2	45	5.5
12	5.7	29	19.7	46	4.5
13	17.2	30	24.4	47	2.3
14	42	31	3.5	48	26.3
15	35	32	6.6	49	6.8
16	4.5	33	15.06		
17	5.5	34	24.4		

Table D.2: Dose Rates at the Granary 2012

List of dose rate measurement at the granary region performed at the field trip in 2012. Dose rates in $\mu Sv\,h^{-1}$.

Acknowledgments

First, I would like to thank Professor Dr. Herwig G. Paretzke for giving me the possibility to work on this exciting subject as well as for his personal and professional support during the time of my studies.
I am especially thankful to Dr. Clemens Woda, my supervisor at the institute of radiation protection at the Helmholtz Zentrum München for his continuous support, his confidence in me, his open ears and helping hands and for sharing hard work and huge fun on the trips to Metlino with me.

I thank everyone involved in the field trips. First of all, Dr. Nikolay Bougrov of URCRM who joined us in Metlino and helped carrying out significant parts of the sample collection and analysis.
I thank Dr. Oleg Ivanov and his colleagues from the Kurchatov Institute for performing the in-situ gamma spectroscopic measurements at the bottom of the reservoir lake.
I am thankful to Marina Degteva of URCRM and Sergey Romanov of SUBI for organizing the field trips and making it possible for us to come to Metlino. I want thank all the personnel from URCRM and SUBI that assisted our work in the field.
Also, I thank Raphael Wiegand for his help with the sample preparation in the lab at HMGU.

I thank Dr. Alexander Ulanovsky for his continuous support, his complaisant help and for showing me ways to circumvent obstacles.
I am thankful to Dr. John Hendricks and Randolph Schwarz for their support and help at and beyond several MCNP classes.
Last but not least I thank all my colleagues from the institute for their collegiality and for keeping a pleasant and productive working atmosphere.

The research leading to these results has received funding from the European Community's Seventh Framework Program (FP7/2007-2013) under grant agreement n°249675.